Advanced Techniques for High-Performance Optical Transmission and Sensing

Jian Fang

Submitted in partial fulfilment of the requirements of the degree of

Doctor of Philosophy

Department of Electrical and Electronic Engineering
THE UNIVERSITY OF MELBOURNE

August 2018

Copyright © 2018 Jian Fang

All rights reserved. No part of the publication may be reproduced in any form by print, photoprint, microfilm or any other means without written permission from the author.

Abstract

In this thesis, we explore the advanced techniques for both optical transmission and optical fibre sensing. For the optical transmission, we design a low differential modal delay (DMD) few-mode fibre with distributed long period gratings. With the help of random strong mode coupling, we verify that our scheme produces a significant DMD reduction, controllable bandwidth and environmental robustness over a long distance, leading to a great potential of high-capacity optical transmission. We next explore the application of few-mode fibre in optical fibre sensing area. A novel multi-parameter sensing technique will be demonstrated based on elliptical-core few-mode fibre. We also provide a general method for discriminative sensing with more than two modes. Experimental results show an advantageous performance for the discrimination between the temperature and strain, providing a feasible way of separating multiple parameters simultaneously.

Besides the few-mode fibres technologies, in this thesis, we will introduce two advanced techniques for high-performance distributed fibre sensing. We will first propose an ultra-fast Brillouin fibre sensing technique. By utilising the dual-polarisation orthogonal-frequency division multiplexing and coherent detection, our scheme could monitor the distributed fibre status with only single-shot measurement. The ultimate sensing speed is only limited by the fibre length, which will significantly boost the sensing speed. After that, a complex-domain Brillouin fibre sensing technique is demonstrated, by detecting the complex Brillouin spectrum directly and estimating the Brillouin frequency on the complex domain. With the complex nonlinear regression method, rigorous closed-form expressions are derived for the Brillouin frequency uncertainty. Our technique will improve the sensing accuracy by a factor of $\sqrt{2}$ and the SNR by a 3dB, which is confirmed by both simulations and experiments.

Declaration

This is to certify that

1. the thesis comprises only my original work towards the PhD,
2. due acknowledgement has been made in the text to all other material used,
3. the thesis is less than 100,000 words in length, exclusive of tables, maps, bibliographies and appendices.

Jian Fang, August 2018

Acknowledgements

First, I would like to express my sincerest gratitude to my principal supervisor, Prof. William Shieh, for his responsible supervision, patient guidance and generous support during my entire PhD candidature. Without his expertise and guidance, this thesis might not be completed.

Second, I want to thank my advisory committee members: Prof. Christina Lim and Prof. Elaine Wong, for their valuable suggestions and instructions. Moreover, I am grateful to the University of Melbourne and Australian Government Research Training Program, for providing me the scholarships and research environments.

I would like to express my deep gratitude to Dr. Ting Wang, Dr. Yaowen Li, Dr. Giovanni Milione, Dr. Philip N. Ji, Dr. Ezra Ip, Dr. Yue-Kai Huang, Dr. Ming-Fang Huang, Dr. Shuji Murakami, Dr. Yue Tian, Dr. Shaoliang Zhang, Dr. Fatih Yaman from NEC Laboratories America in Princeton, New Jersey, USA during my internship. My thanks also go to Dr. Ben Sun and Lori Pantaleo for their help during my life in the United States.

I would also like to thank my friends and colleagues at the University of Melbourne: Dr. Xi Chen, Dr. An Li, Dr. Di Che, Dr. Yifei Wang, Dr. Qian Hu, Dr. Hamid Khodakarami, Miao Sun, Chuanbowen Sun and Honglin Ji. I greatly appreciate their encouragement and assistance when I confront difficulties.

Last but not least, a very special gratitude goes to my darling, Longyue Wang, and my parents Jihong Fang and Xiaoxu Yan, for their understanding, support and sacrifice.

Preface

1. Contents arising from each contributing chapter towards the thesis:

   Chapter 3:

   Original contributions (overall percentage: 90%): proposed the low-DMD fibre design for spatial-division multiplexing, including problem formulation, fibre channel modelling, modal property analysis and simulation.

   Contribution from co-contributors (overall percentage 10%): supervised the overall development of work (name of co-contributors: William Shieh); assisted the simulation (name of co-contributors: An Li).

   Chapter 4:

   Original contributions (overall percentage: 80%): proposed the idea of a novel multi-parameter sensing technology, including the problem formulation, design the system configuration, data collection and data analysis.

   Contribution from co-contributors (overall percentage 20%): supervised the overall development of work (name of co-contributors: William Shieh and Ting Wang); assisted the experiment (name of co-contributors: Giovanni Milione, Ezra Ip, Yaowen Li, Philip N. Ji, Yue-Kai Huang, Ming-Fang Huang, Shuji Murakami); provided the fibre under test (name of co-contributors: Ming-Jun Li, Jeffery Stone, Gaozhu Peng).

   Chapter 5:

   Original contributions (overall percentage: 85%): proposed the ultra-fast Brillouin distributed fibre sensing technology, including the problem formulation, experiment demonstration, data collection and data analysis.

Contribution from co-contributors (overall percentage 15%): supervised the overall development of work (name of co-contributors: William Shieh); assisted the experiment (name of contributors: Pengbai Xu).

Chapter 6:

Original contributions (overall percentage: 85%): proposed the complex domain Brillouin distributed fibre sensing technology, including the problem formulation, experiment demonstration, data collection and data analysis.

Contribution from co-contributors (overall percentage 15%): supervised the overall development of work (name of co-contributors: William Shieh); assisted the experiment (name of contributors: Miao Sun); aided on the signal processing (name of contributors: Di Che), provided comments and suggestions (name of contributors: Matthew Myers).

2. None of the work towards the thesis has been submitted for other qualifications.

3. None of the work towards the thesis was carried out prior to enrolment in the degree.

4. No third-party editorial assistance was provided in preparation of the thesis.

5. Publications arising from each contributing chapter towards the thesis:

   Publication arising from Chapter 3:

   (a) Jian Fang, An Li and William Shieh, "Low-DMD few-mode fiber with distributed long-period fiber gratings," Optics Letters, 40, 3937-3940, 2015.

   Contribution from co-authors: Jian Fang (overall percentage 90%): composed the manuscript, designed the scheme, conducted simulations and data analysis. An Li (overall percentage 2%): aided on the fiber modelling and data analysis. William Shieh (overall percentage 8%): supervised overall development of work, guided and aided on the fiber modelling and data analysis, aided to edit and revise the paper.

(b) Jian Fang, Byoung Yoon Kim, and William Shieh, "Spinning effect in few-mode fiber with distributed long period gratings," in Proc. 21st Optoelectronics and Communications Conference (OECC)/ International Conference on Photonics in Switching 2016, ThC1-4.

Contribution from co-authors: Jian Fang (overall percentage 90%): composed the manuscript, designed the scheme, conducted simulations and data analysis. Byoung Yoon Kim (overall percentage 2%): aided to edit and revise the manuscript. William Shieh (overall percentage 8%): supervised overall development of work, guided and aided on the fibre modelling and data analysis, aided to edit and revise the manuscript.

Publication arising from Chapter 4:

(a) Jian Fang, Giovanni Milione, Jeffery Stone, Gaozhu Peng, Ming-Jun Li, Ezra Ip, Yaowen Li, Yue-Kai Huang, Philip N. Ji, Ming-Fang Huang, Shuji Murakami, William Shieh and Ting Wang, "Distributed temperature and strain sensing using Brillouin optical time-domain reflectometry over a few-mode elliptical-core optical fibre," 26th International conference on optical fibre sensors (OFS), oral presentation, 2018.

Contribution from co-authors: Jian Fang (overall percentage 80%): composed the manuscript, designed the scheme, conducted the experiment and analysed the data; Giovanni Milione (overall percentage 4%): aided on the scheme design and experimental setup; Jeffery Stone, Ming-Jun Li and Gaozhu Peng: (overall percentage 3%): provided the fibre under test. Ezra. Ip, Yaowen Li, Yue-Kai Huang, Philip N. Ji, Ming-Fang Huang and Shuji Murakami: (overall percentage 6%): aided on the system configuration; William Shieh: (overall percentage 3%): aided to edit and revised the manuscript. Ting Wang: (overall percentage 4%): supervised the overall development of the work, aided to edit and revise the manuscript.

(b) Jian Fang, Giovanni Milione, Jeffery Stone, Gaozhu Peng, Ming-Jun Li, Ezra Ip, Yaowen Li, Yue-Kai Huang, Philip N. Ji, Ming-Fang Huang, Shuji Murakami,

William Shieh and Ting Wang, "Multi-parameter sensing with higher-order optical and acoustic modes," preparing for Optics Letters.

Contribution from co-authors: Jian Fang (overall percentage 80%): composed the manuscript, designed the scheme, conducted the experiment and analysed the data; Giovanni Milione (overall percentage 4%): aided on the scheme design and experimental setup; Jeffery Stone, Ming-Jun Li and Gaozhu Peng: (overall percentage 3%): provided the fibre under test. Ezra. Ip, Yaowen Li, Yue-Kai Huang, Philip N. Ji, Ming-Fang Huang and Shuji Murakami: (overall percentage 6%): aided on the system configuration; William Shieh: (overall percentage 3%): aided to edit and revised the manuscript. Ting Wang: (overall percentage 4%): supervised the overall development of the work, aided to edit and revise the manuscript.

Publication arising from Chapter 5:

(a) Jian Fang, Pengbai Xu, Yongkang Dong and William Shieh, "Single-shot Brillouin optical time domain analyser," Optics Express 25(13), 15188-15198, 2017.

Contribution from co-authors: Jian Fang (overall percentage 85%): composed the manuscript, designed the scheme, performed the experiment and analysed the data. Pengbai Xu (overall percentage 5%): aided on the experiment, edited the manuscript. Yongkang Dong (overall percentage 2%): aided on the preparing of the manuscript. William Shieh (overall percentage 8%): supervised the overall development of the work, aided to edit and revise the manuscript.

(b) Jian Fang, William Shieh and Pengbai Xu, "Single-shot Brillouin optical time domain analysis for distributed fiber sensing," in Proc. IEEE Sensors, B4L-C, pp. 1093-1095, 2016.

Contribution from co-authors: Jian Fang (overall percentage 90%): wrote the manuscript, designed the scheme, performed the experiment and analysed the data. Pengbai Xu (overall percentage 4%): aided on the experiment, edited the manuscript. William Shieh (overall percentage 6%): supervised the overall development of the work, aided to edit and revise the manuscript.

(c) Jian Fang, Pengbai Xu and William Shieh, "Single-shot measurement of stimulated Brillouin spectrum by using OFDM probe and coherent detection," in Photonics and Fiber Technology 2016 (ACOFT, BGPP, NP), OSA Technical Digest (online), paper AT5C.3.

Contribution from co-authors: Jian Fang (overall percentage 90%): composed the manuscript, designed the scheme, performed the experiment and analysed the data. Pengbai Xu (overall percentage 4%): aided on the experiment, edited the manuscript. William Shieh (overall percentage 6%): supervised the overall development of the work, aided to edit and revise the manuscript.

Publication arising from Chapter 6:

(a) Jian Fang, Miao Sun, Di Che, Matthew Myers, Hongchun Bao, Colin Prohasky and William Shieh, "Complex Brillouin optical time domain analysis," Journal of Lightwave Technology 36(10), 1840-1850, 2018.

Contribution from authors: Jian Fang (overall percentage 85%): wrote the manuscript, designed the scheme, performed the experiment and analysed the data. Miao Sun (overall percentage 2%): aided on the experiment, edited the manuscript. Di Che (overall percentage 2%): aided on the signal processing and data analysis. Matthew Myers (overall percentage 2%): aided on preparing and revising of the manuscript. Hongchun Bao (overall percentage 2%): aided on editing of the manuscript. Colin Prohasky (overall percentage 2%): aided on editing the manuscript. William Shieh (overall percentage 5%): supervised the overall development of the work, aided on the preparation and revision of the manuscript.

(b) Jian Fang, Miao Sun, Di Che, Matthew Myers and William Shieh, "Complex domain Brillouin frequency estimation for distributed fiber sensing," in Proc. IEEE Photonics Conference, Orlando, FL, 2017, pp. 695-696.

Contribution from authors: Jian Fang (overall percentage 85%): wrote the manuscript, designed the scheme, performed the experiment and analysed the data. Miao Sun (overall percentage 2%): aided on the experiment, edited the

manuscript. Di Che (overall percentage 2%): aided on the signal processing and data analysis. Matthew Myers (overall percentage 5%): aided on preparing and revising of the manuscript. William Shieh (overall percentage 6%): supervised the overall development of the work, aided on the preparation and revision of the manuscript.

6. Research towards the thesis was supported by the Australian Government through the Australian Government Research Training Program (RTP) Scholarship, Australian Research Council (ARC) Discovery Project DP150104815 and ARC Linkage Project LP150101270.

Dedicated to the memories of my grandparents.

Contents

List of Figures

List of Tables

Chapter 1
Introduction

1.1 Introduction

Human beings have the innate desire to explore the unknown world as well express ourselves. Throughout the long span of civilisation, people have kept developing better technologies for communicating and sensing the surrounding environments.

1.1.1 Optical fibre communication

In the ancient times, communication could be verbal speech, illustrated symbols, carved pictures or written scripts. With the advancement of human society, communicating over a distance, or called telecommunication, has become desirable. In the early history, telecommunication could be the talking drums in Africa or the smoke signals in China and America. In 1809, Samuel Thomas von Sömmerring tried the first experiment electrical telegraphy. In 1838, Samual More successfully demonstrated a telegraph transmission over five kilometres. In 1879, Alexander Graham Bell showed the first telephone service across the Atlantic ocean. Since then, the demand for transmission has been growing constantly. Various electrical-based communication systems have been developed to provide better transmission service for people around the world, over the installed communication medium such as the single copper wire, twisted pair wires, and the coaxial cables. However, in the late 20 century, such kind of systems had reached a bottleneck in terms of both the channel capacity and transmission distance. For example, the operating rate of a coaxial cable can operate can be just 200 Mbps, while the signal needs to be regenerated every single kilometre. This, however, raises a costly expense for providing

high-quality communication service.

While people started seeking for better communication systems, the concept of lightwave communication was proposed after the invention of lasers. Particularly, researchers had been looking for the most appropriate lightwave transmission medium. In 1953, Bram van Heel successfully transmitted an image through an optical fibre bundle with transparent cladding. By 1960, the attenuation of glass-cladding fibres was around 1 decibel (dB) per metre. Such a high loss in the optical fibre make it impossible to be utilised in communication applications. In 1964, Dr. Charles K. Kao proposed the critical idea and specifications to fabricate the optical fibres with loss below 20 dB per kilometre.. Based on this, the silica fibre with low transmission loss was successfully fabricated in 1970. Since then, technologies have been evolved to produce low-loss fibre. In 1979, people were able to manufacture optical fibres with a loss as low as 0.2 dB per kilometre at the wavelength of 1.55 μm. To date, the widely used Corning SMF-28 fibre has a loss factor smaller than 0.18 dB/km. The lowest record of pure silica core fibres can down to 0.1419 dB/km so far [1].

Compared with the electrical-based communication systems, the optical fibre communication systems have a much broader bandwidth, resulting in a considerable boost of transmission capacity. Most of today's existing fibre communication systems are based on single-mode fibre (SMF). A single-mode fibre has many independent channels based on the different wavelength and the orthogonal polarisation. By multiplexing in both wavelength-domain (i.e. the wavelength-division multiplexing, WDM) and polarisation domain (i.e. polarisation-division multiplexing, PDM), the total net data rate can surpass 15.5 Tbps in a single fibre over 7000 kilometre transmission distance. The low attenuation of optical fibres allows signals transmitting over a very long distance. Moreover, using silica fibre can be much more cost-effective than the wires made by a copper material. So far, optical fibre communication systems using single-mode fibres have been widely used in both long-distance and short-reach applications.

One of the major advances of optical fibre communication is introduction of digital coherent technology. Early-stage optical communication systems employed the intensity-modulation and direct-detection (IM-DD) scheme. Combined with the WDM technol-

ogy and the erbium-doped fibre amplifiers (EDFAs), the IM-DD scheme has been widely used in the optical communication even today. On the other hand, with the increasing demand in transmission capacity of WDM systems, the digital coherent technology, which employs the narrow-linewidth laser source and coherent receivers, attracted a widespread of interest [2]. The digital coherent optical transmission system can implement long-range, large-capacity transmission by utilising more spectrally efficient modulation formats, such as the M-ary phase-shift keying (PSK), the quadrature-amplitude modulation (QAM), and the orthogonal frequency division multiplexing (OFDM). Compared with the IM-DD system, digital coherent technology uses the complex amplitude of light (amplitude and phase), allowing the this system to transmit more information than amplitude-only systems. Moreover, since the digital coherent reception is a linear process, all the complex information is preserved after detection, and the channel dispersion can be compensated with the post signal-processing electrically. With the aid of high-speed analogue-to-digital converter (ADC), wideband coherent receiver, and probabilistic shaping technique, the digital coherent technology has enabled the real-time coherent transmission of single-carrier 250-Gb/s uniform 16-QAM over 5523 km trans-Atlantic field trial [3], which is a milestone in the modern coherent optical communications.

1.1.2 Motivation of spatial division multiplexing

Along with the development of telecommunication, the Internet technologies have advanced rapidly in the past decades. As the result, the Internet usage has increased tremendously. Nowadays, with the growing demand of high-definition video streaming, multimedia file sharing, online gaming, cloud computation and other big data application, worldwide data traffic is growing very rapidly every year [4]. According to Cisco recent Visual Networking Index internet traffic forecast, the global IP traffic will increase three-fold in the next five years, and the annual global IP traffic will reach 4.8 ZB [1] pear year by 2022 [5]. This development leads to a higher requirement for optical transmission capacity.

In the past, the growing capacity demand has been fulfilled by using the PDM and

[1] 1 ZB = 10^{21} bytes.

WDM technologies. However, after growing over several decades, the capacity of single-mode fibres has been rapidly approaching its capacity limits, which is imposed by the combination of Shannon's information theory and nonlinear fibre effects. This bottleneck was also called capacity crunch [6]. As the transmitted data rate continues to increase, researchers have been developing new technologies to deal with this capacity crunch.

One straightforward option is installing more optical fibres. This method can linearly increase the transmission data rate, e.g. adding two more fibres for one point-to-point transmission can increase its capacity by twice. However, since all the optical components, lasers and detectors need to be increased linearly as well, the cost will be tremendous. Considering the exponentially grown capacity demand each year, the total cost will beyond measure in the future.

Another alternative is adding a new multiplexing dimension. Existing single-mode fibre-based optical transmission systems use single-mode fibres which only support the fundamental mode. However, by changing the fibre refractive index profile, such as increase the core-diameter or doping concentration, more spatial modes could be supported. According to the waveguide theory [7], the spatial modes should be orthogonal to each other, which can form several orthogonal channels for transmission. Therefore, the total channel capacity will be multiplied. This is equivalent to adding a *space* dimension to the existing multiplexing technique. Meanwhile, the digital coherent technique and the multiple-input and multiple-output (MIMO) technique have also motivated the researchers to exploit the multiple modes as independent channels in practical solutions. Based on this idea, the spatial division multiplexing (SDM) technology was proposed and has drawn much attention in the past years.

Though the multi-mode fibre (MMF), such as the GI-50 MMF, can support a number of modes at certain wavelength, it has been used for conventional communication and data networks over a fairly long time. In those applications, the MMF is used as single optical channel, and the transmitted signal is carried by multiple modes simultaneously. Due to the fibre loss and modal dispersion, MMF has been mainly used in the short-reach applications. Meanwhile, researchers have also studied the two-mode fibre (TMF) since 1970s [8,9]. Although these early works on TMFs were not designed for mode multiplex-

ing, the schematic to design the few-mode fibres (FMF) has already been demonstrated during that time. In 2000, the dispersive multiplexing scheme in MMF was proposed with MIMO technique [10], which treats different optical modes as independent channels. However, the large number of modes in MMF raises a lot of challenges such as the mode coupling, mode loss, and DSP complexity, thus restrict the application to short distances. Therefore, the few-mode fibres, which support less modes than MMFs, have been studied for mode multiplexing, for their potential to provide high mode selectivity and long transmission distance.

The general concept of SDM includes several different types of a transmission system. Depending on the type of fibres, they can be classified into two main categories: the mode-division-multiplexing (MDM) systems and the multi-core fibre (MCF)-based systems. Mode-division-multiplexing systems use few-mode fibres , which is a kind of multimode fibres but only supports a few numbers of modes. The MCF-based system uses multi-core fibre, which packages several single-mode (or few-mode) fibre cores within one cladding structure. Both of them have the promising potential for overcoming the capacity crunch. Compared with MCF, the FMF has the similar shape to the SMF, therefore the fabrication process could be easier. Therefore, FMFs have been widely studied in SDM transmission systems. It is noted that by combining the multi-core and the few-mode techniques, the transmission capacity can achieve 10.16-Peta-B/s over 11.3-km 6-mode 19-core fibre [11].

Although the SDM transmission with FMF has become a very active research field, challenging issues are still ahead before this technology can be used in the practical long-haul transmission. One important issue is the mode coupling between the guided modes. Due to the unavoidable perturbation in the fibre link, the spatial modes in few-mode fibres suffer from the mode coupling effect, which will hinder the recovery of transmitted signals. Therefore, designing and manufacturing the high-performance few-mode fibre is a very attractive topic in SDM transmission area.

1.1.3 Optical fibre sensors

Besides communication, sensing is the other important issue. There are many environmental parameters around that are critical to the quality of the life to human beings, such as the temperature, the air pressure, the humidity, the concentration of oxygen and the sunlight. The surrounding environment can be roughly perceived by our body. However, in order to sense the actual condition over a distance, or to measure some parameter with a high accuracy, a remote sensor is necessary.

Sensors, which is related to measurement technology, have been around for quite some time in various forms. The first thermostat, which was considered as the first modern sensor by some people, came to market in 1883. The idea of sensing through optical fibre first emerged half a century ago. In the mid-1960s, the Fotonic Sensor filed a patent, based on the bifurcated fibre bundle for position/vibration measurement [12].

Optical fibre sensors are devices that utilise the lightwave to convey the information which they sense. They can be either discrete (i.e. has one or several monitor points) or distributed (i.e. the sensor is an optical fibre itself). Compared with conventional sensors, optical fibre sensors have relatively small size, low cost and high reliability. Since the sensor medium is silica, it can be durable under some extreme condition, such as high temperature up to 1200°C [13].

A distributed optical fibre sensor (DOFS) is a kind of *intrinsic* sensor that can monitor the physical parameters at every point along the optical fibres. The word *intrinsic* means the sensor keeps the light within the fibre inside, and the external physical condition modulates the light from outside. Detectable physical parameters include temperature, strain, pressure, bending, vibration, breakpoints, etc. In principle, the environmental variation changes the refractive index at each position of the fibre. This kind of refractive index change can be conveyed by sending an optical light probe, reading the backscattering signals and then interpreting them into the desired physical values.

The DOFS technology can be retrospected to the study on optical time-domain reflectometry (OTDR) in 1976. This technology was initiated for locating the faulty positions in an optical transmission line. After three-decades development, many different types of DOFS have been proposed and demonstrated. According to the different scattering

principle, the distributed optical fibre sensors can be classified into three types:

1. **Rayleigh OTDR**

   The Rayleigh OTDR is based on Rayleigh backscattering, which is a predominantly elastic scattering in optical fibres. Early stage development of Rayleigh OTDR uses incoherent broadband laser source to generate probe pulses. This kind of incoherent Rayleigh OTDR is also called conventional OTDR, which has been used in faulty/splice point detection. With the development of coherent optical communication technologies, Rayleigh-based coherent OTDR (COTDR) has also been proposed. COTDR system adopts a narrow linewidth laser source and direct detection has been used in the distributed vibration sensing (DVS). COTDR with coherent detection gives a much better performance in distributed acoustic sensing (DAS), at the cost of high expense and complicated signal processing.

2. **Raman OTDR**

   The Raman OTDR, or ROTDR, refers to the sensor system based on spontaneous Raman scattering (SpRS). SpRS is a kind of inelastic scattering caused by thermal vibration of the lattice. This thermal vibration generates a high-frequency shift (around 10THz) with a broad bandwidth (tens of nm). Raman scattering is insensitive to strain but sensitive to temperature. Due to this property and simple structure, Raman OTDR has been widely used in the distributed temperature sensing (DTS).

3. **Brillouin-based fibre sensors**

   The Brillouin-based fibre sensors include the Brillouin OTDR (BOTDR) and the Brillouin optical time-domain analysis (BOTDA). BOTDR is based on the spontaneous Brillouin scattering (SpBS), which is inelastic. In optical fibres, SpBS is the interaction between the light field and hyper-sonic acoustic waves. This process generates a Brillouin frequency shift around 11GHz, and is sensitive to both temperature and longitudinal strain. Therefore, BOTDR can be used for temperature or strain sensor. BOTDA is based on the stimulated Brillouin scattering (SBS), which is the interaction of three waves: the pump wave, the probe wave, and the acoustic waves. As a

result, BOTDA requires a double-ended access to the tested fibre. BOTDA can also be used as temperature or strain sensing, with a stronger received signal and better resolution than BOTDR.

According to the reported results, Brillouin-based optical fibre sensors have the superior performance to ROTDR, in both the sensing accuracy and distance. Note that the Brillouin frequency is sensitive to both temperature and strain, so separating temperature and strain has been a great challenge in Brillouin fibre sensing.

The DOFSs described above are working with SMF or MMF. With the growing research on SDM technology, few-mode fibres are also used in optical fibre sensing field. Compared with SMF-based DOFS, FMF has a larger core-diameter, which can increase the Rayleigh scattering power, as well as the nonlinear power threshold. Meanwhile, FMF-based DOFS can control and manage the launched spatial modes, meaning that it could obtain more information than only one mode. This feature can be used for multi-parameter sensing, such as the discrimination between the temperature and strain.

1.2 Thesis outline

The contents of this thesis are organised as follows:

Chapter 1 Introduction: This chapter gives the background of this thesis, as well as a historical development of several key technologies in optical transmission and sensing. We also introduce the motivation of spatial division multiplexing technique. Several different types of distributed optical fibre sensors are briefly presented.

Chapter 2 Literature review: In this chapter, the mode-division multiplexing (SDM) technology is reviewed first, including the MDM fibres and modes, mode multiplexers and demultiplexers, few-mode amplifiers and few-mode transmission system. Then we reviewed the current methods for dispersion control in FMF and explained the relationship between modal dispersion and digital signal processing (DSP) complexity. We also give a brief review for the recent progress of few-mode fibre sensors in different applications. Finally, we introduce several other attractive fields in the distributed fibre sensing area, which have a promising research perspective.

Chapter 3 Low-DMD FMF for optical transmission: This chapter first discuss the motivation for designing the Low-DMD fibre. Then the design principle of the FMF with distributed grating is illustrated. We introduce the coupled mode equations method for the evaluation of the mode coupling and build a model for random fibre channel. Possible fabrication is also discussed after that. To evaluate the performance of our design, We perform intensive simulations. Finally, the results show a considerable improvement in the DMD reduction. Discussions are also given for practical consideration.

Chapter 4 Multi-parameter sensing with few-mode fibres: In this chapter, we demonstrate a novel multi-parameter sensing technology with the help of few-mode fibres. We first introduce the principle of few-mode Brillouin fibre sensors. Then the methods for multi-parameter discrimination is discussed, including the conventional two-mode method and our generalised more-mode method. A few-mode BOTDR system is configured, using the elliptical-core FMF. Then we characterise the spontaneous Brillouin scattering spectrum. As a sensor, its temperature and strain dependence is experimentally calibrated. Finally, we show the improved performance of our technology in the discriminative sensing.

Chapter 5 Ultra-fast Brillouin fibre sensing technology: In this chapter, we propose an ultra-fast Brillouin fibre sensing technique, which can monitor the fibre with only one-shot measurement. The motivation for developing such technique is firstly discussed. Then we show the principle of this method. To validate the feasibility, the experimental setup and system configuration are given. We also give the details of the data processing procedure. Experimental results confirm that our method can significantly boost the sensing speed. At last, we discuss some issue in this problem, as well as the future perspectives.

Chapter 6 Complex-domain Brillouin fibre sensing technology: This chapter shows an advanced technology named complex-domain Brillouin fibre sensors. We first explain the motivation of this research. Then the detection method for complex Brillouin spectrum is illustrated. Rigorous theoretical formula are derived, along with the closed-form expressions for the BFS uncertainty. We conduct both Monte-Carlo simulation and experiment to verify our improvement. The results show a $\sqrt{2}$ improvement of sensing

accuracy and a 3-dB improvement of signal-to-noise issue. Discussions are finally given for some issues in practical applications.

Chapter 7 Conclusions: In this chapter, we summarise the main results in this thesis and give some perspective of future research directions.

1.3 Publications

Papers

1. Jian Fang, Giovanni Milione, Jeffery Stone, Gaozhu Peng, Ming-Jun Li, Ezra Ip, Yaowen Li, Yue-Kai Huang, Philip N. Ji, Ming-Fang Huang, Shuji Murakami, William Shieh, Ting Wang, "Multi-parameter sensing with higher order optical and acoustic modes," submitted to Optics Letters, accepted.

2. Jian Fang, Giovanni Milione, Jeffery Stone, Gaozhu Peng, Ming-Jun Li, Ezra Ip, Yaowen Li, Yue-Kai Huang, Philip N. Ji, Ming-Fang Huang, Shuji Murakami, William Shieh and Ting Wang, "Distributed temperature and strain sensing using Brillouin optical time-domain reflectometry over a few-mode elliptical-core optical fibre," 26th International conference on optical fibre sensors (OFS), TuD1, 2018.

3. Jian Fang, Miao Sun, Di Che, Matthew Myers, Hongchun Bao, Colin Prohasky and William Shieh, "Complex Brillouin optical time domain analysis," Journal of Lightwave Technology 36(10), 1840-1850, 2018.

4. Jian Fang, Miao Sun, Di Che, Matthew Myers and William Shieh, "Complex domain Brillouin frequency estimation for distributed fibre sensing," in Proc. IEEE Photonics Conference, Orlando, FL, 2017, pp. 695-696.

5. Jian Fang, Pengbai Xu, Yongkang Dong and William Shieh, "Single-shot Brillouin optical time domain analyser," Optics Express 25(13), 15188-15198, 2017.

6. Jian Fang, William Shieh and Pengbai Xu, "Single-shot Brillouin optical time domain analysis for distributed fibre sensing," in Proc. IEEE Sensors, B4L-C, 1093-1095, 2016.

7. Jian Fang, Pengbai Xu and William Shieh, "Single-shot measurement of stimulated Brillouin spectrum by using OFDM probe and coherent detection," in Photonics and fibre Technology 2016 (ACOFT, BGPP, NP), OSA Technical Digest (online), paper AT5C.3.

8. Jian Fang, Byoung Yoon Kim, and William Shieh, "Spinning effect in few-mode fibre with distributed long period gratings," in Proc. 21st Optoelectronics and Communications Conference (OECC)/ International Conference on Photonics in Switching 2016, ThC1-4.

9. Jian Fang, An Li and William Shieh, "Low-DMD few-mode fibre with distributed long-period fibre gratings," Optics Letters, 40, 3937-3940, 2015.

10. Yifei Wang, Jian Fang, An Li, Qi Yang and William Shieh, "Complex imaging via coherent detection," Optics Express 25(15), 17295-17305, 2017.

11. Yifei Wang, Jian Fang, An Li, Qi Yang and William Shieh, "Nearfield Complex Imaging," in Proc. Optical fibre Communication Conference, Th4H. 4, 2017.

12. Yifei Wang, Xi Chen, An Li, Jian Fang, Qi Yang and William Shieh, "Complex imaging for detecting few-mode fibre modes," in Proc. Signal Processing in Photonics Communications, SpTh3D.3, 2017.

13. Di Che, Jian Fang, Hamid Khodakarami and William Shieh, "Polarization multiplexing without wavelength control," presented at European Conference on Optical Communication (ECOC) 2017.

14. Di Che, Feng Yuan, Qi Yang, Hamid Khodakarami, Yifei Wang, Jian Fang and William Shieh, "Reinventing Optical Direct Modulation by Frequency Chirp," in Asia Communications and Photonics Conference (ACP) 2016, OSA Technical Digest, AF1C.3.

15. An Li, Yifei Wang, Jian Fang, Ming-Jun Li, Byoung Yoon Kim and William Shieh, "Few-mode fibre multi-parameter sensor with distributed temperature and strain discrimination," Optics Letters, 40(7), 1488-1491, 2015.

16. An Li, Yifei Wang, Jian Fang and William Shieh, "Distributed Temperature and Strain Discrimination Using a Few-Mode fibre," CLEO: Science and Innovations, SM1L.3, 2015.

17. Qian Hu, Di Che, Yifei Wang, An Li, Jian Fang and William Shieh, "Beyond amplitude only detection for digital coherent system using directly modulated laser," Optics Letters, 40(12), 2762-2765, 2015

Patent

1. Yaowen Li, Jian Fang, Ting Wang, Philip N. Ji, Yue-Kai Huang, Shuji Murakami, Giovanni Milione, "A multi-layer coding method for distributed physical value measurement," filed for US Patent.

Chapter 2
Literature Review

2.1 Mode division multiplexing technology

Mode division multiplexing (MDM) [14] is an important branch of spatial division multiplexing (SDM). As we introduced in chapter 1, MDM technology was first proposed to overcome the so-called capacity crunch [6, 15–17]. Besides the existing multiplexing methods of wavelength and polarisation, MDM adds a new dimension: the *spatial mode*, to drastically increase the fibre channel capacity.

2.1.1 MDM fibres and modes

In mode division multipled transmission, each mode is designed for carrying independent information. Conventional single-mode fibres (SMFs) with 8$\sim$9μm core diameter and 125 μm cladding diameter can support only one mode per polarisation. Conventional multimode fibres (MMFs) with core/cladding diameters of 50/125 μm and 62.5/125 μm can support more than 50 spatial modes. It is also possible to fabricate multimode fibres support as many as several hundred modes. Early stage research on MDM technology focused on MMF [10, 18]. However, MMF supports too many modes which will couple with each other even over a middle-range distance. Therefore, MMF-based MDM demonstrations are limited to a small number of modes, with the assistance of the spatial filters [19]. Therefore, few-mode fibres (FMFs), which only supports a small number of modes, have been proposed for MDM technology. Compared with MMF, few-mode fibres have the manageable number of modes. Therefore, they are relatively easy to handle and can be used to prove certain concepts in MDM technology.

The optical modes guided in FMF are the modes that can be well constrained in the core region and can propagate with acceptable attenuation. The mode condition can be described using the normalised frequency V (also known as V number of the Abbe number). For a step-index fibre structure, V-number is defined as [20]:

$$V = \frac{2\pi a}{\lambda}\sqrt{n_1^2 - n_2^2} \approx \frac{2\pi n_1 a}{\lambda}\sqrt{2\Delta} \tag{2.1}$$

where a is the core diameter, λ is the wavelength in vacuum. n_1 and n_2 are the refractive indices of the core and cladding, respectively. $\Delta := (n_1 - n_2)/n_1$ is the refractive index difference. If the V number is larger than 2.405, it could guide more than one spatial mode.

In FMF, the discrepancy between n_1 and n_2 is usually small enough (i.e. Δ less than 1%). In this case, weakly guidance approximation is applied in the simplified modal analysis [21]. Mode groups under this approximation were designated as LP (linearly polarised) modes. The number of supported LP modes is related to the V parameter of FMF profile, i.e. $N \approx V^2/2$.

The simplest example of FMF is the two-mode fibre (TMF), with $2.4 < V < 3.8$. A circular-core two-mode supports two LP modes: LP_{01} mode and LP_{11} mode.

2.1.2 Mode multiplexers and demultiplexers

Besides fibres, another important component in MDM is the mode multiplexers (MMUX), which can be inversely used as the mode de-multiplexers (MDMUX). So far, a lot of mode multiplexers have been experimentally demonstrated which can be classified into two types. The first type is matching the LP mode field pattern of the input side to the mode pattern of the output fibre. In early-stage SDM experiments [22–25], mode multiplexer is realized by combining mode converters with passive mode combiners. Mode conversion could be achieved by using fixed phase plates [22], spatial light modulator, long-period fibre gratings [23, 26] or liquid crystal in silicon panels [27]. Passive mode combiners can be realised by using free-space beam splitters and collimators.

Free-space mode multiplexers are widely used in early-stage SDM experiments, as

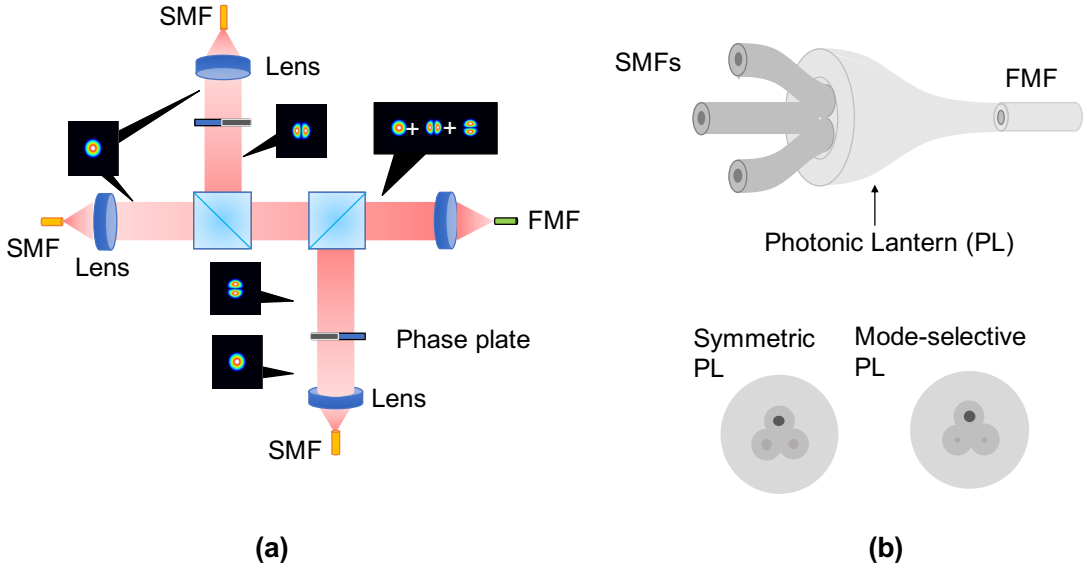

Figure 2.1: Mode multiplexers by matching mode field pattern (a) Free-space mode multiplexer with fixed phase plate. (b) Photonic lantern supports 3 spatial modes.

shown in Fig. 2.1(a). However, they are usually cumbersome, space-consuming and lossy. To minimise the insertion loss and the volume of the mode multiplexer, low-loss optical waveguide device, which is called photonic lantern (PL), has been proposed, as in Fig. 2.1(b). The photonic lanterns are couplers which made by adiabatically tapered several closely placed SMFs into a FMF [28]. Photonic lanterns can be either symmetric or mode-selective. Symmetric photonic lanterns, sometimes also called standard photonic lanterns, have identical single-mode input fibres. When the input signals are injected through these identical fibres and pass through the adiabatic taper, they couple to each other and finally form a combination of supported modes of output few-mode fibre. Since the symmetric photonic lantern will scramble single-mode input into few-mode output, e.g. each input signal excites all the output modes, MIMO signal processing is necessary, which may increase the system computation complexity. Mode-selective photonic lanterns, which allow each input excited one selected output mode, can be made with dissimilar input fibres [29,30]. Comparing with symmetric photonic lanterns, mode-selective photonic lanterns are more difficult in the manufacture, while they could reduce the complexity of MIMO signal processing in MDM systems. The state-of-the-art mode-(group)-selective photonic lanterns can support three group-mode selectively (LP_{01} with

20 dB selectivity, LP_{11} with 10 dB selectivity, and LP_{21}+LP_{02} with 7 dB selectivity) with low insertion loss (-0.06 dB) over the entire C-band [30].

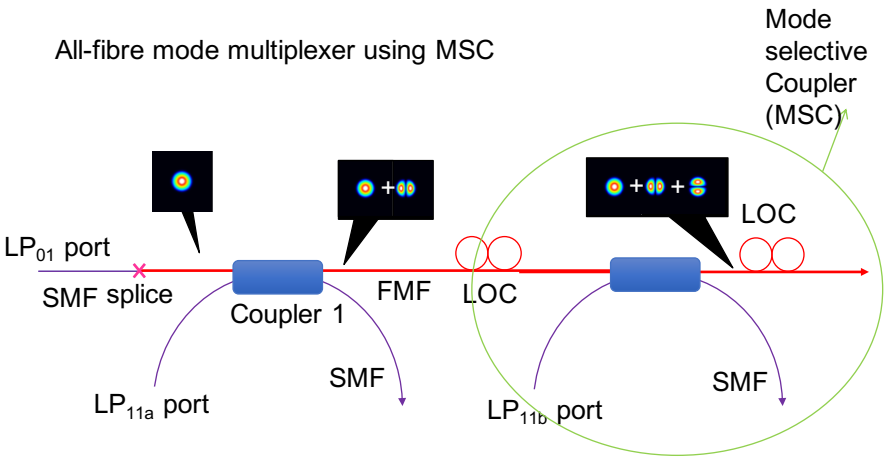

Figure 2.2: All-fibre mode multiplexer using mode selective couplers (MSCs)

The other type of mode-multiplexers is matching the propagating constants [31–34]. This kind of multiplexers could be made by fused directional fibre couplers, which are sometimes called mode-selective couplers (MSCs). As shown in Fig. 2.2, an MSC can be comprised of an FMF arm and a SMF arm. The fundamental mode of the single-mode fibre arm will be coupled to a specific higher-order mode, e.g. $LP_{11a(b)}$, of the few-mode fibre arm, if the phase match conditions $\beta_{01}^{SMF} = \beta_{lm}^{FMF}$ is satisfied, where β is the propagation constant and l, m are mode numbers. By cascading two MSCs with an elliptical-core two-mode fibre (e-TMF) [33] or a lobe orientation controller (LOC) [31]. Like the mode-selective photonic lanterns, cascaded mode-selective couplers can be optimised to cover the entire C-band as well [35].

2.1.3 Few-mode amplifiers

In long-distance optical transmission, the amplifiers are indispensable to compensate for the loss of the fibre link. In MDM systems, optical amplifiers are also desirable for long distance transmission. To achieve this, different MDM amplifiers such as few-mode erbium-doped fibre amplifiers (FM-EDFAs) and few-mode distributed Raman amplifiers (FM-DRAs) have been proposed.

Like the conventional EDFA in single-mode WDM systems, few-mode EDFA dopes the element Erbium in a few-mode fibre. Comparing with single-mode EDFA which only amplify the fundamental mode, FM-EDFA aims to amplify all the spatial modes simultaneously. The first FM-EDFA supports three spatial modes (LP_{01}, LP_{11a} and LP_{11b}) was experimentally demonstrated in [17]. In FM-EDFA, the gain of each supported mode needs to be flattened over the C-band and the differential mode gain (DMG) needs to be minimised [36]. To satisfy these requirements, various erbium doping profiles (EDPs) have been carefully designed, such as the six-mode ring-doped profile [37], the three-mode ring structure profile [38] and the ring + central rod-doped profile [39]. Recently experiment shows a FM-EDFA supporting 5 spatial modes (LP_{01}. $LP_{11a(b)}$ and $LP_{21a(b)}$ with a flatten gain over 14dB in the entire C-band [40]. The schematic of a FM-EDFA is shown in Fig. 2.3.

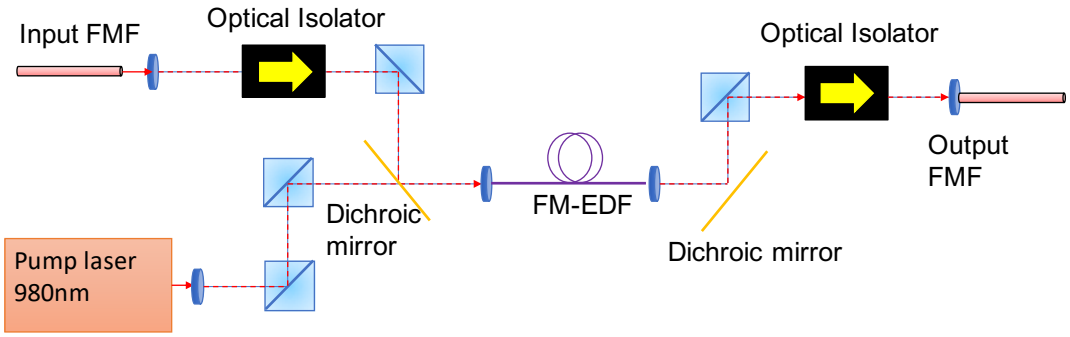

Figure 2.3: Typical schematic of a few-mode EDFA

Besides FM-EDFAs, another important type of MDM amplifier is the few-mode distributed Raman amplifiers (FM-DRAs). Back-propagated laser pump generates stimulated Raman back-scattering, which can be used to amplify forward-propagated few-mode signals. The equalised gain of different modes can be achieved by selectively coupling the back-propagated laser pump into a LP mode of the FMF. The first FM-DRA experiment was demonstrated by Bell Labs in 2011 [41], with a gain of 8dB for both LP_{01} and LP_{11} modes. More generally theoretical analysis for Raman amplification in few-mode fibres can be found in [42].

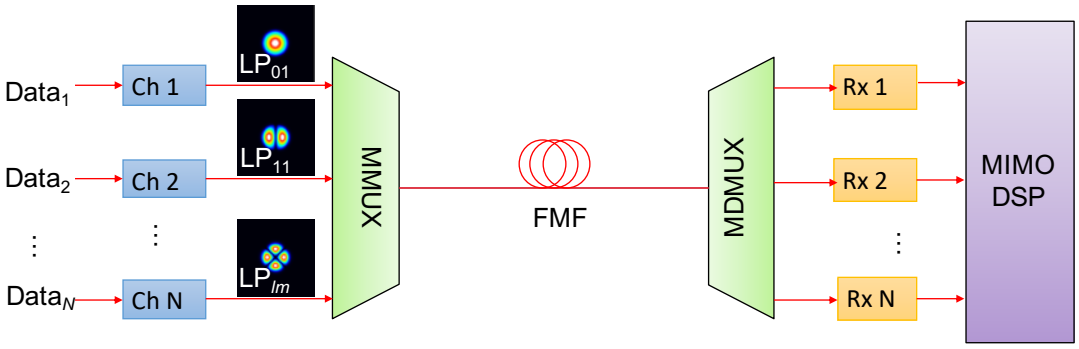

Figure 2.4: A typical MDM transmission system with FMF.

2.1.4 Few-mode transmission system

An SDM transmission system usually contains the few-mode fibre, the transmitter, the receiver and a pair of mode multiplexer and de-multiplexer. For long-distance transmission system the amplifier is also required. As a typical example, Fig. 2.4 shows the schematic of an MDM transmission with FMF. To transmit signals through N independent modes, at least N transmitters and N receivers are required. The MMUX and MDMUX are used for combining and separating different modes at the ends of the FMF channel. Due to the mode coupling in the fiber channel, MIMO DSP is required to eliminate the channel linear impacts such as the modal dispersion and modal coupling. A detailed experimental setup of a MDM transmission can be found in [39]. It contains 146 WDM channels, each of which carries 19 Gbaud dual polarizations QPSK signal within three LP modes. The few-mode EDFA and recirculating loop allow the total transmission length reaches over 1000 km. Mode (de)multiplexer and loop switch based on free-space components are used. The total capacity of this transmission system is 26.63 Tb/s. A brief summary of mode-division-multiplexing transmission systems is given in Table 2.1. A remarkable experiment conducted recently [43] demonstrated the three-mode transmission over 3500 km with a total net capacity of 9.9 Tb/s. Another recent work [44] demonstrated a MDM transmission system over one of the cores of the few-mode multi-core fibre (FM-MCF). With the help of 6-mode EDFA and the lens-coupled fan-in and fan-out (FIFO) device, the total capacity of 266.1-Tbit/s has been achieved with 6-mode 580-wavelength over a distance of 90.4 km.

Table 2.1: A brief summary of mode-division-multiplexing transmission systems

Fibre type	Spatial mode	Distance km	Mod. format	Amp. type	MMUX type	Data rate Gbps	WDM channel	Net capacity Tb/s	Reference
FMF	2	4.5	OFDM	NA	FS	107	1	0.2	[23]
FMF	2	40	QPSK	NA	FS	112	1	0.21	[27]
FMF	3	33	QPSK	NA	FS	112	6	1.86	[22]
FMF	3	50	QPSK	FM-EDFA	FS	112	88	27.23	[17]
FMF	3	96	QPSK	NA	FS	80	1	0.22	[45]
FMF	3	1200	QPSK	3×SM-EDFA	FS	80	1	0.19	[24]
FMF	3	85	QPSK	FM-EDFA	FS	112	1	0.31	[46]
FMF	3	209	QPSK	FM-DRA	FS	80	5	1.1	[47]
FMF	3	119	16QAM	MM-EDFA	FS	256	96	57.6	[48]
FMF	6	130	QPSK	6×SM-EDFA	PL	80	8	3.07	[25]
FMF	6	177	16QAM	6×SM-EDFA	PL	160	32	24.58	[49]
FMF	3	500	QPSK	FM-EDFA	FS	76	146	26.63	[39]
MMF	6	17	QPSK	NA	PL	120	1	23	[50]
FMF	3	1000	QPSK	FM-EDFA	FS	28	1	NA	[51]
MMF	15	22.8	QPSK	NA	PL	30	12	NA	[52]
FMF	6	74	OFDM	NA	PL	6.8	255	16.8	[53]
FMF	3	560	QPSK	6×SM-EDFA	MSC	120	32	NA	[32]
EC-FMF	2	2	QPSK	NA	FS	100	1	NA	[54]
FMF	3	1050	QPSK	FM-DRA	PL	NA	60	18	[55]
FMF	3	20	OOK	NA	PL	10	1	NA	[56]
EC-FMF	3	1	OOK	NA	FS	10	1	NA	[57]
FMF	3	3500	QPSK	3×SM-EDFA	PL	NA	33	9.9	[43]
FMF	3	75	QPSK	FM-DRA	FS+PL	20	1	NA	[58]
FMF	3	30	64QAM	NA	MSC	24.5	381	280	[59]
FMF	3	1045	16QAM	3×SM-EDFA	MSC	24.5	348	159	[60]
FM-MCF	6	90.4	16QAM	FM-EDFA	FS	12	580	266.1	[44]

2.2 Dispersion control in MDM transmission

Dispersion is a physical phenomenon that a light pulse spreads out when propagates along the fibre. In single-mode fibre, chromatic dispersion (CD) and polarisation mode dispersion (PMD) are two major kinds of dispersion. In MDM transmission system, modal dispersion (MD) becomes another important issue that needs to be carefully engineered.

2.2.1 DMD in few-mode fibres

The modal dispersion in few-mode fibres can be characterised by the differential mode delay, or called DMD. The propagation constant of a spatial mode μ in few-mode fibre can be written as the Taylor expansion that [61]:

$$\beta_\mu(\omega) = \beta_{0,\mu} + \beta_{1,\mu}(\omega - \omega_0) + \frac{1}{2}\beta_{2,\mu}(\omega - \omega_0)^2 + \cdots \tag{2.2}$$

where

$$\beta_{m,\mu} = \left(\frac{d^m \beta_\mu}{d\omega^m}\right)_{\omega=\omega_0} \tag{2.3}$$

For uncoupled modes, the group delay is related to the first-order derivative of the Taylor expansion of the propagation constant, i.e. $\beta_{1,\mu} = d\beta_\mu / d\omega|_{\omega=\omega_0}$. The actual value of group delay τ_μ is the product of the distance L and the first-order derivative of beta, i.e. $\tau_\mu = \beta_{1,\mu} L$. For coupled modes, however, group delay is related to field transfer matrix $\mathbf{M}(\omega)$ [62]. Assuming that the field transfer matrix can be decomposed as $\mathbf{M}(\omega) = \mathbf{U}\boldsymbol{\Lambda}(\boldsymbol{\omega})\mathbf{V}$, where $\mathbf{U}$ and $\mathbf{V}$ are two unitary matrices and

$$\boldsymbol{\Lambda}(\omega) = \mathrm{diag}[\exp(-j\omega\tau_1), \cdots, \exp(-j\omega\tau_N)]. \tag{2.4}$$

The group delay vector $\boldsymbol{\tau} = [\tau_1, \tau_2, \ldots \tau_N]^T$ can be obtained by calculating the eigenvalues of $j[d\boldsymbol{\Lambda}(\omega)/d\omega]\boldsymbol{\Lambda}^+(\omega)$. Some literature define DMD as the maximal discrepancy among all the group delays, i.e.:

$$\mathrm{DMD}_{\max} \triangleq \max(\boldsymbol{\tau}) - \min(\boldsymbol{\tau}). \tag{2.5}$$

This definition of DMD is usually called as the *maximal DMD*. Another definition uses the standard derivation (std) of the group delays, i.e:

$$\mathrm{DMD}_{\mathrm{std}} \triangleq \mathrm{std}(\boldsymbol{\tau}) = \sqrt{\frac{1}{N}\sum_{i=1}^{N}(\tau_i - \bar{\boldsymbol{\tau}})} \tag{2.6}$$

where $\bar{\boldsymbol{\tau}}$ is the mean value of vector $\boldsymbol{\tau}$. This definition is usually treated as the *std DMD* Compared with the maximal DMD, this definition has the better statistical properties. It is noted that the maximal DMD and std DMD are strongly correlated [63]. The maximal DMD will directly affect the DSP complexity (which will be discussed in the following section), while the std DMD is more suitable for the FMF channel with mode coupling. In this thesis, if there is no special instruction, the DMD is refer to the definition in Eq. (2.6).

2.2.2 MIMO DSP complexity

In MDM transmission system, the guided modes suffer from both DMD and modal crosstalk. While propagating along the fibre, the modes (especially the degenerate modes) will mix with each other through the mode coupling effect, and the DMD will largely accumulate with the distance. This will induce severe inter-symbol interference (ISI), which can hinder the performance of MDM transmission. Therefore, multiple-input and multiple-output (MIMO) equalisation has to be deployed to compensate the DMD, as well some linear channel effects.

The operations and realisation of MIMO DSP has been elaborately reported in [45,64, 65]. Here, we would like to focus on its complexity. For an MDM system transmitting N spatial modes, the DMD and mode coupling will be compensated by a $N \times N$ equaliser. The DMD equaliser needs an array of $N \times N$ filters. Each filter in the DMD equaliser requires a temporal memory $\Delta T_{\mathrm{DMD}} = \eta_N \mathrm{DMD}_{\mathrm{max}}$, where η_N is a constant related to the number of modes and confidence interval. The number of filter taps for each temporal memory will be [63]:

$$N_{\mathrm{DMD}} = [\Delta T_{\mathrm{DMD}} R_o R_s] = [\eta_N R_o R_s \mathrm{DMD}_{\mathrm{max}}] \tag{2.7}$$

where R_o is the oversampling rate and R_s is symbol rate.

The MIMO equalisation can be conducted in either the time-domain or the frequency-domain. The complexity of MIMO DSP can be quantitatively estimated by the number of complex multiplications (CM) every symbol. For a time-domain equaliser (TDE), the DSP complexity can be expressed as

$$CM_{\mathrm{TDE}} = NR_o\eta_N \mathrm{DMD}_{\max} \tag{2.8}$$

For a frequency-domain equaliser (FDE), the complexity is given as [63]:

$$CM_{\mathrm{FDE}} = R_o \frac{N_{\mathrm{FFT}} \log_2(N_{\mathrm{FFT}})N + N_{\mathrm{FFT}}N^2}{(N_{\mathrm{FFT}} - \eta_N \mathrm{DMD}_{\max} + 1)N} \tag{2.9}$$

where N_{FFT} is the number of FFT taps. Note that N_{FFT} is usually required to be the positive integer power of 2, i.e. $N_{\mathrm{FFT}} = 2^m, m \in \mathbb{Z}^+$. No matter TDE or FDE is selected, eqs. (2.8) and (2.9) clearly show that the MIMO DSP complexity is strongly related with the differential mode delay in the few-mode fibre. When the DMD is large enough, the MIMO-DSP can be too complicated to compensate the modal dispersion. Therefore, to recover the transmitted signal, as well as to reduce the MIMO DSP complexity, the DMD in FMF is expected to be as low as possible.

2.2.3 Methods for DMD reduction in FMF

Literature has reported several methods to control the DMD in FMF, which can be concluded into three different types:

Fibre profile optimisation

Since DMD in few-mode fibres is strongly related by the fibre profile and LP transverse mode pattern, one possible approach to reduce DMD is to optimise the fibre profile. There are two types of fibre profiles which are used to control the DMD:

The first one is multi-layer step-index (ML-SI) profile, which is demonstrated in Fig. 2.5(a). By adjusting the index and radius of each layer, the group delay difference between LP_{01} mode and LP_{11} mode can be flexibly tuned from positive value to negative

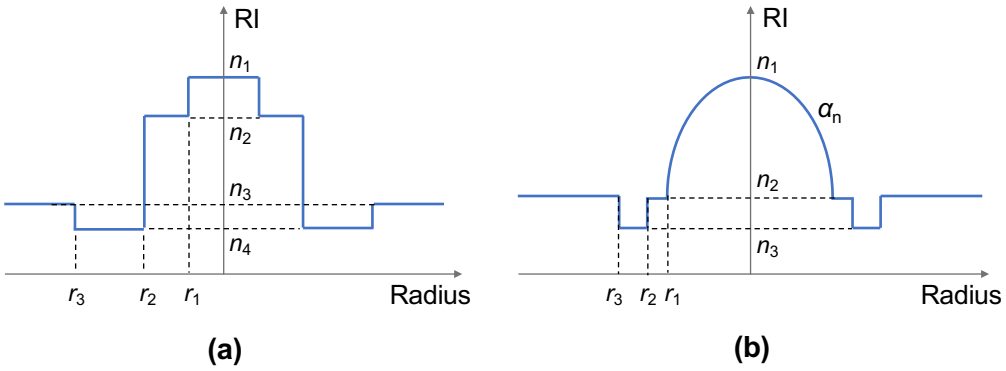

Figure 2.5: Typical fibre RI profiles for (a) multi-level step-index and (b) trench-assisted graded-index few-mode fibres

value, including zero at a certain wavelength [66]. The other type is the trench-assisted graded-index profile, shown in Fig. 2.5(b). A trench layer is added outside the core, aims to reduce the loss of higher-order LP modes and tune the DMD values. By carefully adjusting the shape alpha parameter α_n and the refractive indices, the difference of group delays can be adjusted from positive value to negative value over the C band as well. Comparing with the multi-layer step-index profile of FMF, the trench-assisted graded-index profile of FMF is more like the profile of a standard multi-mode fibre. Therefore this kind of few-mode fibre can be manufactured by scaling the preform of a multi-mode fibre during the drawing process [67].

Table 2.2: Refractive index profile of the two-mode fibre.

Profile type	LP modes	Length	Designed DMD	Measured DMD	Ref.
ML-SI	2	20.4 km	≈ 0	$\approx \pm 400$	[66]
TA-GI	2	30 km	0.3 ps/km	76 ps/km	[68]
TA-GI	2	4.45 km	8.6 ps/km	85 ps/km	[69]
TA-GI	6	4.44 km	25 ps/km	155 /ps/km	[67]

Both methods can tune the DMD values from positive to negative. Almost zero DMD at a certain wavelength is also possible by carefully design the fibre profiles. However, the actual DMD is strongly affected by the fabrication variations. Table 2.2 shows some results of FMF fabrication. We can find that even the DMD is optimised to a very small value, the measured DMD is still much larger than the designed number. For example,

a 9-LP mode few-mode fibre which supports 15 spatial modes has been reported, with a designed DMD of 25 ps/km and a measured DMD of 155 ps/km [67]. Thus, this kind of method is very sensitive to the fabrication tolerance.

DMD management

The second approach to reducing the DMD in fibre link is called DMD management or DMD compensation. The approach compensates the total accumulated DMD by interconnecting fibres with positive and negative DMD [70], which is familiar to the compensation of chromatic dispersion in SMF transmission. Fig. 2.6 shows an example of DMD compensation in two-mode fibre given in reference [70]. The fibre link comprised many fibre segments, each of which has the identical length. The DMD of red fibre segment (Fibre 1) is the same in magnitude as of Fibre 2 but opposite in sign. So, if there is no mode coupling in the fibre or the splice point, the accumulated DMD in two concatenated fibre (Fibre 1 + Fibre 2) will result in zero.

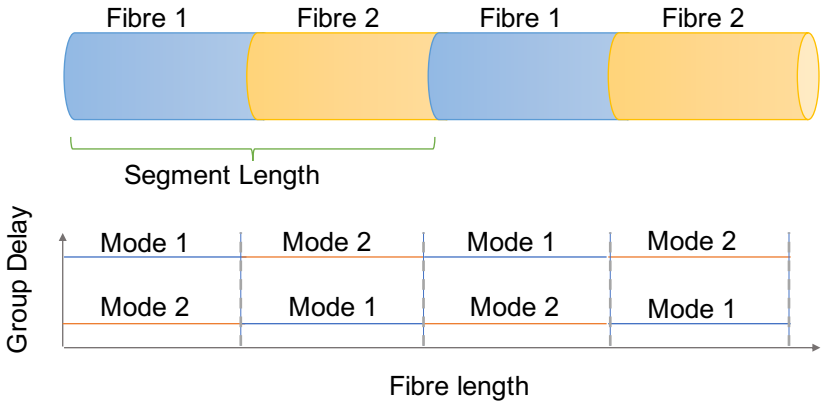

Figure 2.6: Fibre link configuration for a typical DMD management scheme [70].

However, if there is mode coupling in the fibre, the accumulated DMD will not be zero anymore. The DMD spread will act like a combination of square root function added by a sawtooth shape. Detailed analysis of DMD compensation with random mode coupling can be found in [71]. Since the environmental perturbation and vibration will influence the longitude variation of fibre refractive index, mode coupling is unavoidable. Therefore, DMD compensation scheme may only be effective for short or middle range SDM transmission [72].

Strong mode coupling

The third possible approach is introducing strong mode coupling in few-mode fibres. When the transmitted modes are strongly coupled, every independent signal has the same chance to pass both on fast and slow mode path. Therefore, each mode will have similar DMD during transmission. In a strong coupling regime, the mean DMD will scale with the square-root of the fibre length. For instance, assuming that a two-mode fiber has the DMD of 2 ps/m, therefore the DMD will be accumulated up to 200 ns over a transmission distance of 100 km, which is very difficult for MIMO DSP. In the strong mode region, however, the accumulated DMD will be only around 632 ps over 100 km distance. Detailed derivation of this property in a two-mode fibre can be obtained in a similar way as the polarisation mode dispersion which was widely studied in single-mode fibre [73]. For few-mode fibres support over three LP modes, strong mode coupling is usually classified as the intra-group coupling and inter-group coupling. The intra - group coupling is defined as the coupling within the same mode groups and the inter-group coupling is defined as the various mode groups. Since the (degenerated) LP modes in the same mode group have the similar propagation constant, intra-group coupling can be easily obtained by adding distributed perturbation such as spinning the fibre during the drawing process [74]. The inter-group coupling, however, is much more difficult to achieve. If the fibre is placed in a relatively stable environment, inter-mode coupling will not even happen after several hundreds of transmissions. Thus, it is desirable to design methods to guarantee strong mode coupling between different mode groups. Comparing with DMD management method, strong mode coupling is proven to be useful to improve the mode dependent loss (MDL) [75].

2.3 Recent progress of few-mode fibre sensors

Besides optical transmission, distributed fibre sensing is another important application with optical fibres. While the few-mode fibres have attracted much attention in spatial-division multiplexing, researchers have also shown the growing interest in FMF-based optical fibre sensors.

2.3.1 Few-mode distributed temperature sensors

Raman distributed temperature sensing (DTS) has been intensively studied in a wide variety of industrial and scientific areas [76, 77]. It is based on the spontaneous Raman scattering (SpRS) in optical fibres. However, the SpRS power is rather weaker (-60∼70 dB lower) than the input probe light. Moreover, the maximum input probe power is limited by the threshold of stimulated Raman scattering (SRS). As a solution, conventional Raman DTS adopts the MMF as the sensing medium. Since the MMF has a much larger core diameter, it can increase the Raman backscatter power, as well as the allowable peak power for input probe. But the sensing range is limited, due to the deterioration of resolution caused by modal dispersion. For long-range sensing , RDTS based on SMF has been proposed [78]. Compared with MMF, SMF has a smaller loss factor. Since it only supports one mode, the spatial resolution could survive without mode dispersion. However, the core-diameter of SMF is smaller than MMF, resulting in a lower input power and weaker SpRS. As a solution, advanced pulse coding technique has been proposed to enhance the SNR [79], but the system configuration is rather complicated and costly.

Recently, Raman DTS with few-mode fibres was proposed [80], as a trade-off between the SMF and MMF. The fibre under test was consisted by a graded-index two-mode fibre and a four-mode step-index fibre. Pump pulses were sent in the quasi-single mode (QSM), i.e. using the LP_{01} mode only and suppressing all the higher-order modes. 20-km DTS was demonstrated, with a spatial resolution of 3 metres and 4°C improvement on temperature resolution. Reference [81] reports a long-distance RDTS over a 25-km specially designed graded-index FMF. By optimising the FMF profile, the DMD can be minimised with a desired effective area A_{eff}. Under the few-mode operation, i.e. filling the power in all the spatial modes below the SRS threshold, a good performance of 4°C temperature resolution and 1.13-m spatial resolution was achieved. Under the QSM operation, the spatial resolution turned to 4.7°C, which is superior to the single-mode fibres.

2.3.2 Few-mode distributed shape sensing

Shape sensing, or the curvature measurement, is an important issue in a variety of applications such as the reverse engineering, product inspection and medical diagnosis [82]. Conventional shape sensors are based on long-period gratings [83], fibre Bragg gratings [84], Sagnac loops [85] and interferometers [86]. However, all these approaches can only sense single or only several points, lacking the capability for monitoring the distributed shape variation.

This problem, however, can be solved wi/th few-mode fibres. Ref. [87] reports few-mode fibre based distributed curvature sensor based on a BOTDA system operating at QSM. When the fibre is naturally curved, i.e. under uniform temperature and without extra longitudinal stress, both the lateral beam displacement and the bending strain will happen in the FMF, resulting in a bending-induced Brillouin frequency change (BFS) which can be read out through a typical BOTDA system. This technique can also be a hybrid with other technology. In [88], this QSM Brillouin shape sensor is combined with a QSM Raman DTS. The hybrid system can monitor the temperature and curvature distributedly, with 1.5-m spatial resolution over 2 km distance.

2.3.3 Brillouin-based few-mode discriminative sensing

As we stated in section 1.1.3, Brillouin-based fibre sensors, have faced a challenging problem to discriminate temperature and strain, or other parameter applied to the FUT simultaneously. The reason is that the Brillouin frequency shift (BFS), which is main interrogated parameter in Brillouin sensors, has a linear response to to both the temperature and strain. Therefore it is theoretically impossible to separate these two effects by using BFS only.

To solve this problem, many approaches have been proposed. One simple method uses a specially designed cable containing two fibres, one of which is kept in loose condition so that it is sensitive to temperature only. However, it cannot always guarantee the strain decoupling in a real environment. The hybrid sensing system [89] has also been considered as a possible solution, but it will considerably increase the system complexity

and cost. The other approach utilise additional information along with the BFS simultaneously, in both single-mode fibre (SMF) [90, 91] and polarisation maintaining fibre (PMF) [92, 93]. They have demonstrated the feasibility for temperature/strain separation, but the system is rather complicated. Another approach is to use multiple Brillouin peaks in the photonic crystal fibre (PCF) [94], the large effective area fibre (LEAF) [95], and the specially designed fibres with inverse-parabolic [96] or M-shaped [97] profiles. The multiple Brillouin peaks correspond to the interaction between fundamental optical mode with higher order acoustic modes, with distinct properties to multiple parameters. But the small discrepancy between the temperature and strain coefficients leads to an unfavourable discriminative error.

Recently, few-mode fibres have been considered as a promising solution for multi-parameter distribution sensing. In ref. [98], our group proposed a few-mode BOTDA scheme for simultaneous measurement of temperature and strain. By comparing the temperature and strain coefficients of LP_{01} mode and LP_{11} mode, two-parameter sensing of temperature and strain was successfully demonstrated over a 3-km customer designed FMF with the discriminative accuracy of 1.2°C and 21.9$\mu\varepsilon$. In [99, 100], a single-ended few-mode BOTDR scheme was proposed. Compared with BOTDA, BOTDR can have access to the tested fibre from one side, which will bring much convenience in practical application. Such an approach was demonstrated over a two-mode fibre with a 5-m spatial resolution. In [101], the Brillouin dynamic gratings (BDG)-based Brillouin sensors was proposed showing its potential for multi-parameter measurement. That system was demonstrated over 95 meters with a 5m spatial resolution. The temperature and strain errors are $\pm 105\mu\varepsilon$ and ± 1.6°C, respectively.

2.4 Other attractive fields in distributed fibre sensing

We have reviewed the recent progress of few-mode fibre sensors as a new-type distributed fibre sensing technology. Nevertheless, optical fibre sensors using conventional single-mode fibres have also achieved a remarkable progress in the past decades. Besides few-mode fibre or the space division multiplexing, there are some other attractive fields

in distributed fibre sensing:

2.4.1 Advanced pulse coding technology

Optical time-domain distributed fibre sensors, such as OTDR, ROTDR, BOTDR, and BOTDA, are pulse-based systems. By sending an optical pulse into the fibre and detecting the backscattering signal, distributed physical parameters can be monitored. For long-distance fibre sensing, the received power is quite weak for effective detection. In optical fibres, the peak pump power is limited by nonlinear thresholds. Although sending a broader pulse can boost the total pump power, the spatial resolution will be degraded. Therefore, there is a trade-off between the received SNR and spatial resolution.

Pulse coding is an effective technique to overcome this trade-off. This technology spreads the probe energy in the time-domain by using properly coded pulse sequences, resulting in a much higher SNR without deteriorating the spatial resolution [102].In the past decade, various pulse coding techniques have been proposed to improve the distributed fibre sensors. In [103], 255-bit Simplex pulse coding method was proposed to use in the Raman OTDR system, with an enhancement of sensing distance over 19.5 km. In [104], the simplex pulse coding was applied in the BOTDR-based DTS, with the help of Landau-Placzek Ratio (LPR). Ref. [105] reported a BOTDA system with 511-bit Simplex pulse coding, and achieved a 1-m spatial resolution over 50 km SMF. Cyclic simplex pulse coding, which is a simpler coding technique, has been applied in RDTS [78], BOTDA [106,107], Coherent ϕ-TDR[108], and the Raman/Brillouin hybrid sensing systems [109]. Cyclic pulse coding based on pseudo-random sequence has also shown in [110], which can considerably improve the resolution and distance in the DTS system.

2.4.2 Distributed dynamic sensing

In the past few years, distributed dynamic sensing (DDS), which records fast strain (or vibration) variation along the fibre, has become a hot topic. This research field is driven by the growing demand in gas and oil industries, geophysical science and the structural health monitoring [111]. Conventional Brillouin sensing systems, such as BOTDA,

usually require a large number of measurements to complete each time, including scrambling the polarisation, averaging the signals and scanning the frequency. So the sensing process is quite time-consuming, ranging from tens of seconds to tens of minutes. Furthermore, it assumes that the fibre status (strain and temperature) shall remain unchanged during these measurements; otherwise, the distributed Brillouin spectra may not be correctly reconstructed. Thus it is applicable for monitoring the dynamic change along a long-range distance.

Several methods have been proposed to reduce the measurement time for distributed dynamic sensing. In [112], a slope-assisted BOTDA technique was proposed, utilising the slope of the SBS gain profile for measuring a few hundred Hertz. Ref. [113] extended this technique with a frequency-agile method, which will increase the dynamic range of vibration measurement. Ref. [114] demonstrated a fast frequency-swept method in BOTDA, which realised a dynamic measurement over 100 m fibre. In [115], a sweep-free BOTDA technique was proposed, to reduce the measurement time by eliminating the frequency sweeping process. The optical frequency comb technique was proposed in [116], which adopted the digital-generated optical frequency comb to measure the Brillouin spectrum without frequency scanning, resulting in a greatly improved sensing speed which is suitable for distributed dynamic sensing.

2.4.3 High-performance Brillouin information extraction

Brillouin frequency shift (BFS) is a key parameter in Brillouin-based distributed fibre sensors, and is directly related with the measurement accuracy. A lower BFS uncertainty means a higher measurement resolution for the sensors. Therefore, how to improve the BFS accuracy has become a quite attractive field. In a typical BOTDA or BOTDR system, the BFS is estimated by the gain profile. Curve fitting methods, like the Lorentzian curve fitting for the Brillouin gain/loss spectrum, have been widely adopted in Brillouin fibre sensors. But the curve fitting method requires a proper selection of initial status. In addition, the signal processing time for curve fitting is quite time-consuming. For example, in a commercialised BOTDA, the Brillouin signal processing time could be comparable to the measurement time (according to the author's test with the off-the-shelf

product). Therefore, how to estimate the BFS with high accuracy is an interesting topic in distributed Brillouin fibre sensors.

Recently, with the rapid development of artificial intelligence, researchers start to explore the applications of machine learning in the fibre sensing area. In [117], an artificial neural network (ANN) was employed in the signal processing for BOTDA sensor system. Results show that ANN has a higher accuracy and larger error tolerance compared with the conventional curve fitting method. Reference [118] used the support vector machine (SVM) in the BOTDA system for ultra-fast temperature extraction. Both simulation and experiment are conducted, resulting in a 100 times faster than the conventional Lorentzian curve fitting method. Compared with ANN, SVM requires a shorter training time. Ref. [119] demonstrated the simultaneous temperature and strain measurement along a large-effective-area fibre, assisted by the deep neural networks (DNN) in data processing procedure, while ref. [120] reported another method for temperature and strain discrimination with a conventional BOTDA with the convolutional neural network (CNN) technique. As a general point of view, machine learning-based techniques can significantly boost the data processing time, though some training time is required. Meanwhile, how to prepare the training data in practice is still an issue that needs to be carefully investigated.

Chapter 3
Low-DMD FMF for Optical Transmission

3.1 Motivation

In MDM transmission system, the transmitted signal will suffer from the accumulated DMD in the fibre link, which is strongly related to the MIMO DSP complexity. In order to fully recover the transmitted signal and reduce the DSP complexity, FMF with low DMD is desired. As we discussed in section 2.2.3, there are three methods to control the DMD in FMF: (1) manufacture FMF with low DMD, (2) DMD management, and (3) strong mode coupling. In this chapter, we focus on the approach that using strong mode coupling to reduce the DMD in few-mode fibres. We study a novel scheme called distributed grating-(assisted) few-mode fibre (DG-FMF), which is introduced with strong mode coupling between supported LP modes by adding long period grating (LPG) with random direction distributively along the whole fibre. The basic idea of this scheme comes from the fact that when manufacturing fibre gratings, no matter by side-illumination of UV light or CO_2 lasers, will introduce an asymmetric refractive index variation in the fibre cross section. This distribution will result in the non-zero overlap integral between the fundamental mode and the higher order modes, and thus the strong mode coupling can be induced. In our proposed schematic, the entire transmission fibre is distributively inscribed with this kind of LPGs. To ensure that the mode coupling is uniform over a long distance, the exposed direction of LPG is randomised with a certain interval. This chapter is orgainised as follows: section 3.2 presents the design of our proposed low-DMD DG-FMF. Section 3.3 introduces the coupled mode equation for the LPG with random

rotations. The fibre channel model in our scheme will be discussed in section 3.4, while we will study its performance of DMD reduction, as well as its efficient bandwidth and the working range of temperature in section 3.5. Finally the work in this chapter will be summarised in section 3.6.

3.2 Design of Low-DMD DG-FMF

Without loss of generality, consider a two-mode fibre which supports LP_{01}, LP_{11a} and LP_{11b} modes. we assume the few-mode fibre is circular and isotropic. LP_{11a} and LP_{11b} are assumed to have the identical propagation constant. Although the higher-order intra-LP modes do have slight DMD, but do not present a problem as significant as that from inter-LP, and therefore intra-modal dispersion is ignored in our analysis. To guarantee strong mode coupling between LP_{01} and $LP_{11a(b)}$, the refractive index change introduced by gratings on the cross section must be asymmetric, otherwise the overlap integral will be zero. In practice, conventional LPGs manufactured by single side illumination, no matter exposed by CO2 laser or UV light, always have an asymmetric refractive index distribution [38,39]. To demonstrate our DG-FMF scheme, the UV-side-illumination model is chosen to describe the index distribution. As shown in Fig. 3.1 (a), the fibre is exposed by UV beam at an angle of ψ, and the relative refractive index change along the symmetric axis is depicted in Fig. 3.1 (b). The fibre is consisted of many grating sections, each of which is made with various angle ψ and identical period Λ, as shown in Fig. 3.1 (c).

The refractive index distribution of each grating section with the angle ψ can be derived from the one with left-side exposure, we first analyse the grating with $\psi = 0$. In this case, refractive index change of LPG can be described as:

$$\Delta n_g(x, y, z) = \Delta n_g(x, y) \left[1 + \cos\left(\frac{2\pi z}{\Lambda}\right)\right], \tag{3.1}$$

where Λ is the grating period and $\Delta n_g(x, y)$ is the cross-section refractive index variation with following exponential shape as:

$$\Delta n_g(x, y) = \Delta n_g \exp\left[-\rho\left(\sqrt{a^2 - y^2} - x\right)\right], \tag{3.2}$$

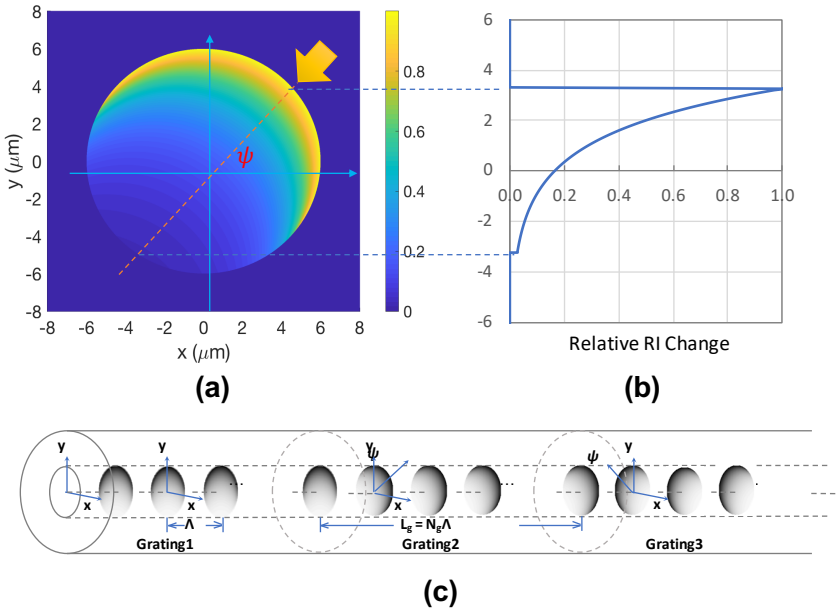

Figure 3.1: (a) Relative refractive index change in the cross-section. (b) Relative refractive index along the symmetric axis. (c) Schematics of distributed grating-assisted few-mode fibre.

where parameter ρ determines the asymmetric shape of the index profile, and a is the core radius. Δn_g is the grating strength. The coupling among LP modes can be calculated by the coupling coefficients written as:

$$K_{v-\mu}(z) = \left[1 + \cos\left(\frac{2\pi z}{\Lambda}\right)\right] \cdot \zeta_{v-\mu}, \tag{3.3}$$

where $\zeta_{v-\mu}$ is a z-independent coefficient expressed as in [121] that

$$\zeta_{v-\mu} = \frac{n_1 \omega \epsilon_0}{2} \iint \Delta n_g(x,y) E_v(x,y) E_\mu(x,y) dxdy, \tag{3.4}$$

where $E_v(x,y)$ and $E_\mu(x,y)$ are normalised electric fields of mode v and μ respectively. ω is the angular frequency of light and ϵ_0 is the dielectric constant in vacuum. Parameter n_1 is the refractive index of the core. Assuming that the core radius is 6 μm, $\omega = 1.2153 \times 10^{15}$ rad/s (for 1550 nm), $n_1 = 1.4525$, and the cladding is pure silica. Fig. 3.2 shows the relationship between $\zeta_{v-\mu}$ and ρa. We find that the coupling between LP_{01} and LP_{11a}

has a maximal value when ρa equals to 1.32. Moreover, the coupling coefficients of LP_{01}-LP_{11b} and LP_{11a}-LP_{11b} are both zero, meaning no coupling between these modes exists when the fibre is left-side illuminated.

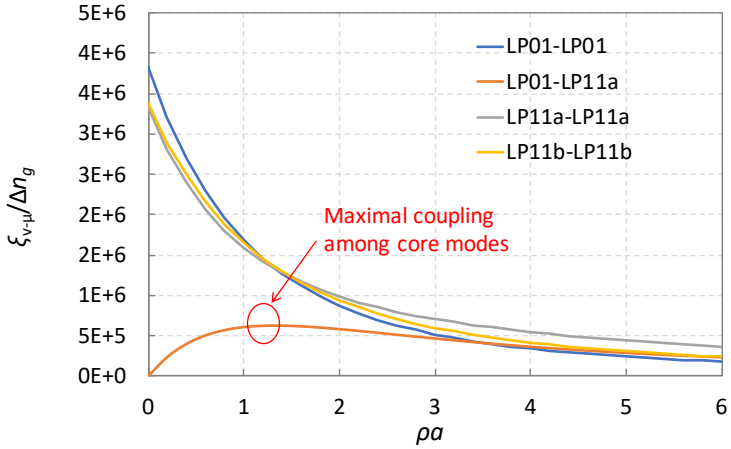

Figure 3.2: Mode coupling ratio versus the product of ρ and a.

3.3 Coupled mode equations

The field coupling among LP modes in the LP G can be described by the following coupled mode equations (CME) [121]:

$$\frac{d}{dz}\mathbf{A}(z) = -\left[\frac{\alpha}{2}\mathbf{I} + j\mathbf{\Gamma}(z)\right]\mathbf{A}(z), \tag{3.5}$$

where vector $\mathbf{A}(z) = [\mathbf{A}_{01}(z), \mathbf{A}_{11a}(z), \mathbf{A}_{11b}(z)]^T$ denotes the complex amplitude of LP modes with the implicit term $\exp(-j\beta z)\exp(j\omega z)$ and α is the loss factor in the fibre. α is the loss factor, $\mathbf{I}$ is an identity matrix. The coupling matrix $\mathbf{\Gamma}(z)$ is written as

$$\mathbf{\Gamma}(z) = \begin{bmatrix} \gamma_{01-01} & \gamma_{01-11a} & \gamma_{01-11b} \\ \gamma_{11a-01} & \gamma_{11a-11a} & \gamma_{11a-11b} \\ \gamma_{11b-01} & \gamma_{11b-11a} & \gamma_{11b-11b} \end{bmatrix}, \tag{3.6}$$

in which the non-zero elements in matrix $\mathbf{\Gamma}(z)$ are expressed as

$$\begin{aligned} \gamma_{01-01} &= \zeta_{01-01} \\ \gamma_{11a-11a} &= \zeta_{11a-11a} \\ \gamma_{11b-11b} &= \zeta_{11b-11b} \\ \gamma_{01-11a} &= \tfrac{1}{2}\zeta_{01-11a}e^{-j\pi z/\Lambda} = \gamma^*_{11a-01} \end{aligned} \tag{3.7}$$

Note that γ_{01-11b}, $\gamma_{11a-11b}$,γ_{11b-01} and $\gamma_{11b-11a}$ are zero because the RI distribution is symmetric about the x axis, resulting in the zero-overlap integrals between LP_{11b} and the two other modes. Therefore, we can obtain the analytical solution of the CME through the method described in [121], and the solution will be

$$\mathbf{A}(z_0+z) = c(z)\mathbf{H}(z)\mathbf{A}(z_0), \tag{3.8}$$

where z_0 is the initial position, $c(z) = \exp(-\alpha z)$ and $\mathbf{H}(z)$ is a unitary matrix that

$$\mathbf{H}(z) = \begin{bmatrix} h_{11} & h_{12} & 0 \\ h_{21} & h_{22} & 0 \\ 0 & 0 & h_{33} \end{bmatrix} \tag{3.9}$$

with the elements:

$$h_{11} = \exp\left[-j(\beta_0 + \frac{\pi}{\Lambda})z\right]\left[\cos(sz) - j\frac{\delta}{s}\sin(sz)\right] \tag{3.10}$$

$$h_{22} = \exp\left[-j(\beta_0 - \frac{\pi}{\Lambda})z\right]\left[\cos(sz) + j\frac{\delta}{s}\sin(sz)\right] \tag{3.11}$$

$$h_{33} = \exp[-j(\beta_0 + \chi)z] \tag{3.12}$$

$$h_{12} = -j\exp\left[-j(\beta_0 + \frac{\pi}{\Lambda})z\right]\exp\left[-\frac{2j\pi(z+z_0)}{\Lambda}\right]\frac{\kappa}{s}\sin(sz) \tag{3.13}$$

$$h_{21} = -j\exp\left[-j(\beta_0 - \frac{\pi}{\Lambda})z\right]\exp\left[+\frac{2j\pi(z+z_0)}{\Lambda}\right]\frac{\kappa}{s}\sin(sz) \tag{3.14}$$

where $\chi = \gamma_{11b-11b}$, $\beta_0 = (\beta_{01} + \beta_{11} + \gamma_{01-01} + \gamma_{11a-11a})/2$ and the detuning factor $\delta = 1/[2(\beta_{01} + \gamma_{01-01} - \beta_{11} - \gamma_{11a-11a} - 2\pi/\Lambda)]$. Parameter $\kappa = \zeta_{01-11a}/2$ and $s^2 = \delta^2 + \kappa^2$. If the LPG is made with a rotation angle ψ to the x axis, then the transfer matrix becomes

$\mathbf{M}^t(z) = c(z)\mathbf{R}(\psi)\mathbf{H}(z)\mathbf{R}^+(\psi)$ where $\mathbf{R}(\psi)$ is a rotation matrix with the following form:

$$\mathbf{R}(\psi) = \begin{bmatrix} 1 & 0 & 0 \\ 0 & \cos\psi & \sin\psi \\ 0 & -\sin\psi & \cos\psi \end{bmatrix} \tag{3.15}$$

The transmittance can be found by assuming only one certain mode is incident and calculate the ratio between the input and output power. When the phase-matching condition is satisfied, the period of LPG should be:

$$\Lambda = \frac{2\pi}{\beta_{01} - \beta_{11} + \gamma_{01-01} - \gamma_{11a-11a}}, \tag{3.16}$$

e.g. $\delta = 0$. The maximum mode conversion between LP_{01} and LP_{11a} exists when $\kappa L_{\max} = \pi/2 + m\pi, m = 1, 2, 3\ldots$, where $L_{\max} = (1+2m)\pi/(2\kappa)$ is the length of each LPG. For the convenience of the following analysis, here we assume that $m = 1$.

3.4 Fibre channel model

The fibre channel model for our proposed few-mode fibre is shown in Fig. 3.3. It is modelled as a concatenation of N_S segments, each of which is consisted of N_L LPGs with different exposed directions, and each LPG has the identical length of L_g. Orientation between fibre segments are randomised, with a random rotation angle θ_i. The transfer matrix of the ith normal few-mode fibre segment is defined as $\mathbf{M}_i(z,\omega) = \mathbf{R}(\theta_i)\mathbf{M}_i^t(z,\omega), k \in \{1, 2, \ldots, N_S\}$, where $\mathbf{R}(\cdot)$ is the rotation matrix and $\mathbf{M}_i^t(z,\omega)$ is the transfer matrix of the ith fiber segment which can be written as $\mathbf{M}_i^t(z,\omega) = \Pi_{k=1}^{N_L}\mathbf{R}(\psi_{iN_L+k})\mathbf{H}(L_g,\omega)\mathbf{R}^+(\psi_{iN_L+k})$. The total transfer matrix is written as

$$\mathbf{M}_{tot}(z,\omega) = \mathbf{M}_{N_S}(z,\omega)\mathbf{M}_{N_S-1}(z,\omega)\cdots\mathbf{M}_1(z,\omega). \tag{3.17}$$

To emulate the random perturbation in the channel, a Gaussian distributed random core rotation is introduced at the end of each segment. Hence the total transfer matrix

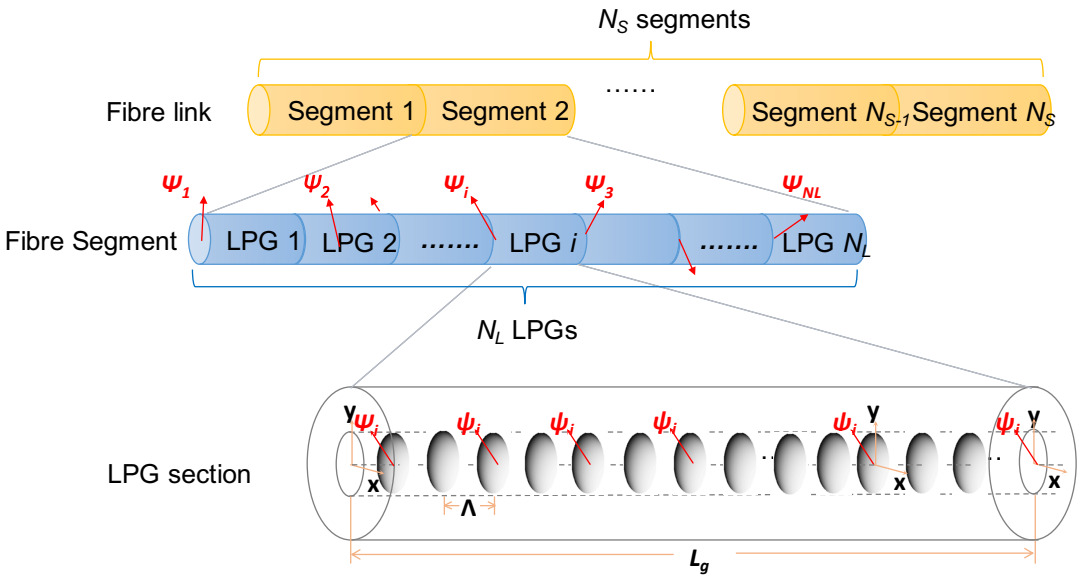

Figure 3.3: Fibre channel model for DG-FMF

will be:

$$\mathbf{M}_{tot}(\omega) = c_1 \prod_{n=0}^{N_s-1} \left[\mathbf{R}(\theta_{n+1}) \prod_{i=1}^{N_L} \mathbf{R}(\psi_{nN_L+i}) \mathbf{H}(L_g, \omega) \mathbf{R}^{+}(\psi_{nN_L+i}) \right] \tag{3.18}$$

where $c_1 = \exp(-\alpha N_S N_L L_g)$ denotes the loss of the fibre channel and $\psi_i \sim U[0, 2\pi]$ is the exposed angle of each LPG. The differential group delay can be evaluated via the group delay operator as:

$$\mathbf{G}(\omega) = j \frac{d\mathbf{M}_{tot}(\omega)}{d\omega} \mathbf{M}_{tot}^{+}(\omega) \tag{3.19}$$

which eigenvalues correspond to the group delays. For a lossless fibre, $\mathbf{M}_{tot}(\omega)$ is unitary and $\mathbf{G}(\omega)$ will be Hermitian.

The long distributed gratings in our DG-FMF can be rapidly written by drawing a FMF through a periodically intensity-modulated UV laser beam, as described in [122]. It provides an effective method to manufacture a grating of any length and to control the grating parameters, which is compatible to our scheme. Since the core of a Ge-doped optical fibre is a photosensitive waveguide, a writing beam of actinic radiation, such as a UV laser beam, is positioned to write on the fibre. A periodic intensity distribution is obtained by using an interference pattern generator (phase mask) positioned between the writing beam and the waveguide to create an interferogram of period Λ. The fibre

then is translated through the periodic intensity distribution relative to the writing beam at a precisely-controlled relative velocity $v(t)$. Alternatively, for applications requiring long-length gratings (but not limited to long-length FBGs), the fibre may be coupled to a spool which rotates to draw the fibre at $v(t)$ through the periodic intensity distribution. Finally, a modulator varies the amplitude of the beam intensity as a function of time at a frequency $f(t)$ such that $v(t)/f(t) = \Lambda$.

3.5 Performance of the proposed DG-FMF

3.5.1 Performance of DMD reduction

Based on the model we described above, numerical simulation has been performed to evaluate the DMD performance of the DG-FMF. We consider a step-index FMF with core radius of 6 μm and cladding radius of 62.5 μm, which is comparable to the existing SI two-mode fibres. The RI of GeO_2-doped core is 1.4525. The refractive indices of core, cladding and gratings for the different wavelengths are calculated with the Sellmeier equation. The effective indices of LP_{01} and $LP_{11a(b)}$ are 1.450429 and 1.447415 at 1550nm, respectively. The transition loss due to cladding mode coupling can be evaluated using the coupling coefficients and phase match conditions between the core modes and cladding modes [123]. When the coupling strength equals to 1×10^{-6}, the added transmission loss of core modes due to the cladding mode coupling is about -0.98 dB at 100-km length, which is acceptable for transmission. For each LPG, the period is set to satisfy the phase match condition at 1550 nm, e.g. $\Lambda = 514.35\mu$m. In the simulation, every LPG segment is assumed about 10 meters, and the core rotation angle θ between two neighbouring segments follows a zero-mean normal distribution with a standard deviation of $\sigma_\theta = 0.05$ rad. Note that here we choose 0.05 for simulating the weak perturbation in the fiber channel [124]. Compared with the uniform random rotation angle ψ of LPG, θ is much smaller than ψ, indicating that it does not play a significant role in the simulation. For each case, we conducted 10^4 Monte-Carlo simulations.

Fig. 3.4 shows the mean DMDs of SI-FMF without gratings, DG-FMF with $L_g = 1 \times L_{\max}$ and DG-FMF with $L_g = 2 \times L_{\max}$, respectively. When there are no gratings,

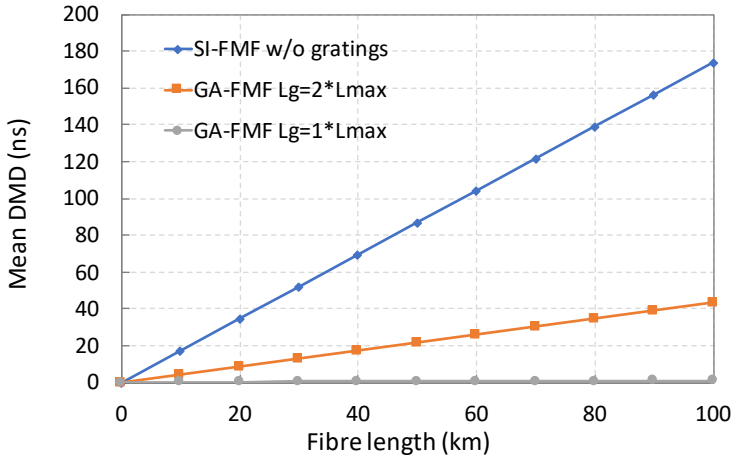

Figure 3.4: Mean DMDs as a function of the fibre length with $\Delta n_g = 1 \times 10^{-6}$.

DMD in a SI-FMF accumulates linearly to 173.71 ns at 100 km. However, when the FMF is assisted with distributed gratings of $L_g = L_{\max}$, the mean DMD will be remarkably reduced to 904.16 ps at 100 km, due to the strong mode coupling. In addition, the minimum mode conversion occurs when L_g equals to $2 \times L_{\max}$, resulting in a larger DMD than the previous one.

Fig. 3.5 shows a closer view of the DMD in the DG-FMF with different grating lengths. The mean DMDs scale with the square-root of the fibre length. DMD of $L_g = L_{\max}$ smaller than other cases because the maximal mode conversion appears at this length. Furthermore, the four DMD lines are approximately even spaced parallel with an interval of times, meaning that the mean DMD is proportional to $\sqrt{z/L_g}$ when $L_g \leq L_{\max}$, where z is the length of the fibre.

The mean DMDs with different grating strengths is demonstrated in Fig. 3.6. For each Δn_g, the grating period Λ is chosen to satisfy the phase matching condition at 1550 nm, and the LPG length is select to be $L_g = L_{\max}$ the grating strength is 5×10^{-7}, the mean DMD is about 1.27 ns at 100 km. With the increase of Δn_g from 5×10^{-7} to 4×10^{-6}, the DMD becomes lower. This is due to the coupling coefficient κ, which is proportional to the grating strength, is inversely proportional to $L_{\max}$, resulting in a smaller mean DMD. Notice that if the UV-induced effective index change is large enough, e.g. greater than 1×10^{-5}, the coupling to the cladding modes will also be enhanced, leading to a considerable

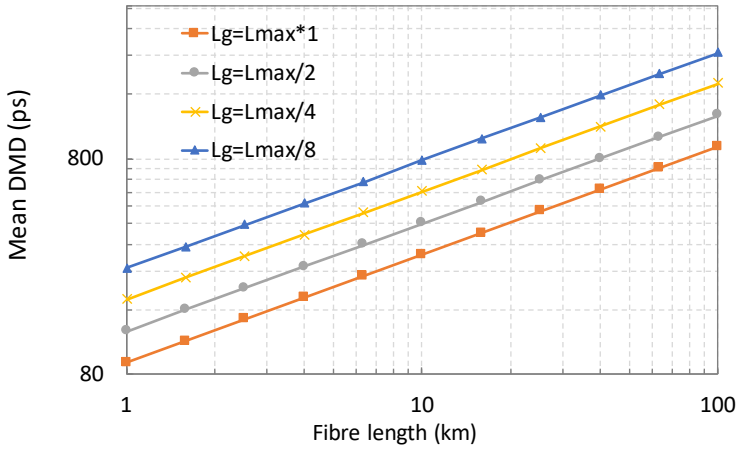

Figure 3.5: Mean DMDs in terms of the fibre length with various grating lengths of the fibre when $\Delta n_g = 1 \times 10^{-6}$.

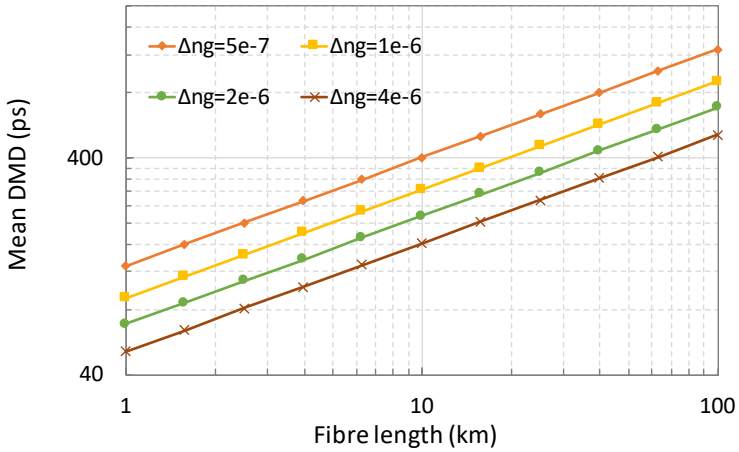

Figure 3.6: Mean DMDs in terms of fibre length with various grating strengths.

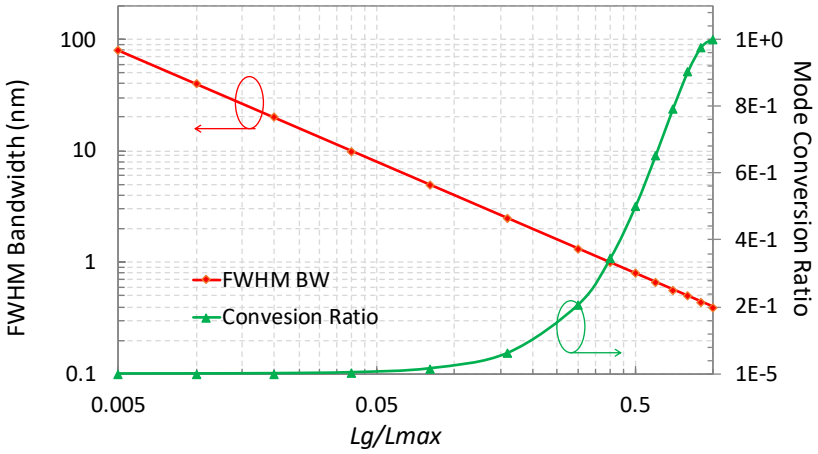

Figure 3.7: Mode conversion ratio and bandwidth (FWHM) in terms of $L_g/L_{\max}$.

transition loss in the fibre, which may not be feasible in practical transmission.

3.5.2 Bandwidth control and temperature robustness

Besides DMD, another important issue of DG-FMF is the bandwidth [125]. The mode conversion ratio and full-width half-maximum (FWHM) bandwidth of fundamental mode are shown in Fig. 3.7. Even though the maximum mode conversion occurs when the LPG length equals to $L_{\max}$ bandwidth is only 0.4 nm. Since the FWHM bandwidth is proportional to the length of LPG [123, 126], wider bandwidth can be achieved by reducing L_g. When the LPG length equals to $L_g = 0.01 \times L_{\max}$ the FWHM bandwidth will be about 40 nm, with a mode conversion ratio of 0.025%. Notice that reducing L_g will also increase the mean DMD, as we discussed above. So, there is a trade-off between DMD reduction and wideband applications.

We also evaluated the temperature sensitivity of the DG-FMF. The RI of the silica cladding is recalculated with the temperature-dependent Sellmeier equation [127], and the thermos-optics coefficients of the core and grating parts are assumed to be $1.2 \times 10^{-5}/°\mathrm{C}$ [128]. Fig. 3.8 shows the mean DMD with $\Delta n_g = 1 \times 10^{-6}$. Results indicate that our DG-FMF has a flat DMD performance from 1530 nm to 1570 nm, which covers the whole C-band. Furthermore, we find that the DMD at $-20\ °C$ is a decreasing function in the C-band, while it becomes flatter when temperature rises. This phenomenon

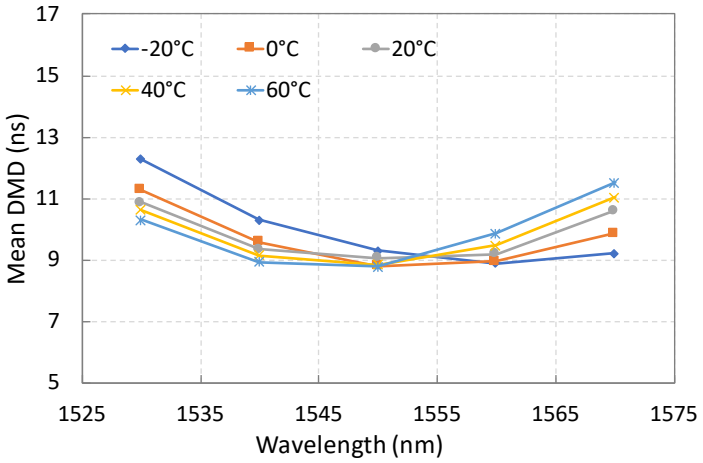

Figure 3.8: Mean DMDs of 100 km from 1530 nm to 1570 nm with various temperatures.

coincides with the revealed fact that when the temperature increases, the transmission spectrum of LPG will move to the lower wavelength [129]. At the temperature of 60 °C, the average DMD in the C-band will be around 12 ns. Although it is higher than the cases with lower temperatures, the DMD in DG-FMF at 60 °C is still much lower and easier to be processed than SI-FMF by DSP and MIMO. Therefore, our GA-FMF has a stable DMD performance and temperature robustness within C-band.

Note that although the model we discussed here is for two-mode fibre, it can be upgrade extended to a FMF supporting more modes. One possible method is to build several different types of LPGs, each of which having a different pitch designed for the phase matching of two certain modes. By randomly cascading these types of LPGs together with a random rotation, all the modes would get mixed, and strong mode coupling will be guaranteed.

3.6 Chapter summary

In summary, we have proposed a distributed grating-assisted few-mode fibre (DG-FMF) to reduce the differential mode delay (DMD). By introducing asymmetric long-period fibre gratings with random exposure directions in a step-index few-mode fibre during fibre manufacture process, the strong random mode coupling is generated along the en-

tire length of the fibre. Simulation results show that mean DMD in the DG-FMF can be reduced to less than 12 ns at a distance of 100 km with a period of 514 μm and grating strength of 1×10^{-6}. The DMD reduction in our DG-FMF is guaranteed within the entire C-band, and in a wide temperature range from -20°C to $+60^{\circ}$C. Results in this chapter have been published in [130].

Chapter 4
Multi-Parameter Sensing with FMF

4.1 Motivation

Few-mode fibres (FMFs) have attracted much attention in spatial-division multiplexing, since it can offer the potential to overcome the capacity crunch in optical transmission. Meanwhile, researchers have also shown growing interest in FMF-based Brillouin fibre sensors. Previous study demonstrates that the circular-core few-mode fibres (EC-FMFs) can be used in both BOTDA [98] and BOTDR [100] for multi-parameter sensing. The discrimination between temperature and strain is based on the Brillouin peaks of multiple input optical modes (LP_{01} and LP_{11}), which correspond to the interaction between the fundamental acoustic mode and higher order optical modes. However, the temperature and strain coefficients of the two modes only have a small discrepancy, resulting in a large amplification factor of measurement error. The elliptical-core (e-core) FMF, which has already been used in the SDM transmission [54, 57], is considered as another candidate, since it can reduce the modal fading in c-core FMFs. The stimulated Brillouin scattering (SBS) in EC-FMF has been studied [131], and the Brillouin dynamic gratings (BDG)-based Brillouin sensors has shown its potential for multi-parameter measurement [101]. However, the spontaneous Brillouin scattering (SpBS) in EC-FMF, as well as the SpBS-based EC-FMF-based multi-parameter sensor, has yet to be investigated.

This chapter is organised as follows: In section 4.2, we will introduce the principle of FMF Brillouin fibre sensors. In section 4.3, we will describe the methods for multi-parameter discrimination, including the conventional method with only two modes and the generalised solution with arbitrary number of modes. Section 4.4 will demonstrate

the experimental setup for our proposed e-core FMF Brillouin fiber sensor, and its unique SpBS properties will be characterised in section 4.5. Calibration for the temperature and strain of the e-core FMF will be performed in section 4.6, followed by the performance evaluation for this e-core FMF sensor in section 4.7. Note that the analysis in sections 4.5, 4.6 and 4.7 are different from the previous works [98, 100] which are based on the circular-core FMF. Finally, the contents in this chapter is summarised in section 4.8.

4.2 Principle of FMF Brillouin fibre sensors

The relationship between the Brillouin frequency shift (BFS) Δv_B and the temperature change (ΔT) and strain variation ($\Delta\varepsilon$) can be expressed as [132]:

$$\Delta v_B = c_T \Delta T + c_\varepsilon \Delta\varepsilon \tag{4.1}$$

where c_T and c_ε are the temperature and strain coefficients, respectively. The temperature change can be expressed using the unit °C if using Celsius degrees, while the strain (ε) can be calculated by dividing the total length deformation ΔL by the original length (L), i.e.:

$$\varepsilon = \Delta L / L, \tag{4.2}$$

which is a dimensionless variable. In fibre sensing area, the strain is very small. So strain is often expressed in the unit *micro-strain* ($\mu\varepsilon$), which equals to $\varepsilon \times 10^{-6}$. The widely used units of c_T and c_ε are MHz/°C and MHz/$\mu\varepsilon$, respectively.

The BFS of intra-mode Brillouin scattering is given by [96, 100]:

$$v_B = \frac{2n_{o,i}}{\lambda_p} V_{a,k} = \frac{V_{\text{clad}}}{\lambda_p} \frac{2n_{o,i}}{n_{a,k}}, \tag{4.3}$$

where λ_p is the wavelength of probe light, $n_{o,j}$ is the effective index of the ith optical modes, $n_{a,k}$ is the effective index of kth acoustic modes, V_{clad} is the longitudinal acoustic velocity in fibre cladding, which is around 5944 m/s. The temperature dependence of

Brillouin frequency is given by [133]:

$$\frac{dv_B}{dT} = \frac{2V_{\text{clad}}}{\lambda_p}\left(n_{a,j}\frac{dn_{o,i}}{dT} + n_{o,i}\frac{dn_{a,j}}{dT}\right) \tag{4.4}$$

while the strain dependence of Brillouin frequency is

$$\frac{dv_B}{d\varepsilon} = \frac{2V_{\text{clad}}}{\lambda_p}\left(n_{a,j}\frac{dn_{o,i}}{d\varepsilon} + n_{o,i}\frac{dn_{a,j}}{d\varepsilon}\right) \tag{4.5}$$

For inter-modal Brillouin scattering, the BFS can be expressed as [131]

$$v_B = \left(\frac{n_{o,i} + n_{o,j}}{\lambda_p}\right)V_{a,k} = \frac{V_{\text{clad}}}{\lambda_p}\frac{n_{o,i} + n_{o,j}}{n_{a,k}}, \tag{4.6}$$

The temperature and strain dependence for inter-modal Brillouin frequency become

$$\frac{dv_B}{dT} = \frac{2V_{\text{clad}}}{\lambda_p}\left(n_{a,j}\frac{dn_{o,i}}{dT} + n_{o,i}\frac{dn_{a,j}}{dT} + n_{a,j}\frac{dn_{o,j}}{dT} + n_{o,j}\frac{dn_{a,j}}{dT}\right) \tag{4.7}$$

$$\frac{dv_B}{d\varepsilon} = \frac{2V_{\text{clad}}}{\lambda_p}\left(n_{a,j}\frac{dn_{o,i}}{d\varepsilon} + n_{o,i}\frac{dn_{a,j}}{d\varepsilon} + n_{a,j}\frac{dn_{o,j}}{d\varepsilon} + n_{o,j}\frac{dn_{a,j}}{d\varepsilon}\right) \tag{4.8}$$

4.3 Methods for multi-parameter discrimination

4.3.1 Discriminative measurement with two modes

To discriminate temperature and strain, at least two spatial modes (assigned as mode 1 and mode 2) are required. Assuming that the temperature and strain coefficients are expressed as $(c_{T,1}, c_{\varepsilon,1})$ and $(c_{T,2}, c_{\varepsilon,2})$, we can separating these two effects by measuring the BFS in each mode, which can be written as [98]:

$$\begin{bmatrix}\Delta v_{B,1}\\ \Delta v_{B,2}\end{bmatrix} = \mathbf{C}_2\begin{bmatrix}\Delta T\\ \Delta\varepsilon\end{bmatrix}, \qquad \mathbf{C}_2 = \begin{bmatrix}c_{T,1} & c_{\varepsilon,1}\\ c_{T,2} & c_{\varepsilon,2}\end{bmatrix}. \tag{4.9}$$

By solving the equation above, we can get the change of temperature ΔT and strain $\Delta\varepsilon$ as

$$\begin{bmatrix} \Delta T \\ \Delta\varepsilon \end{bmatrix} = \mathbf{C}_2^{-1} \begin{bmatrix} \Delta T \\ \Delta\varepsilon \end{bmatrix} = \frac{1}{\det(\mathbf{C}_2)} \begin{bmatrix} c_{\varepsilon,2} & -c_{\varepsilon,1} \\ -c_{T,2} & c_{T,1} \end{bmatrix} \begin{bmatrix} \Delta v_{B,1} \\ \Delta v_{B,2} \end{bmatrix}, \tag{4.10}$$

where $\det(\cdot)$ means matrix determinant.

To estimate the performance of multi-parameter discrimination, we assume the measurement error for these two modes are $\sigma_{v_B,1}$ and $\sigma_{v_B,2}$, respectively and assume they are uncorrelated. Here $\sigma_{v_B,i}$ is defined as the standard deviation of the BFS for mode i. Then the discriminative errors for temperature and strain are expressed as

$$\sigma_T = \sqrt{\frac{c_{\varepsilon,2}^2}{\det(\mathbf{C}_2)^2}\sigma_{v_B,1}^2 + \frac{c_{\varepsilon,1}^2}{\det(\mathbf{C}_2)^2}\sigma_{v_B,2}^2} \tag{4.11}$$

$$\sigma_\varepsilon = \sqrt{\frac{c_{T,2}^2}{\det(\mathbf{C}_2)^2}\sigma_{v_B,1}^2 + \frac{c_{T,1}^2}{\det(\mathbf{C}_2)^2}\sigma_{v_B,2}^2} \tag{4.12}$$

From these two equations it can be found that the accuracy of temperature and strain discrimination relies on the accuracy of mode 1 and mode 2. The errors also depend on the determinant of matrix $\mathbf{C}_2$, meaning that the matrix condition will also significantly affect the measurement resolution.

4.3.2 Generalised solution with more modes

Here, we would like to expand it to a more general case. If n modes are used, each of them has the temperature and strain coefficients written as (c_T, c_ε),$i \in \{1, 2, ..., n\}$, then we have:

$$\begin{bmatrix} \Delta v_{B,1} \\ \vdots \\ \Delta v_{B,n} \end{bmatrix} = \mathbf{C} \begin{bmatrix} \Delta T \\ \Delta\varepsilon \end{bmatrix}, \qquad \mathbf{C} = \begin{bmatrix} c_{T,1} & c_{\varepsilon,1} \\ \vdots & \vdots \\ c_{T,n} & c_{\varepsilon,n} \end{bmatrix} \tag{4.13}$$

If $\mathbf{C}$ has linearly independent columns, i.e. $\mathbf{C}^T\mathbf{C}$ is invertible, the solution for temperature and strain change can be expressed as:

$$\begin{bmatrix} \Delta T \\ \Delta \varepsilon \end{bmatrix} = \mathbf{C}^{+} \begin{bmatrix} \Delta v_{B,1} \\ \vdots \\ \Delta v_{B,n} \end{bmatrix} \tag{4.14}$$

where $\mathbf{C}^{+} = (\mathbf{C}^T\mathbf{C})^{-1}\mathbf{C}^T$ is the Moore-Penrose inverse of matrix $\mathbf{C}$.

Assuming that the uncertainty for Brillouin frequency shift of each mode can be written as $[\sigma_{v_B,1}, \sigma_{v_B,2}, \cdots, \sigma_{v_B,n}]$, then the errors of temperature and strain discrimination are evaluated through:

$$\sigma_T = \sqrt{\sum_{k=1}^{n} (c_{1k}^{+}\sigma_{v_B,k})^2}, \qquad \sigma_\varepsilon = \sqrt{\sum_{k=1}^{n} (c_{2k}^{+}\sigma_{v_B,k})^2} \tag{4.15}$$

where c_{ik}^{+} is the ith-row kth-column element of matrix $\mathbf{C}^{+}$. When two modes are used for the discrimination of temperature and strain, i.e. $n = 2$, Eqs. (4.13),(4.14) and (4.15) will reduce to the identical forms as in [134]. However, by using more modes, the sensing accuracy will be much improved.

4.4 System configuration

The experimental setup our proposed scheme is shown in Fig. 4.1. An external cavity laser (ECL) operating at 1.55 μm is split into two branches by a 50:50 optical coupler (OC). The lower branch is used as the local oscillator (LO), while the upper one is modulated by an acousto-optic modulator (AOM) driven by a pulse generator. The pulse width is 50 ns, corresponding to a spatial resolution of 5 m. A polarisation scrambler (PS) scrambles the polarisation of pump light. Then the pump pulses are sent to the free-space mode launcher (FSML) through an optical circulator (CIR). The Fig. 4.2 shows the structure of the FSML, which consists of three collimators (CLs) and one 50:50 beam splitter (BS), which forms two pathways for different spatial modes. A 0-π phase plate (PP) is used for the mode conversion between LP_{01}-mode and LP_{11}-mode, with an extinction ratio

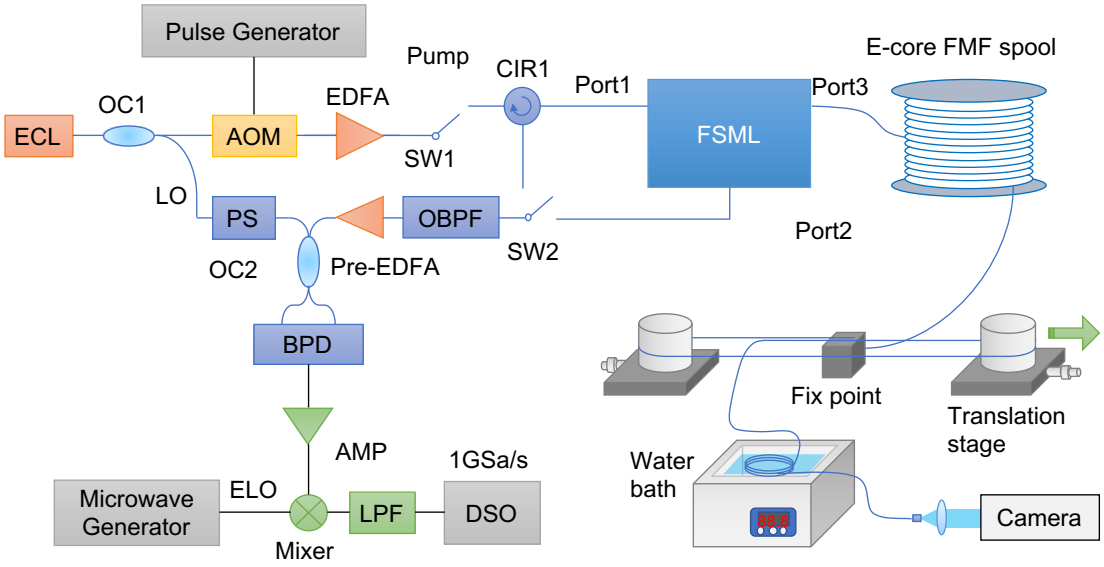

Figure 4.1: Experimental setup of the EC-FMF BOTDR.

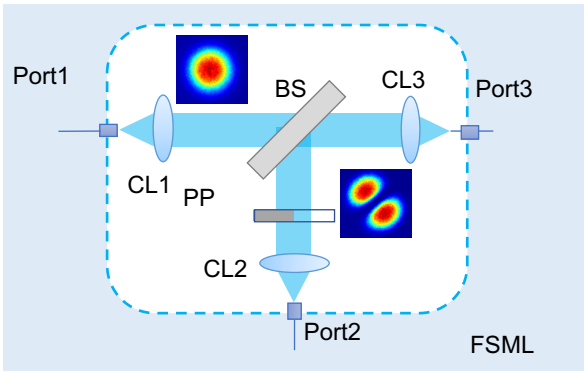

Figure 4.2: Inside structure of the free-space mode launcher (FMSL). CL: collimator, BS: beamsplitter, PP: phase plate.

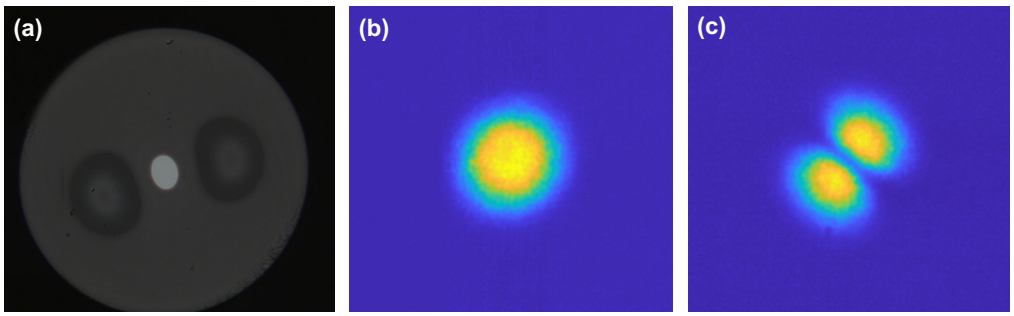

Figure 4.3: (a) Cross-section of the EC-FMF. (b) Measured mode pattern for LP_{01} mode. (c) Measured mode pattern for LP_{11} mode.

around 14 dB. The insertion loss of FSML is 4.5 dB for LP_{01} mode and 5.6 dB for LP_{11} mode, respectively.

The fibre under test here is a 500-m e-core few-mode fibre, supporting two LP modes (LP_{01}, LP_{11e}) at 1.55 μm and three LP modes (LP_{01}, LP_{11e}, LP_{11o}) at 1.3 μm. Fig. 4.3(a) shows the cross-section of the EC-FMF [54]. Fig. 4.3(b) and 4.3(c) are the measured mode patterns for LP_{01} and LP_{11e} modes, respectively. We have observed quite pure mode patterns for both LP_{01} and LP_{11}, indicating that the mode extinction ratio in FSML is sufficient. More detailed parameters of the EC-FMF can be found in [54]. At the far-end of the FUT, a 4-meter fibre segment is stretched by a translation stage, followed by a 20-meter segment which is placed in a temperature-controlled water bath. The backscattering light is filtered by an optical band-pass filter (OBPF) to eliminate the Rayleigh scattering, and is then amplified by a pre-EDFA with a narrow output filter inside. The beating signal between Brillouin scattering signal and LO is detected by a balanced photo-detector (BPD). A voltage-controlled oscillator (VCO) generates a RF sine wave to shift the beating signal to the frequency range within a 450-MHz low-pass filter (LPF). The signal is finally collected by a digital storage oscilloscope (DSO) with the sampling rate of 1GSa/s.

4.5 Characterisation of SpBS

We sent the pump in LP_{01} mode and received the Brillouin backscattering signals from both LP_{01} mode and LP_{11e} mode. The distributed Brillouin spectrograms were recovered by moving a 50-ns fast Fourier transform (FFT) window on the time-domain signal with 5-ns step interval. To make the spectra finer, the zero-padding technique was used. To improve the signal-to-noise ratio (SNR) as well as to eliminate the polarisation fading, the Brillouin spectrograms were averaged for 5000 times. Figs. 4.4 and 4.5 shows the measured Brillouin spectrograms as a function of frequency detuning and fibre distance, of LP_{01} output and LP_{11e} output respectively. Multi-peak shape is observed for both of them, indicating that there are higher order-acoustic modes. Fig. 5.6 shows the Brillouin spectra of the cross-sections of measured Brillouin spectrograms for a fibre segment under loose condition and room temperature.

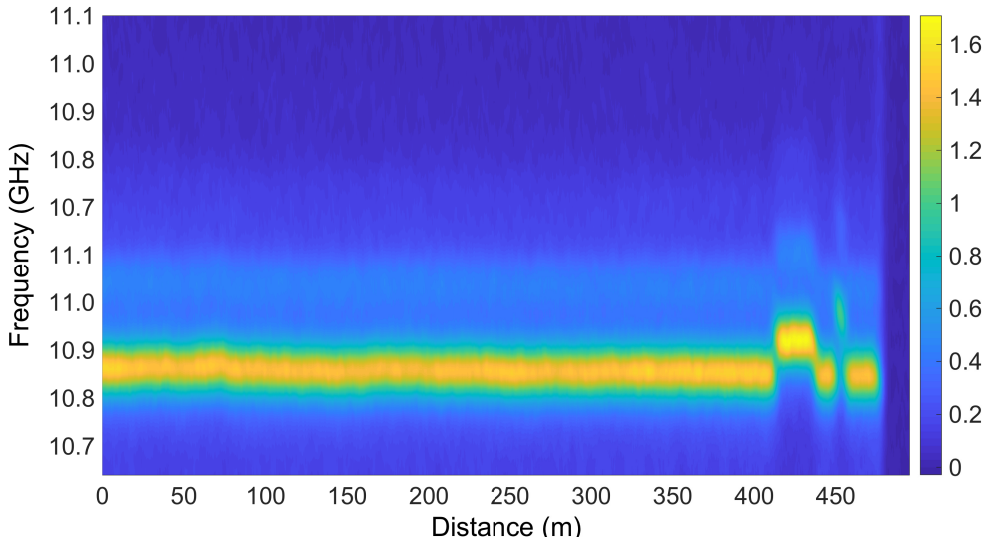

Figure 4.4: Measured Brillouin spectrograms of LP_{01} output as a function of frequency detuning and distance.

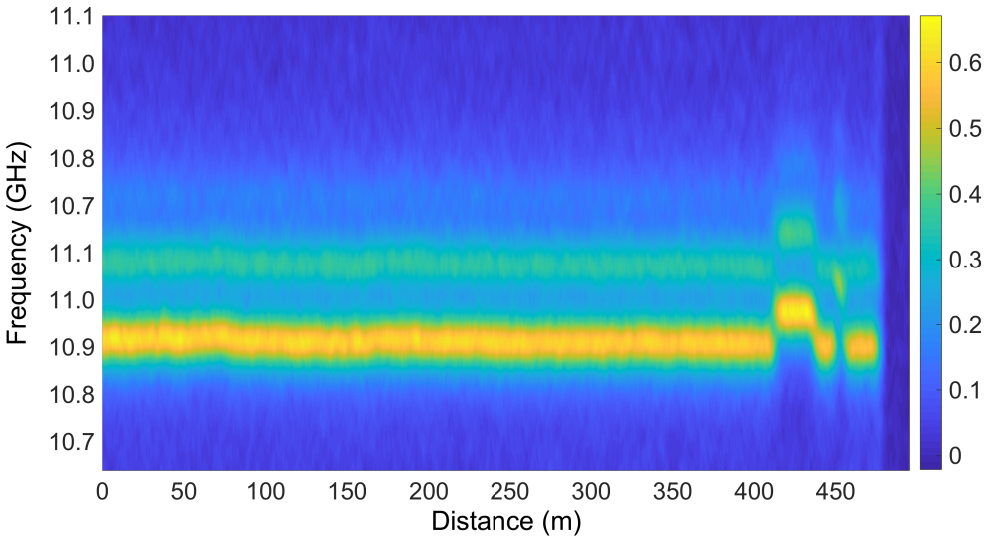

Figure 4.5: Measured Brillouin spectrograms of LP_{11} output as a function of frequency detuning and distance.

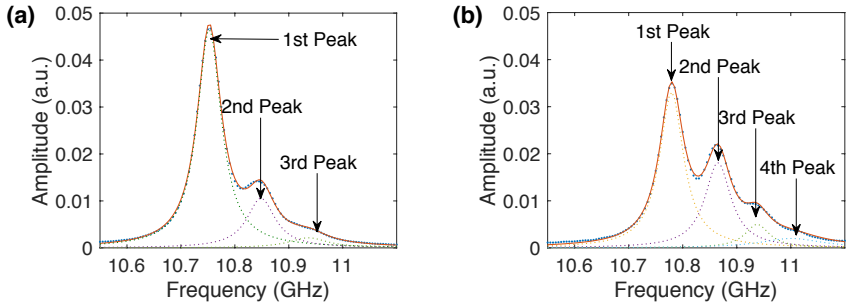

Figure 4.6: BGS of SpBS in EC-FMF: (a) LP_{01} to LP_{01}, (b) LP_{01} to LP_{11}. Dots: measured data points; solid red lines: multi-peak Lorentzian fit curves; dashed lines: standard Lorentzian fit curves.

We adopted the multi-peak Lorentzian fitting with the following model:

$$f_n(v) = \sum_{i=1}^{n} \frac{g_{0,i}\Gamma_{B,i}^2}{\Gamma_{B,i}^2 + 4(v - v_{B,i})^2} \tag{4.16}$$

where v is the frequency detuning. $g_{0,i}$, $\Gamma_{B,i}$, and $v_{B,i}$ correspond to the Brillouin amplitude, Brillouin linewidth and the BFS of ith peak, respectively. Fig. 4.6 shows the measured SpBS spectra (dots), the multi-peak fitting curves (solid lines) and the standard Lorentzian fit curves of each peak (dashed lines) for LP_{01} output and LP_{11e} output. Detailed characteristics of these SpBS, including g_0, v_B (in GHz unit) and Γ_B (in MHz unit), are shown in Table 4.1. From this table we can find that the 1st-peak v_B of the LP_{01} output is different from that of the LP_{11e} output by the amount of 26.9 MHz. Meanwhile, a difference of 18.8 MHz is observed between the 2nd-peak v_B of the LP_{11e} output and that of the LP_{01} output. These results indicate that the multi-peak Brillouin spectra are due to the interaction between the optical and acoustic modes, instead of the mode leakage.

4.6 Calibration of temperature and strain

We then conduct the calibration of temperature and strain coefficients by heating the water and moving the position of the translation stage. Fig. 4.7 gives the measured BFS as a function of temperature with various output modes, and Fig. 4.8 is the relationship

Table 4.1: Characteristics of the SpBS in EC-FMF

Mode		1st Peak	2nd Peak	3rd Peak	4th Peak
LP_{01}	g_0	1.4086	0.3216	0.0652	–
	v_B	10.7525	10.8464	10.9366	–
	Γ_B	54.051	63.614	87.592	–
LP_{11}	g_0	0.4961	0.2717	0.0746	0.0301
	v_B	10.7794	10.8652	10.9379	11.0012
	Γ_B	53.728	58.489	54.737	139.939

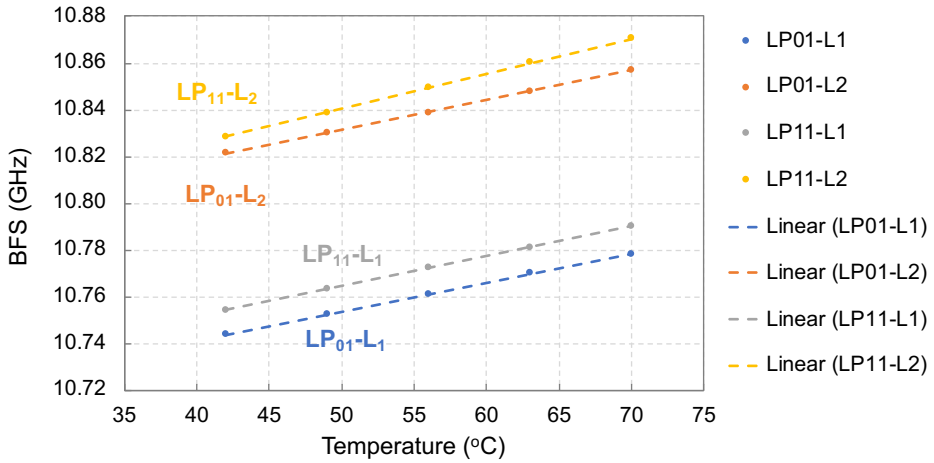

Figure 4.7: Measured BFS as a function of temperature for the 1st and 2nd peaks of LP_{01}-LP_{01} and LP_{01}-LP_{11e}, respectively.

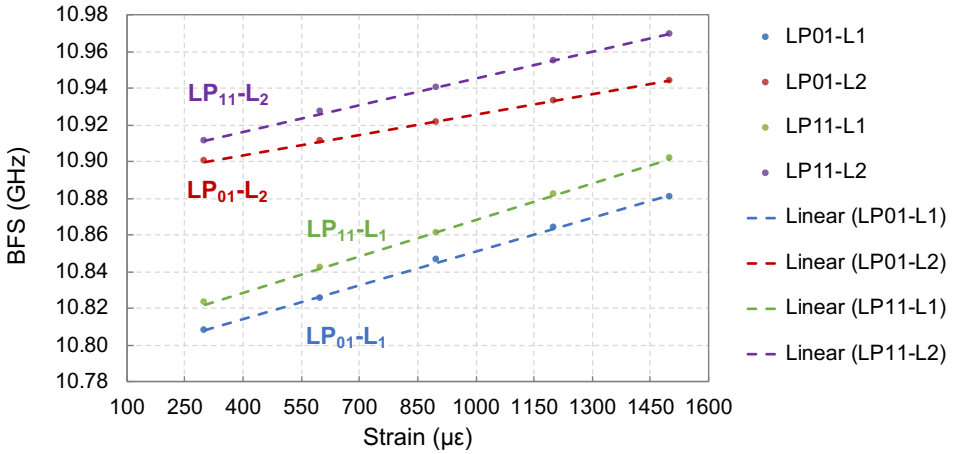

Figure 4.8: Measured BFS as a function of strain for the 1st and 2nd peaks of LP_{01}-LP_{01} and LP_{01}-LP_{11e}, respectively.

Table 4.2: Temperature and strain coefficients

Optical-acoustic mode pair	Temperature		Strain	
	Slope c_T (MHz/°C)	Intercept (GHz)	Slope c_ε (MHz/$\mu\varepsilon$)	Intercept (GHz)
LP_{01}-L_1	1.242	10.691	0.0613	10.790
LP_{01}-L_2	1.278	10.767	0.0364	10.889
LP_{11e}-L_1	1.287	10.700	0.0658	10.803
LP_{11e}-L_2	1.501	10.765	0.0484	10.896

between BFS and strain with various output modes. Linear regression (solid lines) was performed to calculate the temperature and strain coefficients. The fitting results, including the slopes (c_T, c_ε) and the intercepts, can be found in Table 4.2. Compared with the standard SMF which has coefficients around 1.08 MHz/°C and 43 kHz/$\mu\varepsilon$ [135], our EC-FMF has larger temperature and strain coefficients due to the core size and deformation.

4.7 Performance of discriminative sensing

Since the coefficients of various modes are different, they could be used for the temperature and strain discrimination. We assign the optical-acoustic mode pairs as M_1: LP_{01}-P_1, M_2: LP_{01}-P_2, M_3: LP_{11e}-P_1, and M_4: LP_{11e}-P_2, where LP_{lm} means the lm-order output optical modes and P_i indicates the ith-order acoustic peak. Then we can group them into 11 combinations, including 6 two-mode combinations, 4 three-mode combinations and 1 four-mode combination. To evaluate the performance of multi-parameter discrimination, we use the error amplification factors, which are defined as the ratios between the temperature/strain uncertainty and the BFS uncertainty, i.e. σ_T/σ_{v_B} and $\sigma_\varepsilon/\sigma_{v_B}$. Note that in Eq. (4.15) there are more than one mode used in the error estimation. Many literature assume that the BFS uncertainty or measurement error equals to 0.1 MHz for all the modes. However, in our system the BFSs of multiple Brillouin peaks are estimated through one Brillouin scattering spectrum, as shown in Fig. 4.6. According to [136,137], the BFS uncertainty σ_{v_B} can be expressed as:

$$\sigma_{v_B} \propto \frac{1}{SNR_a}\sqrt{\delta_v \Gamma_B} = \frac{\sigma_n}{g_0}\sqrt{\delta_v \Gamma_B} \tag{4.17}$$

where σ_n is the standard deviation of the noise, δ_v is the frequency interval of the Brillouin scattering spectrum, SNR_a is the amplitude signal-to-noise ratio. For all the modes, σ_n and δ_v are usually kept unchanged for a measurement. Therefore, the BFS uncertainty should take the Brillouin gain g_0 and the Brillouin linewidth Γ_B into account. Assuming that the BFS uncertainty for the 1st-order peaks of LP_{01} mode (i.e. σ_{v_B,M_1}) and LP_{11e} mode (i.e. σ_{v_B,M_3}) equals to σ_v, the BFS uncertainty for the 2nd-order peaks should be $\sigma_{v_B,M_2} = 4.7463 \cdot \sigma_v$ and $\sigma_{v_B,M_4} = 1.9051 \cdot \sigma_v$, calculated according to Eq. (4.17) with the data in Table 4.1.

Table 4.3: Error amplification factors with various combinations of optical-acoustic modes

Combination	$[M_1, M_2]$	$[M_1, M_3]$	$[M_1, M_4]$	$[M_2, M_3]$
σ_T/σ_v (°C/MHz)	8.8498	31.7716	3.9630	8.4418
$\sigma_\varepsilon/\sigma_v$ ($\mu\varepsilon$/MHz)	182.0517	631.8870	87.8433	167.5566
Combination	$[M_2, M_4]$	$[M_3, M_4]$	$[M_1, M_2, M_3]$	$[M_1, M_2, M_4]$
σ_T/σ_v (°C/MHz)	33.2409	3.6840	8.5644	5.5674
$\sigma_\varepsilon/\sigma_v$ ($\mu\varepsilon$/MHz)	1042.9360	78.8164	171.3150	124.1234
Combination	$[M_1, M_3, M_4]$	$[M_2, M_3, M_4]$	$[M_1, M_2, M_3, M_4]$	
σ_T/σ_v (°C/MHz)	3.6624	5.1435	5.0228	
$\sigma_\varepsilon/\sigma_v$ ($\mu\varepsilon$/MHz)	76.5745	110.3671	105.2716	

The error amplification factors σ_T/σ_v and $\sigma_\varepsilon/\sigma_v$ are then evaluated through Eqs. (4.13),(4.14) and (4.15) . Table 4.3 shows the results with various combinations of different optical-acoustic modes. Among the 2-mode combinations, using $[M_3, M_4]$, i.e. the 1st-order and the 2nd-order Brillouin peaks for LP_{11e} output, has the minimum error amplification factors of 3.6840 °C/MHz and 78.8164 $\mu\varepsilon$/MHz for temperature and strain, respectively. With the increasing number of modes in the combination, smaller error amplification factors can be achieved. When combination $[M_1, M_3, M_4]$ is used, we obtain the minimum factors, which are 3.6624 °C/MHz and 76.8163 $\mu\varepsilon$/MHz, respectively. Interestingly, when all the four modes $[M_1, M_2, M_3, M_4]$ are used, the error amplification factors become larger than some two-mode or three-mode combinations. This is due to the fact that the large BFS uncertainty σ_{v_B,M_2} for M_2 peak contributes a lot in both temperature and strain errors. Therefore, involving M_2 in the error analysis will deteriorate

the performance. It is worth noticing that the three-mode combination $[M_1, M_3, M_4]$ only surpass the two-mode combination $[M_3, M_4]$ by less than 3%. Considering the additional steps for detecting the output of both LP_{01} mode and LP_{11e} mode, this small improvement could be neglected in most practical applications. Therefore, the optimal solution will be injecting the light into LP_{01} mode and detecting the Brillouin backscattering from LP_{11e} mode. In practical situation, this can be realised by using a simple FSML, and there is no need for mode switching. For a fair comparison with other FMF-based multi-parameter sensors, we also assume $\sigma_v = 0.1$ MHz as in [98]. In this case, the accuracy of discrimination between temperature and strain is 0.37 °C and 7.88 $\mu\varepsilon$. Compared with the previous results with FMFs, our scheme has better discriminative performance. This result indicates that the using the higher-order optical and acoustic modes in the elliptical-core few-mode fibre could be a promising solution for multi-parameter sensing.

It is noted that the Moore-Penrose inverse method used in this chapter is a simple approach, but might not be the optimal solution when the noise of each mode is different. Therefore, it is also a part of the reasons that the performance is degraded when all the modes are used. An alternative will be a solution that taking the error (noise) per mode into account, such as the minimum mean-square error (MMSE) estimator. We are currently working on this topic and will present the results in the future.

4.8 Chapter conclusion

In this chapter, we have proposed and experimentally demonstrated a single-ended Brillouin optical time-domain reflectometry in EC-FMF. Both the inter-modal and intra-modal SpBSs were observed and characterise. Distributed multi-parameter sensing of temperature and strain was demonstrated over 0.5 km EC-FMF with 5-m spatial resolution. Our results show that the EC-FMF can be good candidate for multi-parameter distributed fibre sensing. Part of this work has been presented at the 26th International Conference of Optical Fibre Sensors (OFS) [138].

Chapter 5

Ultra-fast Brillouin fibre sensing technique

5.1 Motivation

Conventional BOTDA requires taking a large number of measurements for distributed fibre sensing each time, including scrambling the pump polarisation, averaging the received traces and scanning the probe frequency. Therefore the sensing process is usually time-consuming, ranging from tens of seconds to tens of minutes. Furthermore, it assumes that the fibre status (strain and temperature) shall remain unchanged during these measurements; otherwise, the distributed Brillouin spectra may not be correctly reconstructed. Thus it is applicable for monitoring some relatively slow changes along the fibre. In the past few years, distributed dynamic sensing which records fast strain/temperature variation along the fibre, has become a hot topic driven by the growing demand in gas and oil industries, geophysical science and structural health monitoring. Therefore it is desirable for BOTDA technique with boosted sensing speed. To reduce the measuring time, several methods have been proposed, including the slope-assisted method [112, 113], the fast frequency-swept method [114], the RF phase demodulation method [139] and the digital optical frequency comb method [116]. All of these methods have shown some encouraging improvements and applications. Nevertheless, either frequency scanning, or polarisation scrambling, or averaging is still required, which will limit the ultimate measuring speed.

In this chapter, we will propose and demonstrate a novel ultra-fast Brillouin fibre sensing technique named single-shot Brillouin optical time-domain analyser (single-shot

BOTDA). Here, 'single-shot' means that all the information of the fibre is gathered by sending only one pump pulse and receiving the corresponding probe light. Therefore, the sensing speed is expected to be drastically improved. Compared with other DSP-based multi-tone method, our OFDM method in BOTDA has several advantages: (1) no spectral leakage when performing piecewise FFT analysis, (2) low PAPR by properly design the symbol, (3) no need for Guard Interval (GI) since the same OFDM symbol is repeatedly sent as the probe. The details of our proposed scheme will be described in the following sections.

5.2 Principle of single-shot BOTDA

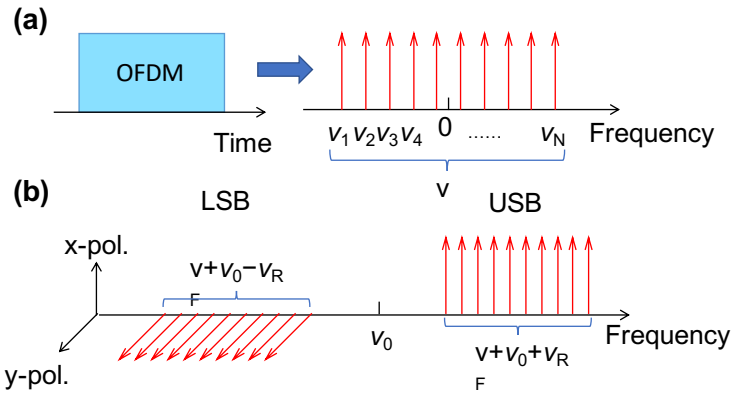

Figure 5.1: The principle of single-shot BOTDA.

The principle of our proposed single-shot BOTDA method is shown in Fig. 5.1, instead of the CW probe used in conventional BOTDA, we use the orthogonal side-band probe with orthogonal frequency division multiplexing (OFDM) modulation in our scheme. A baseband OFDM symbol $s(t)$ can be expressed as [140]

$$s(t) = \sum_{i=-\infty}^{+\infty} \sum_{k=1}^{N} c_{ki} s_k(t - iT_s) \tag{5.1}$$

$$s_k(t) = \Pi(t) e^{j2\pi v_k t}, \tag{5.2}$$

$$\Pi(t) = \begin{cases} 1, (0 < t \leq T_s) \\ 0, (t \leq 0, t > T_s) \end{cases} \tag{5.3}$$

where c_{ki} is the ith complex information at the kth subcarrier, s_k is the waveform for the kth subcarrier and v_k is the frequency [141]. N is the number of subcarriers, $\Pi(t)$ is the pulse shaping function and T_s is the symbol period. If an identical complex sequence $\mathbf{c} = [c_1, c_2, \ldots, c_N]^T$ is repeatedly sent as the information symbol, then in time domain the baseband signal becomes

$$s(t) = \sum_{k=1}^{N} c_k e^{j2\pi v_k t} \tag{5.4}$$

The frequency of subcarriers can be expressed as a vector $\mathbf{v} = [v_1, v_2, \ldots, v_N]^T, k = 1, 2, \ldots, N$, as shown in Fig. 5.1(a). After modulating on an optical carrier with amplitude A_0 and frequency v_0, the time-domain electric field $E_t(t)$ of transmitted optical OFDM is written as

$$E_t(t) = A_0 \sum_{k=1}^{N} c_k e^{j2\pi(v_k+v_0)t} \tag{5.5}$$

Taking the Fourier transform of the above equation, we get

$$\hat{E}_t(v) = A_0 \sum_{k=1}^{N} c_k \delta[2\pi(v - v_k - v_0)] \tag{5.6}$$

In order to cancel the polarisation fading, the optical OFDM signal E_t is then double sideband (DSB) modulated by a RF sine wave with frequency v_{RF} in an intensity modulator working at its null point. Then the output electric field turns to

$$\hat{E}_{\mathrm{DSB}} = \underbrace{a_0 A_0 \sum_{k=1}^{N} c_k \delta[2\pi(v - v_k - v_0 + v_{\mathrm{RF}})]}_{\hat{E}_{s+}} + \underbrace{a_0 A_0 \sum_{k=1}^{N} c_k \delta[2\pi(v - v_k - v_0 - v_{\mathrm{RF}})]}_{\hat{E}_{s-}} \tag{5.7}$$

where a_0 is a factor which contains the amplitude scaling and the common phase change. The polarizations of the upper sideband (USB) and lower sideband (LSB) are then ro-

tated to be orthogonal to each other. Finally the orthogonal sideband probe can be represented as a Jones vector $\mathbf{E}_s = E_{s+}\mathbf{e}_x + E_{s-}\mathbf{e}_y$, where $\mathbf{e}_x$ and $\mathbf{e}_y$ are the basis vectors for x-polarisation and y-polarisation, respectively, as depicted in Fig. 5.1(b).

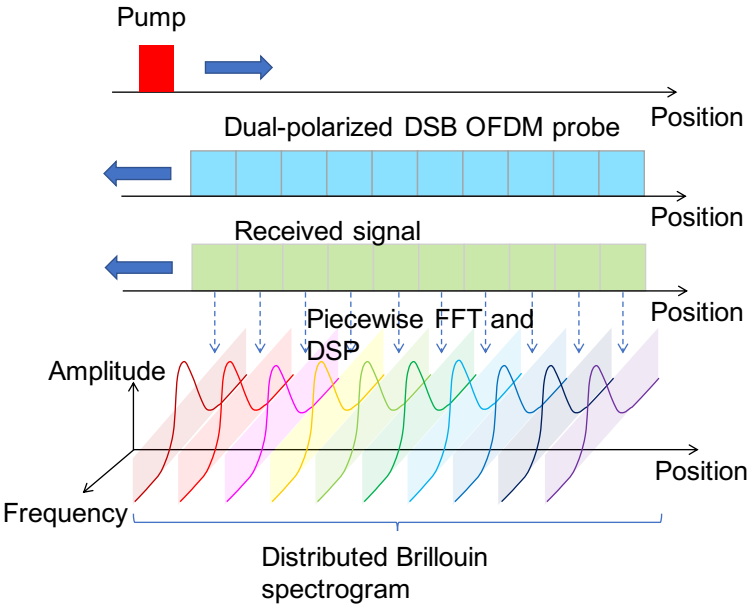

Figure 5.2: Principle of single-shot BOTDA

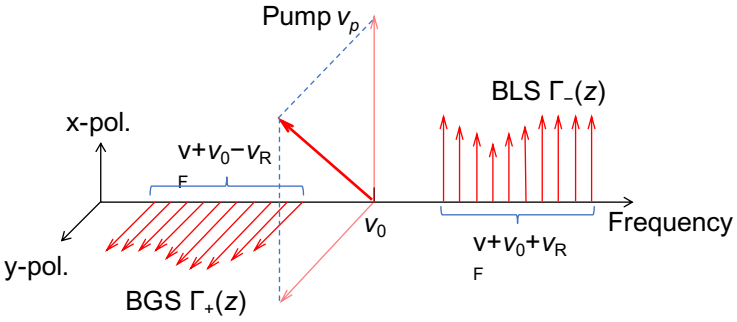

Figure 5.3: Orthogonal double-sideband of OFDM probes.

As shown in Fig. 5.2, the probe and pump counter-propagate along the fibre. When they meet each other at the position z, stimulated Brillouin scattering (SBS) process happens. If the RF frequency v_{RF} is near the Brillouin frequency shift (BFS) v_B, the lower sideband will be amplified while the upper sideband will be attenuated, which is shown

in Fig. 5.3 and can be expressed:

$$E_{r+} = h_+(t,z) \otimes E_{s+}, \quad E_{r-} = h_-(t,z) \otimes E_{s-} \tag{5.8}$$

where '$\otimes$' is the convolution operator, $h_+(t,z)$ and $h_-(t,z)$ are the impulse responses of the Brillouin gain and loss at position z, respectively. In frequency domain Eq. (5.8) becomes

$$\hat{E}_{r+} = H_+(v,z)\hat{E}_{s+}, \quad \hat{E}_{r-} = H_-(v,z)\hat{E}_{s-} \tag{5.9}$$

where $H_+(v,z)$ and $H_-(v,z)$ are the complex Brillouin gain and Brillouin loss spectra at position z, respectively. Assuming that the pump width is longer than the lifetime of acoustic phonon, then these spectra can be given by [142]

$$H_\pm(v,z) = \exp\left[\pm\frac{\eta_\pm g_0 \Gamma_B}{\Gamma_B + 2j(v - v_p \pm v_B(z))}\right] \tag{5.10}$$

where g_0 is the local Brillouin gain, Γ_B is the Brillouin linewidth, v_p is the frequency of pump light. η_+ and η_- are the real mixing efficiency factors of the LSB probe and the USB probe. According to [143], the mixing efficiency factors are written as

$$\eta_\pm = \frac{1}{2}(1 + s_{1p}s_{1s\pm} + s_{2p}s_{2s\pm} - s_{3p}s_{3s\pm}) \tag{5.11}$$

where $\mathbf{s}_p = [s_{1p}, s_{2p}, s_{3p}]^T$, $\mathbf{s}_{s+} = [s_{1s+}, s_{2s+}, s_{3s+}]^T$, $\mathbf{s}_{s-} = [s_{1s-}, s_{2s-}, s_{3s-}]^T$ are the normalised Stokes vectors of the pump, the LSB probe and the USB probe, respectively. Since the LSB probe and the USB probe are orthogonal in polarisation, i.e. $\mathbf{s}_{s+} + \mathbf{s}_{s-} = 0$, one has $\eta_+ + \eta_- = 1$.

The probe light is then received by a polarisation diversity coherent receiver, which mixes probe with a local oscillator (LO) light $E_{\mathrm{LO}} = E_0 \exp(j2\pi v_{\mathrm{LO}} t)$ in a 90 degree optical hybrid. The received complex signals are written as

$$R_+ = \frac{1}{\sqrt{2}}\gamma E_{r+}E^*_{\mathrm{LO}}, \quad R_- = \frac{1}{\sqrt{2}}\gamma E_{r-}E^*_{\mathrm{LO}} \tag{5.12}$$

where γ is the detector responsivity. If LO, probe carrier and pump has the same fre-

quency, i.e. ($v_{\mathrm{LO}} = v_0 = v_p$), the received frequency will be down-converted. Then the received time-domain signals R_+ and R_- are divided into many segments, each of which has the identical length to OFDM symbol period T_s. The subcarrier amplitude of each segment can be obtained through Fourier transform, as shown in Fig. 5.2. Here we assign the subcarrier frequencies of LSB and USB as vectors $\mathbf{v}_+ = [v_{k+}]_{N\times 1}$ and $\mathbf{v}_- = [v_{k-}]_{N\times 1}$, respectively, where $v_{k+} = v_k - v_{RF}$ and $v_{k-} = v_k + v_{RF}$, v_k is the k-th element of $\mathbf{v}$. Since the transmitted symbol $\mathbf{c}$ is known, we can easily derive the Brillouin gain spectrum (BGS) and Brillouin loss spectrum (BLS), which can be described by the logarithmic gain vector $\mathbf{\Gamma}_+(z) = [\Gamma_{k+}]_{N\times 1}, \Gamma_{k+} = \Gamma_+(v_{k+}, z)$ and loss vector $\mathbf{\Gamma}_-(z) = [\Gamma_{k-}]_{N\times 1}, \Gamma_{k-} = \Gamma_-(v_{k-}, z)$ where

$$\Gamma_\pm(v, z) = \pm \frac{2\eta_\pm g_0 \Gamma_B^2}{\Gamma_B^2 + 4(v \pm v_B(z))^2} \tag{5.13}$$

The next step is to combine BGS and BLS and eliminate the polarisation effect. Here we flip the vector $\mathbf{\Gamma}_-(z)$ as $\overline{\mathbf{\Gamma}}_-(z)$ and define $\Delta\mathbf{\Gamma}(z) = \mathbf{\Gamma}_-(z) - \overline{\mathbf{\Gamma}}_-(z)$. If the subcarrier frequency of the baseband OFDM satisfies $v_k = -v_{N+1-k}, k = 1, 2, \ldots, N$, then $\Delta\mathbf{\Gamma}(z) = G(\mathbf{v}, z)$, where $G(v, z)$ is the Lorentzian shape Brillouin gain profile that

$$G(v, z) = \frac{2g_0 \Gamma_B^2}{\Gamma_B^2 + 4(v - v_{\mathrm{RF}} + v_B(z))^2} \tag{5.14}$$

According to the Eq. (5.14) the gain profile is independent of polarisation, indicating that the polarisation fading has been eliminated. After calculating the Brillouin spectrum vector $\Delta\mathbf{\Gamma}$of the entire segments, we can combine them as the distributed Brillouin spectrogram. Therefore the BFS v_B can be estimated by curve fitting with the vector $\mathbf{v}$ and $\Delta\mathbf{\Gamma}$.

It is worth noting that the polarisation-diversity coherent detection in our scheme can not only acquire the complete electric field of the probe light, but can increase the signal-to-noise ratio (SNR) and sensitivity as well. Compared with the direct detection in conventional BOTDA which can only detect the probe intensity, the LO in coherent detection can amplify the probe by a factor of $|E_{\mathrm{LO}}|/|E_s|$, which can significantly enhance the SNR and make it easier to detect the weak probe light. Thus the desired SNR can be

achieved by coherent detection. This SNR enhancement is realised by mitigating the impact of receiver-side noise. However, it may not has as much improvement as the averaging on some in-band noise in the channel, such as the in-band component of ASE noise.

5.3 Experimental setup

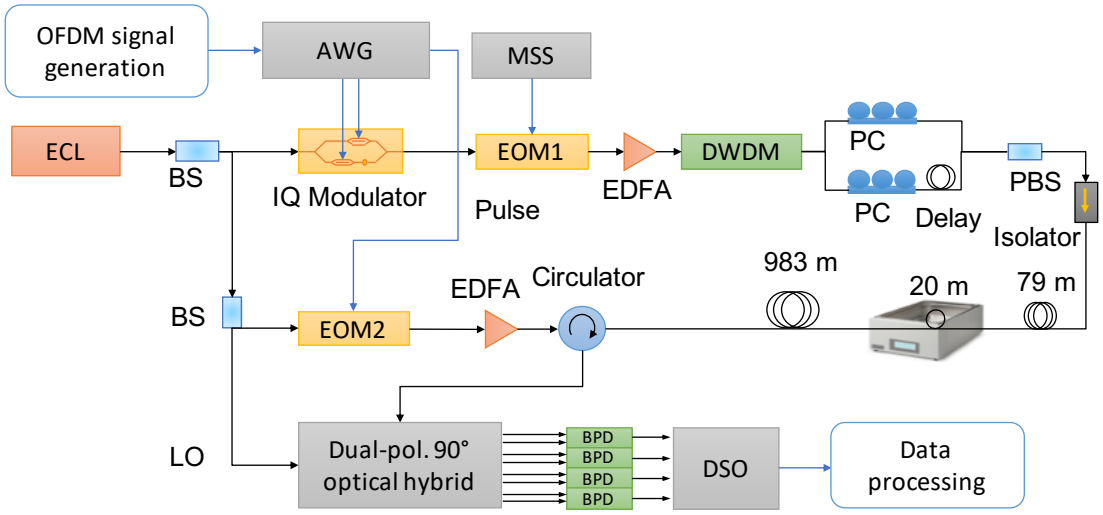

Figure 5.4: The experimental setup

The experimental setup is depicted in Fig. 5.4. An external cavity laser (ECL) with 1542.72 nm centre wavelength and 100 kHz linewidth is split into three branches as the probe, the pump, and the local oscillator by two 3dB beam splitters (BS). The probe part is first modulated by an OFDM signal in an optical in-phase quadrature (IQ) modulator driven by an arbitrary waveform generator (AWG) operating at of 10 GSa/s. The OFDM frame is initially designed in frequency domain with $N = 256$ subcarriers and 2048 total sample points, corresponding to a symbol period of 204.8 ns [1] and a spatial resolution of 20.48 m. In order to reduce the peak-to-average power ratio (PAPR), the subcarriers are

[1] We choose 204.8 ns as the symbol duration because we use 2048-point FFT in OFDM signal generation with an AWG sampling rate of 10 GSa/s.

mapped by a Zadoff-Chu sequence $\mathbf{c} = [c_k]_{N\times 1}$ given by

$$c_k = \exp\left(-j\pi(k-1)^2/N\right), k = 1, 2, \ldots, N \tag{5.15}$$

Due to the large symbol period, intra-symbol phase noise between LO and probe may occur. Thus we add a pilot tone at the right side of $\mathbf{c}$ to track the phase as depicted in Fig. 5.5(a), and to compensate the phase noise in the following section. Then the frequency domain signal is transformed to time domain OFDM frame by a 2048 points inverse fast Fourier transform (Inverse FFT). The real and imaginary parts of an OFDM frame in time domain are shown in Fig. 5.5(b). According to the PAPR definition that

$$\text{PAPR} = \max\left[|s(t)|^2\right] / E\left[|s(t)|^2\right] \tag{5.16}$$

, the PAPR of our designed OFDM signal is only 3.04 dB (within the time interval of one symbol period), which is almost identical to the PAPR of an ideal sinusoidal waveform (3dB), indicating that our OFDM signal power is nearly uniformly distributed in both time domain and frequency domain.

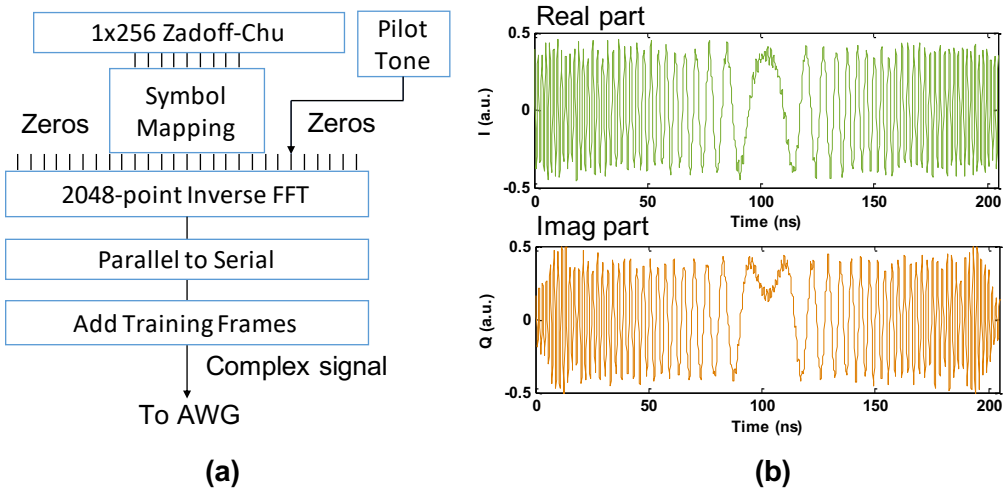

Figure 5.5: (a) Generation of the complex baseband OFDM signal. (b) The real part (I) and imaginary part (Q) of one generated OFDM frame in time domain. (c) The electric spectrum of the baseband OFDM probe.(d) The optical spectrum of the double-sideband OFDM probe with orthogonal sideband polarizations.

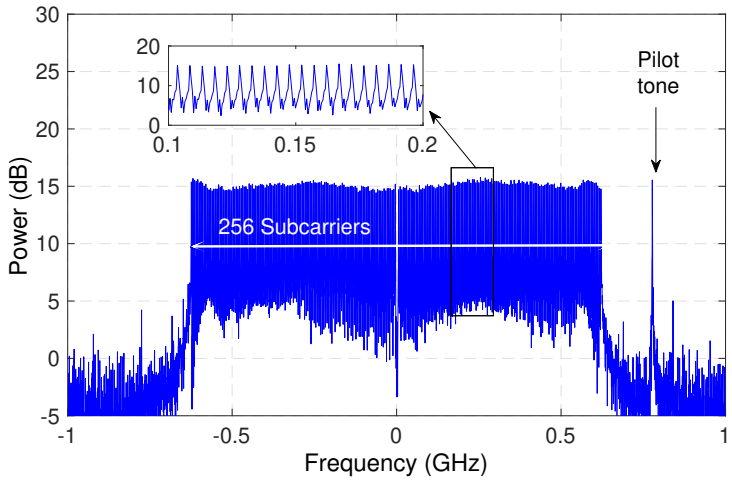

Figure 5.6: The electrical spectrum of the baseband OFDM probe.

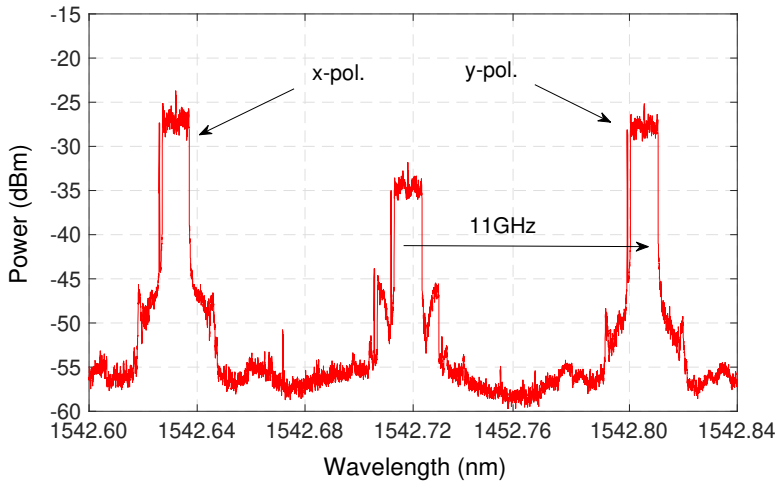

Figure 5.7: The optical spectrum of the double-sideband OFDM probe with orthogonal sideband polarizations.

Then the OFDM frame is repeatedly modulated on the probe as the OFDM signal $E_t(t)$. The electrical spectrum of the OFDM signal is depicted in Fig. 5.6. The 256 sub-carriers occupy a bandwidth from -625 MHz to +625MHz with 4.88 MHz frequency spacing and almost identical amplitude. The small fluctuation of the flat top in Fig. 5.6 is due to the electric distortion of cables and digital-to-analogue converters (DACs). Then a $v_{\mathrm{RF}} = 11$ GHz radio frequency (RF) sine wave modulates the OFDM baseband probe in an electro-optic modulator (EOM). The upper sideband and lower sideband are then separated by a 50 GHz dense wavelength division multiplexer (DWDM) with a sharp slope (30 dB over 10 GHz) . The polarizations of USB and LSB are then adjusted to be orthogonal via two polarisation controllers (PCs) and are combined in a polarisation beam splitter (PBS). Fig. 5.7 depicts the optical spectrum of DSB probe with orthogonal polarisation sidebands. The USB and LSB are assigned as x-polarisation and y- polarisation, respectively. The dual-polarised DSB probe is sent into the fibre through an optical isolator. The total transmitted probe power is -16 dBm.

The pump pulse is generated in another EOM driven by a pulse signal with 150 ns pulse width and 50 kHz repetition rate. Then the pump pulses are amplified by an EDFA to 8 dBm and sent into the fibre under test (FUT) via an optical circulator. The FUT is composed of a 983.14 m standard single-mode fibre (SSMF) spool and a 98.85 m SSMF segment, which the first 20 m is heated by a water bath. The total length is around 1.08 km and the round-trip time is about 10.8 μs. FC/APC connectors are used to reduce the Fresnel reflection.

After the SBS process, the probe signal is mixed with a 6 dBm CW LO in a polarisation diversity coherent detector, which consists of a 90-degree dual-polarisation optical hybrid (Kylia) and four balanced photo-detectors (BPDs). The outputs of four BPDs are acquired by a digital storage oscilloscope (DSO) operating at 50 GSa/s. The received data are then treated in the following signal processing part.

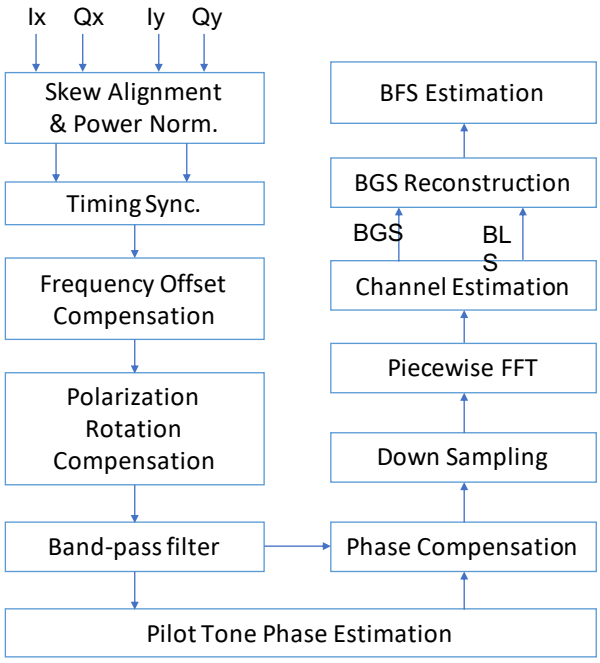

Figure 5.8: Procedure of data processing.

5.4 Data processing

The procedure of data processing is illustrated in Fig. 5.8. The received outputs from four detectors are I_x, Q_x, I_y, and Q_y. After the skew alignment and power normalisation, they form the complex received signals as $R_x = I_x + jQ_x$ and $R_y = I_y + jQ_y$, which correspond to the x- and y-polarisation, respectively. After the timing synchronisation, frequency offset compensation and polarisation rotation compensation using the training frames, a bandpass filter is utilised to filter out the pilot tone and estimate its relative phase drift to the LO. Since the pilot tone and the OFDM signal are generated simultaneously and propagate along the same fibre, their phases are inherently locked. Therefore the phase drift of OFDM signal can be compensated by multiplying the conjugate of the pilot phase and relative frequency offset. The time-domain data are then down-sampled by 5 and divided into segments, each of which has 2048 sample points, corresponding to 20.48 m fibre length. Fast Fourier transform (FFT) is conducted on each segment to get the spectra of both polarizations. The first several segments which are not affected by SBS process are used to estimate the frequency-domain channel distortion. The channel distortion of

other segments in SBS region can be compensated by inverting this distortion shape.

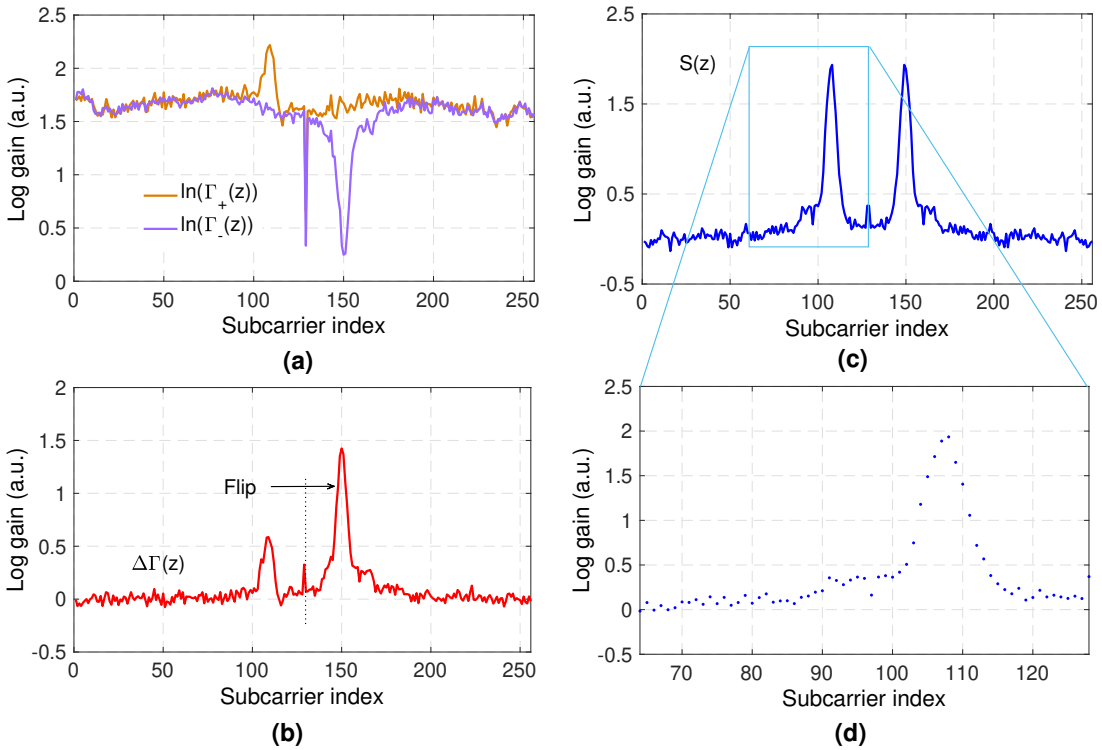

Figure 5.9: (a) Logarithmic gain of BGS vector $\mathbf{\Gamma}_+(z)$ and vector BLS $\mathbf{\Gamma}_-(z)$ of a OFDM frame in the SBS region. (b) Differential Logarithmic gain between the BGS and BLS vectors. (c) Flipped the combined logarithmic gain profile $\Delta\mathbf{\Gamma}(z)$ (d) shows the data points which used for curve fitting and BFS estimation.

Fig. 5.9(a) depicts the logarithmic subcarrier amplitudes of both x- and y- polarizations of one OFDM frame, corresponding to the BGS vector $\mathbf{\Gamma}_+(z)$ and BLS vector $\mathbf{\Gamma}_-(z)$, respectively. We can find that they have the similar channel distortion shape. Some subcarrier amplitudes of y-polarisation are amplified while some subcarrier amplitudes of x-polarisation are attenuated. When we subtract $\mathbf{\Gamma}_-(z)$ from $\mathbf{\Gamma}_+(z)$, as shown in Fig. 5.9(b), the channel distortion is almost eliminated. Then we flip the spectrum and add it with the original one, resulting in a logarithmic gain profile vector $\Delta\mathbf{\Gamma}$, as shown in Fig. 5.9(c). Fig. 5.9(d) illustrates part of the data points with a good Lorentzian shape, which can be use for BFS estimation.

We then calculate the BLS and BGS vectors for each segment and draw them as the reconstructed Brillouin spectrogram for x-polarisation, y-polarisation and the combined

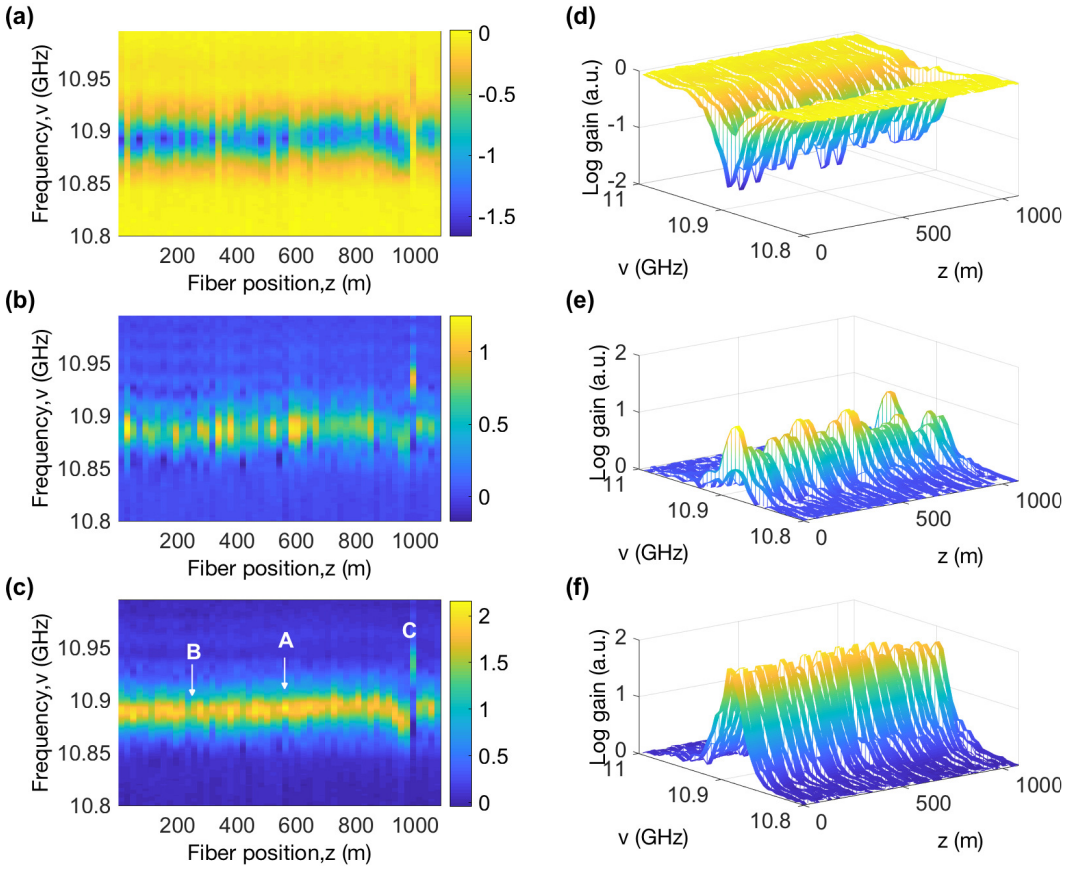

Figure 5.10: Reconstructed Brillouin spectrogram for (a) x-polarisation (b) y-polarisation and (c) combined dual-polarisation. (d), (e) and (f) are the three-dimensional view of (a), (b) and (c), respectively.

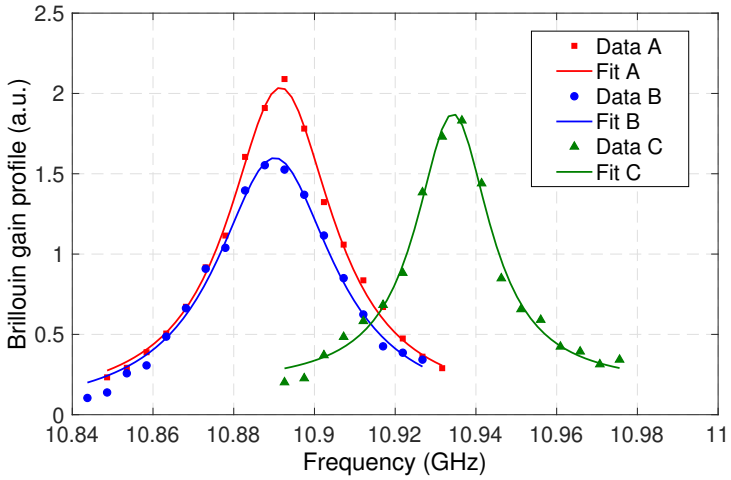

Figure 5.11: The measured BGS and Lorenztian fit curves for three selected positions. A: maximal gain; B: minimal gain; C: maximal frequency shift.

dual-polarisation in Fig. 5.10(a) (b) and (c), respectively. Fig. 5.10(d), (e) and (f) are the three-dimensional view of (a) (b) and (c), respectively. Due to the polarisation effect, there are drastic amplitude fluctuations in Fig. 5.10(a) and (b). However, the Brillouin peaks in Fig. 5.10(c) are quite stable, meaning that the polarisation fading has been successfully mitigated. We also notice that there is a small fluctuation of Brillouin peaks in the combined spectrogram due to measurement noise. To prove that this undulation is insignificant, we choose the maximal peak position, the minimal peak position and the maximal BFS shift position marked as A, B and C in Fig. 5.10. The original data points and the Lorentzian fitting curves of these three positions are shown in Fig. 5.11. It can be found that all the data points for A, B and C are adequate for the curve fitting, meaning that all the data in the reconstructed spectrogram are sufficient for BFS identifying.

5.5 Results

In order to test our single-shot BOTDA performance, distributed temperature sensing experiment is carried out by increasing the temperature of water bath from room temperature to over 75 °C and taking several single-shot BOTDA measurements. Then we treat the recorded data by the signal processing method described in section 4 and com-

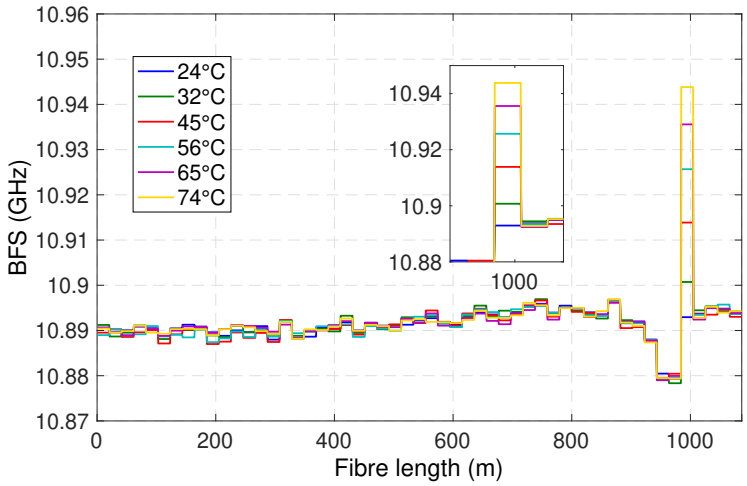

Figure 5.12: The estimated BFS along the fibre with different water bath temperature. The inset figure shows the increment of BFS of the heated fibre segment.

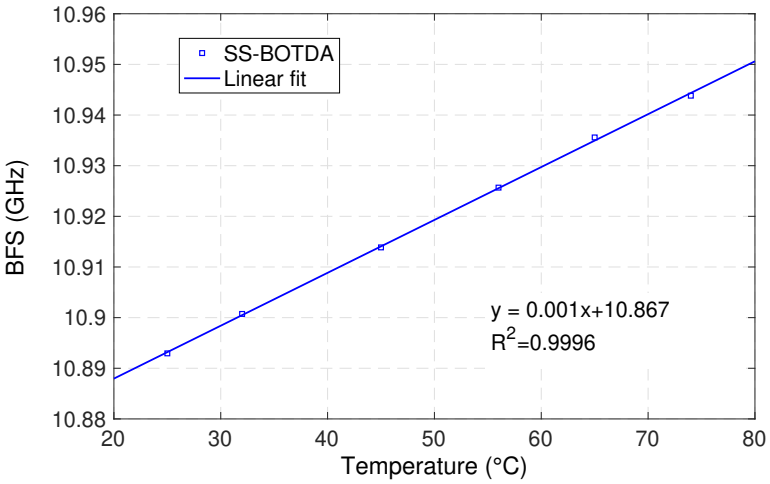

Figure 5.13: BFS of the hotspot as a function of temperature. Blue line is the linear curve fitting.

pute the distributed BFS. Fig. 5.12 shows the calculated BFS for the 1.08 km FUT. The slight variation around the far end of 983 m fibre spool is because of the strain change from manual spooling [115]. The inset in Fig. 5.12 depicts the variation of BFS in the hotspot. With temperature goes higher, the BFS shifts upwards. We then record the BFS of the hotspot position and evaluate its relationship with the temperature via linear fitting, as shown in Fig. 5.13. The temperature coefficient for the FUT is 1.03 MHz/°C. The coefficient of determination R^2 [2] is 99.96%, indicating that good linear relationship is achieved for temperature sensing.

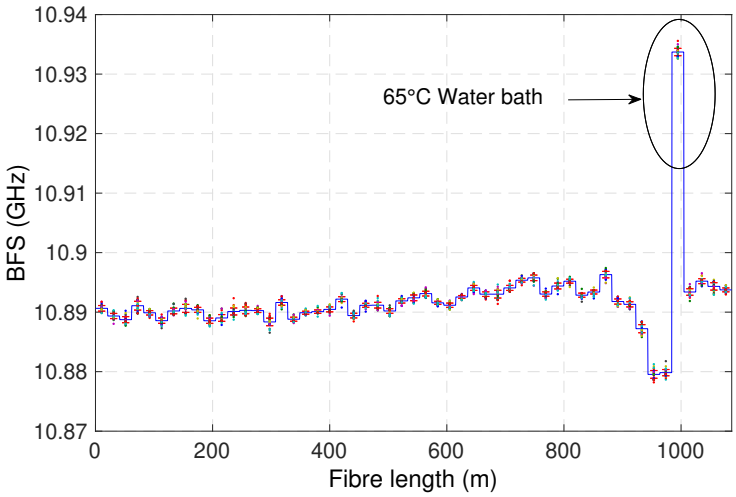

Figure 5.14: BFS of 25 times of measurements along the fibre when the water bath is set to 65°C. Blue line is the mean value for each segment. Dots are BFS data points. Red lines are the error bars.

To validate that our single-shot BOTDA is replicable and reliable, the single-shot measurement is consecutively performed 25 times when the temperature of hotspot is set to 65 °C. Fig. 5.14 shows the BFS of each measurement. The blue line denotes the mean BFS values and the dots are the BFS data for each segment. We can find that the BFS data points are well superposed, indicating that the results are almost the same. To demarcate the accuracy of temperature sensing, we calculate the BFS deviation to the mean value of each segment. According to the histogram in Fig. 5.15, the probability density of

[2] In this thesis, R^2 is defined as the ratio of the sum of squares of the regression (SSR) and the total sum of squares (SST). Assuming that the measured data $\mathbf{y} = [y_1, y_2, \dots y_n]^T$ and the fit data is $\bar{\mathbf{y}} = [\hat{y}_1, \hat{y}_2, \dots \hat{y}_n]^T$, SSR is defined as $\sum_{i=1}^{n}(\hat{y}_i - \bar{y})^2$ and SST is defined as $\sum_{i=1}^{n}(y_i - \bar{y})^2$, where $\hat{y}$ is the mean value of $\mathbf{y}$.

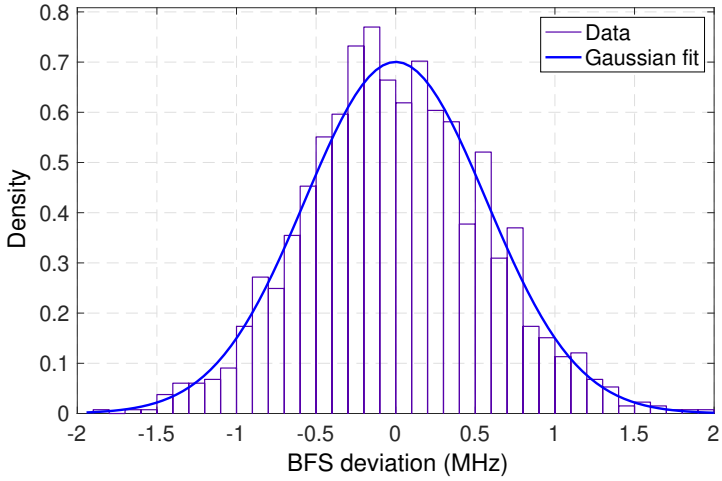

Figure 5.15: Probability density distribution of BFS deviation. Blue line denotes the Gaussian curve fitting of the probability density function (PDF).

BFS deviation approximates a Gaussian distribution. We then perform Gaussian fitting $\mathcal{N}(\mu, \sigma^2)$ on the measured BFS and obtain the results as $\mu = 0$ MHz and $\sigma = 0.57$ MHz. Since the temperature coefficient is 1.03 MHz/°C, the accuracy of temperature sensing is only 0.59 °C, indicating that our measurement result is accurate and reliable.

5.6 Discussion

In our configuration, the pump pulse repetition rate is set to 50 kHz. However, since all the data are acquired with one-time measurement, the ultimate sensing speed is only limited by the fibre round-trip time. Moreover, since the spectrum of OFDM probe can cover several GHz, the sensing speed can be further increased by sequentially launching the pump pulses with different frequencies, as used in [115]. Furthermore, since the subcarriers within the Brillouin bandwidth are amplified or attenuated simultaneously, the pump depletion effect in conventional BOTDA, which has a hollow of the Brillouin spectrum, can also be avoided. Therefore our single-shot method is available for long-range distributed fibre sensing.

The spatial resolution in our experiment is 20.48 m. Different from conventional BOTDA, the spatial resolution of single-shot BOTDA is determined by the subcarrier

frequency. For example, in our experiment the frequency spacing Δf is 4.88 MHz (2048 points over 10 GHz), therefore the spatial resolution is $v_g/(2\Delta f) = 20.48$ m, where v_g is the group velocity. Higher resolution can be achieved by increasing the Δf. However, since the Brillouin linewidth Δv_B is fixed, a larger frequency spacing means less data points in the stimulated Brillouin profile, which may increase the measurement error during the curve fitting process [144]. This problem can be solved by increasing the Brillouin linewidth, which can be realised by adding proper modulation on the pump [145], and will be presented in our future work.

5.7 Chapter conclusion

In conclusion, we have demonstrated a novel ultra-fast Brillouin fibre sensing method, which can monitor the distributed fibre status with only one-time measurement. Instead of the CW probe used in classic BOTDA, we adopt an orthogonal-sideband OFDM probe to acquire stimulated Brillouin spectrum and to diminish the polarisation fading. By carefully designing the OFDM symbol, we achieve a low PAPR signal which uniformly distributes the power in both time domain and frequency domain. Polarisation-diversity coherent detection is used to collect the full field information and to enhance the signal-to-noise ratio. We then conduct the distributed temperature sensing experiment in a 1.08 km standard single-mode fibre with a spatial resolution of 20.48 m. Sensing results show that the distributed Brillouin frequency shift can be successfully located by one-time measurement, with a temperature coefficient of 1.03 MHz/°C and 0.59 °C accuracy. This is, to the best of our knowledge, the first BOTDA that uses only one shot measurement and successfully locates the BFS along the fibre. There is no polarisation scrambling, averaging or frequency scanning in our scheme, indicating that the ultimate sensing speed is only limited by the fibre length, which can be a promising approach in distributed dynamic sensing. Results in this chapter have been published in [146–148]

Chapter 6

Complex-domain Brillouin fibre sensing technique

6.1 Motivation

BOTDA has achieved remarkable progress in distributed optical fibre sensing due to its high accurate distributed monitoring along the fibre [149]. A BOTDA system relies on the measurement of the Brillouin frequency shift (BFS), which has a linear relationship with the change of temperature or strain in the sensing fibre. Conventional BOTDA systems acquire the BFSs through fitting the distributed Brillouin gain spectrum (BGS) resulting in high sensing accuracy for distances of several kilometres. However, if the fibre is longer, the maximal power of injected pump and probe will be limited by stimulated Raman scattering, modulation instability [150] and non-local effects, resulting in a low BGS signal-to-noise-ratio (SNR) at the receiver. Therefore, averaging of many measurements is necessitated to improve the SNR, restricting both the sensing speed and the measurement precision.

In the past years, phase-based BOTDA system has become a promising alternative approach, which uses the Brillouin phase spectrum (BPS) instead of the BGS to estimate the Brillouin frequency shift [113, 139, 151–154]. Comparing with BGS method, fitting through BPS can bring several advantages such as the imperviousness to non-local effects [139], a quasi-linear region for dynamic sensing [151], and improvement in BFS estimation within a restricted frequency range [144]. Although most of the phase-based BOTDA systems can measure both BGS and BPS simultaneously, the BFSs are usually determined by BGS or BPS solely. For instance, in [139, 153, 154], BFS is determined by

either the Brillouin amplitude spectra or the phase-shift spectra separately. Some relations between the BGS and BPS, such as the angle [151] or the ratio [113], have also been explored for BFS estimation in dynamic sensing. Nevertheless, since the BGS and the BPS are derived from the same complex Brillouin spectrum (CBS) function, it is intuitive to consider that estimating the BFS with both BGS and BPS simultaneously can lead to better performance, as predicted in [152]. However, to date, this kind of improvement has not been quantitatively and experimentally investigated.

6.2 Method for Detecting the Complex Brillouin Spectrum

In a BOTDA system, when a continuous-wave (CW) probe $E_S = E_s \exp(2j\pi v_s t)$ meets the counter-propagating pump pulse $E_P = E_p \exp(2j\pi v_p t)$, and frequency difference $v_s - v_p$ is near the BFS v_B, stimulated Brillouin scattering (SBS) is induced. This is described by the complex transfer function that

$$H(v,z) = \exp[-h(v,z)], \tag{6.1}$$

where $h(v,z)$ is the complex Brillouin gain function written as [155]:

$$h(v,z) = \left[\frac{g_0(z)\Gamma_B}{\Gamma_B + 2j(v - v_B(z))}\right] \tag{6.2}$$

where $g_0(z)$ is the local gain factor of position z, Γ_B is the Brillouin linewidth, and $h(v,z)$ is the complex logarithmic gain, $j := \sqrt{-1}$ is the imaginary unit. The minus sign in $H(v,z)$ indicates that it is a Brillouin loss process, which the power is transferred from the CW probe to the pump pulse. Thus, $h(v,z)$ can be expressed as $h(v,z) = g(v,z) + j\varphi(v,z)$, where the real and the imaginary parts represent the BGS and the BPS respectively as

$$\begin{aligned} \mathrm{Re}[h(v,z)] = g(v,z) &= \frac{g_0(z)\Gamma_B^2}{\Gamma_B^2 + 4(v - v_B(z))^2} \\ \mathrm{Im}[h(v,z)] = \varphi(v,z) &= -\frac{2g_0(z)\Gamma_B(v - v_B(z))}{\Gamma_B^2 + 4(v - v_B(z))^2} \end{aligned} \tag{6.3}$$

and satisfy the Kramers-Kronig relations [155]. A three-dimensional plot of the CBS, along with its real and imaginary parts, is illustrated in Fig. 6.1.

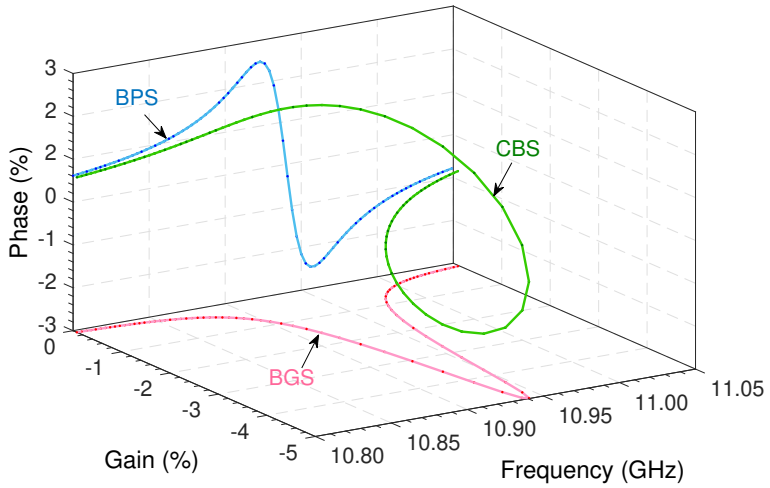

Figure 6.1: Complex Brillouin spectrum. The real and imaginary parts denote the corresponding BGS and the BPS, respectively.

To detect the complex Brillouin spectrum, we generate a reference light E_R that $E_R = E_r \exp(2j\pi v_r t)$ with the fixed frequency discrepancy $\Delta v = v_s - v_r > 2\Gamma_B$ to the probe light E_S. If the probe light interacts solely with the pump, the detected beating signal of the PD will be:

$$I_D = 2\alpha\eta E_r E_s \Big\{ \mathrm{Re}\left\{ \exp[-h(v,z) + 2j\pi\Delta v t + j\Delta\varphi] \right\} + n_D \Big\} \tag{6.4}$$

where α is the channel transmittance, η is the PD responsivity, $\Delta\varphi$ is the relative phase difference between probe and reference due to the chromatic dispersion and n_D is the received noise referred to $2\alpha\eta E_r E_s$. In a practical BOTDA system this noise may come from a variety of sources [142, 154]. For simplicity and without loss of generality, we assume here that n_D is dominated by an additive white Gaussian noise (AWGN) following the distribution of $\mathcal{N}(0, \sigma_D^2)$. The complex Brillouin spectrum $h(v,z)$ is determined with an IQ demodulation process by compensating the frequency offset (i.e. down-shifting the signal around frequency Δv to zero frequency by multiplying $\exp(-2j\pi\Delta t)$) and applying a digital low-pass filter with a $1/M$ bandwidth of the original detected signal

I_D. The filtered signal is then down-sampled by a factor of M and is factored out of $2\alpha\eta E_r E_s \exp(-j\Delta\varphi)$. The demodulated signal can be written as:

$$S_D = \exp[-h(v,z)] + n_I + jn_Q \tag{6.5}$$

where n_I and n_Q are two independent and identically distributed (i.i.d.) Gaussian random variables following $\mathcal{N}(0,\sigma_h^2)$, $\sigma_h^2 = \sigma_D^2/(2M)$. If the gain is small, i.e. $|h(v,z)| \ll 1$, we have $\exp[1-h(v,z)] \approx 1-h(v,z)$. Thus, the detected CBS contaminated by noise can be obtained through:

$$\hat{h}(v,z) \approx 1 - S_D = h(v,z) + n_h \tag{6.6}$$

where $n_h = n_I + jn_Q$ corresponding to the additive Gaussian noises of the real part and the imaginary part separately. For a long sensing distance, the complex gain is usually small to mitigate the non-local effect as well as other nonlinear distortion. Therefore, this small-gain approximation would be satisfied in a long-range BOTDA system..

To measure the CBS for BFS estimation, the probe light is scanned with N frequencies as vector $\mathbf{v} = [v_1, v_2, \ldots, v_N]^T$. The corresponding CBS of position z can be obtained as vector:

$$\mathbf{h}(z) = [\hat{h}(v_1,z), \hat{h}(v_2,z), \ldots, \hat{h}(v_N,z)]^T \tag{6.7}$$

which the real part $\mathbf{g}(z) = [g_i(z)] = \mathrm{Re}\{\mathbf{h}(z)\}$ corresponds to the BGS vector obtained in a gain-based BOTDA system, and the imaginary part $\boldsymbol{\phi}(z) = [\varphi_i(z)] = \mathrm{Im}\{\mathbf{h}(z)\}$ corresponds to the BPS vector obtained in a phase-based BOTDA system.

6.3 Theoretical analysis

6.3.1 BFS uncertainty estimated by BGS and BPS

The following step is to determine the BFS. To quantify the improvement of our proposed approach, we start from the BFS estimation process of the conventional gain-based BOTDA and phase-based BOTDA systems. Conventional BOTDA systems usually de-

termine the BFS by fitting the BGS or BPS solely to either equation in Eq. (6.3). To get a more accurate result, nonlinear least squares (NLS) regression is commonly utilised. This method seeks an optimal real coefficient vector $\mathbf{a} = [g_0, \Gamma_B, v_B]^T$ that minimises either the gain cost function:

$$f_g(\mathbf{a}) = \|g(\mathbf{v}, z) - \mathbf{g}(z)\|^2 \tag{6.8}$$

when BGS is used, or minimises the phase cost function:

$$f_\varphi(\mathbf{a}) = \|\varphi(\mathbf{v}, z) - \boldsymbol{\phi}(z)\|^2 \tag{6.9}$$

when BPS is used, where $\|\cdot\|$ is the Euclidean norm of an N-dimensional vector.

Minimising the cost functions (6.8) and (6.9) can be generalised as an optimisation problem [156] such that:

$$\min_{\mathbf{a}} f(\mathbf{a}) = \min_{\mathbf{a}} \sum_{i=1}^{N} \left| y(v_i; \mathbf{a}) - y_i \right|^2 \tag{6.10}$$

where $\mathbf{a} = [a_1, a_2, a_3]^T$(i.e.$[\mathrm{g_0}, \blacksquare_\mathrm{B}, \mathrm{v_B}]^\mathrm{T}$) $\in \mathbb{R}^3$; $y(v; \mathbf{a})$ and $\mathbf{y} = [y_i]_{N\times 1}$ denote the fitting function and measured data of BGS or BPS, depending on which cost function is used.

Assuming that the added random noise at each observation is normally distributed and has the identical variance σ_y^2, then the goodness of fit can be expressed as [157]

$$\chi^2(\mathbf{a}) = \frac{1}{\sigma_y^2} \sum_{i=1}^{N} \left| y(v_i; \mathbf{a}) - y_i \right|^2 = \frac{1}{\sigma_y^2} \mathbf{r}(\mathbf{a})^T \mathbf{r}(\mathbf{a}) \tag{6.11}$$

where χ^2 is the chi-square distribution, $\mathbf{r}(\mathbf{a}) = [r_m(\mathbf{a})]_{N\times 1} = y(\mathbf{v}; \mathbf{a}) - \mathbf{y}$ is the residual vector. Note that though $y(\mathbf{v}; \mathbf{a})$ is a column vector that the k-th element is calculated by $y(v_k; \mathbf{a})$ The result of such NLS regression is the coefficient vector $\mathbf{a}_0$ which minimises $\chi^2(\mathbf{a})$[157]. Assuming that the fitting function $y(v; \mathbf{a})$ is differentiable around $\mathbf{a}_0$. Standard references on statistics and data analysis give the well-known result that the variances of the coefficients are given by the co-variance matrix $\mathbf{Q}$ that [157]:

$$\mathbf{Q}(\mathbf{a}_0) = [Q_{mn}(\mathbf{a}_0)]_{3\times 3} = \sigma_y^2 \mathbf{C}(\mathbf{a}_0)^{-1} \tag{6.12}$$

where $\mathbf{C}$ is the curvature matrix (or called the Hessian matrix) which can be approximated via

$$\mathbf{C}(\mathbf{a}) = \mathbf{J}(\mathbf{a})^T \mathbf{J}(\mathbf{a}) \tag{6.13}$$

by ignoring higher order terms [156]. $\mathbf{J}(\mathbf{a})$ is the Jacobian matrix with elements defined as

$$[\mathbf{J}(\mathbf{a})]_{mn} = \frac{\partial r_m(\mathbf{a})}{\partial a_n} = \frac{\partial y(v_m; \mathbf{a})}{\partial a_n} \tag{6.14}$$

where $m \in \{1, \ldots, N\}$ and $n \in \{1, 2, 3\}$. The standard deviation of parameter a_3 is exactly the accuracy of the BFS estimation, i.e.:

$$\sigma_{v_B} = \sqrt{Q_{33}(\mathbf{a}_0)} \tag{6.15}$$

If the BFS v_B (a_3) is determined by the BGS, according to Eq. (6.3), we have $y_i = g_i$, $\sigma_y = \sigma_g$. The function $y(v; \mathbf{a})$ will be

$$y(v_i; \mathbf{a}) = g(v_i; \mathbf{a}) = \frac{a_1 a_2}{a_2^2 + 4(v_i - a_3)^2} = \frac{a_1}{1 + 4t_i^2} \tag{6.16}$$

where $t_i = (v_i - a_3)/a_2$. The matrix $\mathbf{C}$ can be computed through Eqs. (6.13) and (6.14) with the elements:

$$\begin{aligned}
c_{11} &= \sum_{i=1}^{N} \frac{1}{(1+4t_i^2)^2} \\
c_{12} &= \sum_{i=1}^{N} \frac{8\gamma t_i^2}{(1+4t_i^2)^3} = c_{21} \\
c_{13} &= \sum_{i=1}^{N} \frac{8\gamma t_i}{(1+4t_i^2)^3} = c_{31} \\
c_{22} &= \sum_{i=1}^{N} \frac{64\gamma^2 t_i^4}{(1+4t_i^2)^4} \\
c_{23} &= \sum_{i=1}^{N} \frac{64\gamma^2 t_i^3}{(1+4t_i^2)^4} = c_{32} \\
c_{33} &= \sum_{i=1}^{N} \frac{64\gamma^2 t_i^2}{(1+4t_i^2)^4}
\end{aligned} \tag{6.17}$$

where $\gamma = a_1/a_2$.

Since the calculation of co-variance matrix $\mathbf{Q}$ in Eq. (6.12) requires the inversion of the curvature matrix $\mathbf{C}$, the theoretical expression for σ_{v_B} could be quite cumbersome. Nevertheless, if the scanned frequencies $\mathbf{v}$ are uniformly and symmetrically distributed around the central value a_3, which is the simplest and in fact the the most common case as assumed in [102, 144, 157], the expressions can be significantly simplified. Then we have $c_{13} = c_{31} = c_{23} = c_{32} = 0$ and the inverse of matrix $\mathbf{C}$ can be explicitly written as

$$\mathbf{C}^{-1} = \begin{bmatrix} \frac{c_{22}}{c_{11}c_{22}-c_{12}^2} & -\frac{c_{12}}{c_{11}c_{22}-c_{12}^2} & 0 \\ -\frac{c_{12}}{c_{11}c_{22}-c_{12}^2} & \frac{c_{11}}{c_{11}c_{22}-c_{12}^2} & 0 \\ 0 & 0 & \frac{1}{c_{33}} \end{bmatrix} \tag{6.18}$$

and the BFS uncertainty becomes

$$\sigma_{v_B}^{(g)} = \sqrt{Q_{33}(\mathbf{a_0})} = \sigma_g \sqrt{\frac{\delta_t}{\gamma^2} S_g^{-1}} \tag{6.19}$$

where the superscript '(g)' of σ_{v_B} denotes that it is calculated with the BGS function, δ_t is defined as δ_v/a_2, and S_g is a sum of series which is given by

$$S_g = \sum_{i=1}^{N} \frac{64 t_i^2 \delta_t}{(1+4t_i^2)^4} \tag{6.20}$$

Similarly, if the BFS is estimated with the BPS, we have $y_i = \varphi_i$, $\sigma_y = \sigma_\varphi$. The function $y(v; \mathbf{a})$ becomes

$$y(v_i; \mathbf{a}) = \varphi(v_i; \mathbf{a}) = \frac{2a_1a_2(v_i - a_3)}{a_2^2 + 4(v_i - a_3)^2} = \frac{2\gamma t_i}{1+4t_i^2} \tag{6.21}$$

Following the same calculation steps as the BGS case, the elements of $\mathbf{C}$ when BPS is used will be

$$\begin{aligned} c_{11} &= \sum_{i=1}^{N} \frac{4t_i^2}{(1+4t_i^2)^2} \\ c_{12} &= \sum_{i=1}^{N} \frac{-4\gamma(1-4t_i^2)t_i^2}{(1+4t_i^2)^3} = c_{21} \end{aligned}$$

$$
\begin{aligned}
c_{13} &= \sum_{i=1}^{N} \frac{-4\gamma(1-4t_i^2)t_i}{(1+4t_i^2)^3} = c_{31} \\
c_{22} &= \sum_{i=1}^{N} \frac{4\gamma^2(1-4t_i^2)^2 t_i^2}{(1+4t_i^2)^4} \\
c_{23} &= \sum_{i=1}^{N} \frac{4\gamma^2(1-4t_i^2)^2 t_i}{(1+4t_i^2)^4} = c_{32} \\
c_{33} &= \sum_{i=1}^{N} \frac{4\gamma^2(1-4t_i^2)^2}{(1+4t_i^2)^4}
\end{aligned}
\tag{6.22}
$$

When the scanned frequencies are uniformly and symmetrically distributed around the central value, as assumed in the BGS case, the inverse of matrix $\mathbf{C}$ still has the form of Eq. (6.18). Therefore the BFS uncertainty fit by BPS is written as

$$
\sigma_{v_B}^{(\varphi)} = \sqrt{Q_{33}(\mathbf{a_0})} = \sigma_\varphi \sqrt{\frac{\delta_t}{\gamma^2} S_\varphi^{-1}}
\tag{6.23}
$$

where the superscript '(φ)' indicates that it is calculated by the BPS, and S_φ is a sum of series given by

$$
S_\varphi = \sum_{i=1}^{N} \frac{4(1-4t_i^2)^2 \delta_t}{(1+4t_i^2)^4}
\tag{6.24}
$$

No matter the BGS or BPS is used, for a given symmetric data points the BFS uncertainty can be directly given via Eqs. (6.19) or (6.23), along with the sums S_g or S_φ . Generally speaking, the above sums do not have closed-form expressions. But when N is sufficient large and δ_t is sufficient small, they could be written in terms of integrals [157]. Consider that the scanned N data points occupy a fixed range L, i.e. $L = N\delta_t = N\delta_v/a_2$. If $L > 4$ (the reason why 4 is chosen will be discussed below), then we have

$$
\lim_{N\to\infty} S_g = \int_{-\infty}^{\infty} \frac{64t^2}{(1+4t^2)^4} dt = \frac{\pi}{2}
\tag{6.25}
$$

$$
\lim_{N\to\infty} S_\varphi = \int_{-\infty}^{\infty} \frac{4(1-4t^2)^2}{(1+4t^2)^4} dt = \frac{\pi}{2}
\tag{6.26}
$$

The reason we choose 4 as the threshold for L is that above integration from -2 to $+2$ will cover sufficient range of their limits (i.e. 99.83% for S_g and 98.93% for S_φ). Therefore

the asymptotic closed-form expressions of $\sigma_{v_B}^{(g)}$ and $\sigma_{v_B}^{(\varphi)}$ are given by

$$\tilde{\sigma}_{v_B}^{(g)} = \sigma_g \sqrt{\frac{2}{\pi a_1^2} a_2^2 \delta_t} = \frac{\sigma_g}{g_0} \sqrt{\frac{2}{\pi} \delta_v \Gamma_B} \tag{6.27}$$

and

$$\tilde{\sigma}_{v_B}^{(\varphi)} = \sigma_\varphi \sqrt{\frac{2}{\pi a_1^2} a_2^2 \delta_t} = \frac{\sigma_\varphi}{g_0} \sqrt{\frac{2}{\pi} \delta_v \Gamma_B}, \tag{6.28}$$

indicating that if the BGS and BPS have the same noise variance, i.e. $\sigma_g = \sigma_\varphi$, the BFS estimated by the gain spectrum or the phase spectrum will have similar uncertainty, which is coincident with the conclusion in [144]. It is also worth noting that our expressions have almost identical form with [136] except the scalar coefficient. The coefficient $\sqrt{2/\pi}$ in our equations is smaller than that of $\sqrt{3/4}$ in [136], since we adopt the nonlinear model instead of the quadratic model in that reference.

6.3.2 BFS uncertainty estimated on complex domain

In our complex BOTDA approach, we consider $h(v,z) = g(v,z) + j\varphi(v,z)$ as a complex function instead of partitioning it into phase and gain separately. Then the observed data for $h(v,z)$ will be $\mathbf{h}(z) = \mathbf{g}(z) + j\boldsymbol{\phi}(z)$. To fit this complex set of data, we adopt the complex nonlinear least squares (CNLS) regression method instead of the NLS method used with BGS/BPS. The CNLS regression was developed several decades ago as an extension of the NLS method [158], and has been applied extensively for complex impedance spectroscopy [159], [160]. Comparing with NLS, the CNLS regression provides an improved performance since a complex-valued fit model is used for simultaneous regression to both the real and imaginary parts of the measured spectrum [161]. In this case, the cost function can be written as

$$f_h(\mathbf{a}) = \|h(\mathbf{v}, z) - \mathbf{h}(z)\|^2 \tag{6.29}$$

and minimising this in the complex domain. Minimising the cost function (6.29) can be generalised as an optimisation problem [156] such that

$$\min_{\mathbf{a}} f(\mathbf{a}) = \min_{\mathbf{a}} \sum_{i=1}^{N} \left| y(v_i; \mathbf{a}) - y_i \right|^2 \tag{6.30}$$

where $y(v; \mathbf{a})$ and $\mathbf{y} = [y_i]_{N\times 1} \in \mathbb{C}^N$ denote the ideal complex function and measured complex data of CBS. Assigning $\mathrm{Re}[y(v_i; \mathbf{a})] = Y_i^{\mathrm{Re}}$, $\mathrm{Im}[y(v_i; \mathbf{a})] = Y_i^{\mathrm{Im}}$, $\mathrm{Re}[y_i] = y_i^{\mathrm{Re}}$ and $\mathrm{Im}[y_i] = y_i^{\mathrm{Im}}$, then Eq. (6.30) can be rewritten as

$$\begin{aligned} &\min_{\mathbf{a}} \sum_{i=1}^{N} \left| \left(Y_i^{\mathrm{Re}} - y_i^{\mathrm{Re}}\right) + j\left(Y_i^{\mathrm{Im}} - y_i^{\mathrm{Im}}\right) \right|^2 \\ &= \min_{\mathbf{a}} \sum_{i=1}^{N} \left\{ \left(Y_i^{\mathrm{Re}} - y_i^{\mathrm{Re}}\right)^2 + \left(Y_i^{\mathrm{Im}} - y_i^{\mathrm{Im}}\right)^2 \right\} \end{aligned} \tag{6.31}$$

which is equivalent to

$$\min_{\mathbf{a}} \|\bar{\mathbf{Y}} - \bar{\mathbf{y}}\|^2 = \min_{\mathbf{a}} \sum_{i=1}^{2N} \left| \bar{Y}_i - \bar{y}_i \right|^2 \tag{6.32}$$

where $\bar{\mathbf{Y}}, \bar{\mathbf{y}} \in \mathbb{R}^{2N}$ are extended vectors defined as

$$\begin{aligned} \bar{\mathbf{Y}} &= [\bar{Y}_i]_{2N\times 1} = [Y_1^{\mathrm{Re}}, \ldots, Y_N^{\mathrm{Re}}, Y_1^{\mathrm{Im}}, \ldots, Y_N^{\mathrm{Im}}]^T \\ \bar{\mathbf{y}} &= [\bar{y}_i]_{2N\times 1} = [y_1^{\mathrm{Re}}, \ldots, y_N^{\mathrm{Re}}, y_1^{\mathrm{Im}}, \ldots, y_N^{\mathrm{Im}}]^T \end{aligned} \tag{6.33}$$

Assuming the real and imaginary parts of the added complex random Gaussian noise have the same variance σ_y^2, then the goodness of fit can be expressed as:

$$\chi^2(\mathbf{a}) = \frac{1}{\sigma_y^2} \sum_{i=1}^{2N} \left| \bar{Y}_i - \bar{y}_i \right|^2 = \frac{1}{\sigma_y^2} \bar{\mathbf{r}}(\mathbf{a})^T \bar{\mathbf{r}}(\mathbf{a}) \tag{6.34}$$

where the residual vector becomes $\bar{\mathbf{r}}(\mathbf{a}) = [\bar{r}_m(\mathbf{a})]_{2N\times 1} = \bar{\mathbf{Y}} - \bar{\mathbf{y}}$. As we discussed above, the co-variance matrix $\mathbf{Q}$ can be computed by inverting the curvature matrix $\mathbf{C}$, which is calculated through the Jacobian matrix. In this case, the Jacobian matrix $\bar{\mathbf{J}}$ becomes

$$[\bar{\mathbf{J}}(\mathbf{a})]_{mn} = \frac{\partial \bar{r}_m(\mathbf{a})}{\partial a_n} = \frac{\partial \bar{Y}_m}{\partial a_n} \tag{6.35}$$

where $m \in \{1, \ldots, 2N\}$ and $n \in \{1, 2, 3\}$.

When CBS is used for BFS estimation, we substitute $h(v_i; \mathbf{a})$ and h_i into $y(v_i; \mathbf{a})$ and y_i, respectively. σ_y is assigned to be σ_h as described in Section 6.2. Then, straightforward calculation gives the expression of elements of $\mathbf{C}$ as

$$\begin{aligned}
c_{11} &= \sum_{i=1}^{N} \frac{1}{1+4t_i^2} \\
c_{12} &= \sum_{i=1}^{N} \frac{4\gamma t_i^2}{(1+4t_i^2)^2} = c_{21} \\
c_{13} &= \sum_{i=1}^{N} \frac{4\gamma t_i}{(1+4t_i^2)^2} = c_{31} \\
c_{22} &= \sum_{i=1}^{N} \frac{4\gamma^2 t_i^2}{(1+4t_i^2)^2} \\
c_{23} &= \sum_{i=1}^{N} \frac{4\gamma^2 t_i}{(1+4t_i^2)^2} = c_{32} \\
c_{33} &= \sum_{i=1}^{N} \frac{4\gamma^2}{(1+4t_i^2)^2}
\end{aligned} \tag{6.36}$$

Under the symmetric assumption as in section 6.3.1, the uncertainty of BFS determined by the CBS can be written as

$$\sigma_{v_B}^{(h)} = \sqrt{Q_{33}(\mathbf{a_0})} = \sigma_h \sqrt{\frac{\delta_t}{\gamma^2} S_h^{-1}} \tag{6.37}$$

where the superscript '(h)' indicates that it is calculated with BGS function, and sum S_h is expressed as

$$S_h = \sum_{i=1}^{N} \frac{4\delta_t}{(1+4t_i^2)^2} \tag{6.38}$$

The asymptotic closed-form can be obtained through the similar steps in section 6.3.1. Considering the scanned N data points within a fixed range $L = N\delta_t > 4$, when $N \to \infty$, $\delta_t = L/N \to 0$. Therefore we have

$$\lim_{N\to\infty} S_h = \int_{-\infty}^{\infty} \frac{4}{(1+4t^2)^2} dt = \pi \tag{6.39}$$

Thus, the asymptotic BFS uncertainty by CBS will be

$$\tilde{\sigma}_{v_B}^{(h)} = \sigma_h \sqrt{\frac{1}{\pi a_1^2} a_2^2 \delta_t} = \frac{\sigma_h}{g_0} \sqrt{\frac{1}{\pi} \delta_v \Gamma_B} \tag{6.40}$$

It is obvious that $S_h = S_g + S_\varphi$, indicating that if $S_g \approx S_h$ and $\sigma_g(z) = \sigma_\varphi(z) = \sigma_h(z)$, then $\sigma_{v_B}^{(h)}(z) \doteq \sigma_{v_B}^{(g)}(z)/\sqrt{2} \doteq \sigma_{v_B}^{(\varphi)}(z)/\sqrt{2}$, indicating the BFS uncertainty fit by CBS is about $\sqrt{2}$ times smaller than that obtained by BGS or BPS solely. Moreover, the asymptotic expressions (6.27) (6.28) and (6.40) also reveal this kind of improvement.

6.4 Monte-Carlo Simulation

To validate the theoretical predictions, we perform the Monte-Carlo simulation by repeatedly constructing a ideal CBS vector $h(\mathbf{v}; \mathbf{a})$ with complex random Gaussian white noise $\mathbf{n}_h = [n_h(v_i)]_{N\times 1}$, resulting $\mathbf{h} = h(\mathbf{v}; \mathbf{a}) + \mathbf{n}_h$. The scanned frequency $\mathbf{v}$ of CBS is set from 10890 MHz to 11010 MHz, with a frequency interval δ_v of 3 MHz. The Brillouin linewidth Γ_B is assigned to 35 MHz, and the BFS v_B is set to 10950 MHz. The added noise σ_h is fixed at 0.005, while the local gain factor g_0 is controlled by the value of SNR. In different literature the SNR may have various definitions [102,154,162,163]. In this paper we define the SNR as

$$SNR = 10 \log_{10} \left[g_0^2 / \sigma_h^2 \right] \text{ (dB)} \tag{6.41}$$

which is identical to the definition in [154,163] but in the decibel unit. The SNR is gradually increased from 9 dB to 23 dB with 1 dB step size, corresponding to a g_0 tuned from 1.41% to 7.06%. Notice that in [102,144] the SNR is defined as the ratio between the maximal gain g_0 and the noise standard deviation, which can be treated as the amplitude SNR_a. Thus our simulated SNR range from 9 dB to 23 dB equals to the SNR_a range from 2.8 to 14.1, which is in accord with the analysis range in [144].

The BFS is then estimated by fitting the vector $\mathbf{h}$ with the CBS function $h(v; \mathbf{a})$ through the CNLS regression. To explore the improvement of our method, we also perform NLS regression to estimate BFS by fitting the real part (i.e. the BGS) and the imaginary part (i.e. the BPS) of $\mathbf{h}$ with the ideal BGS and BPS functions in Eq. (6.3), respectively. The

Levernberg-Marquardt algorithm is employed to solve both the NLS and CNLS problem. The standard deviation of estimated BFS error, which reflects the BFS uncertainty and sensing accuracy, is then calculated by 10^4 Monte-Carlo simulations of each SNR value, while the termination tolerance of nonlinear regression is set to 10^{-12}.

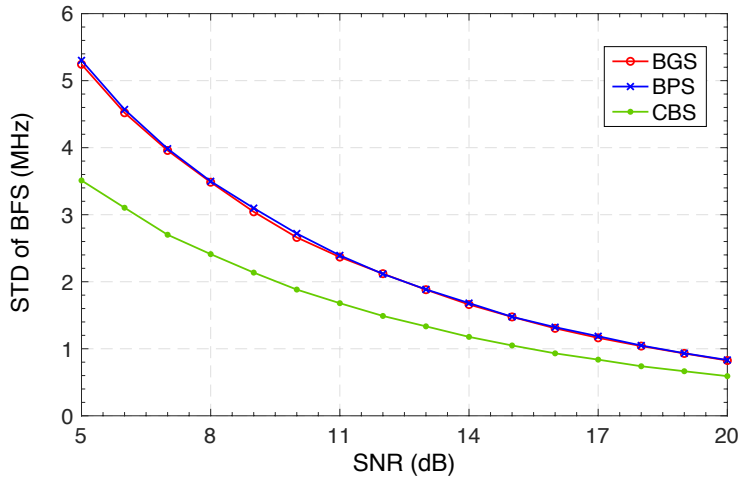

Figure 6.2: Simulated and theoretical standard deviations of the BFS values versus SNR based on BGS, BPS and CBS, respectively. Simulated points are from the statics of 10^4 Monte-Carlo simulation. Theoretical results are calculated through Eqs. (6.19), (6.23),(6.20),(6.24),(6.37) and (6.38).

The simulation results are depicted in Fig. 6.2. The markers denote the simulated results, and the solid lines are the theoretical results calculated through Eqs. (6.19), (6.23), (6.20), (6.24), (6.37) and (6.38). We also calculate the BFS uncertainty with the asymptotic expressions in Eqs. (6.27), (6.28), (6.40) and find that they are almost identical with the solid curves. The results show a remarkable agreement between the theoretical predictions and simulated results. The BFS uncertainty determined by BGS and BPS has the same performance, while BFS uncertainty fit by the CBS is approximately $\sqrt{2}$ times smaller than the estimated by either BGS or BPS solely. Meanwhile, for the same accuracy level, estimation by CBS can reduce the SNR requirement by 3 dB, as shown in Fig. 6.2. This result validate the fact that the BFS estimation in the complex domain will result in $\sqrt{2}$ times uncertainty reduction or 3-dB SNR improvement, compared to estimates based solely on either BGS or BPS.

Fig. 6.3 shows the simulated and theoretical BFS uncertainty with different fitting

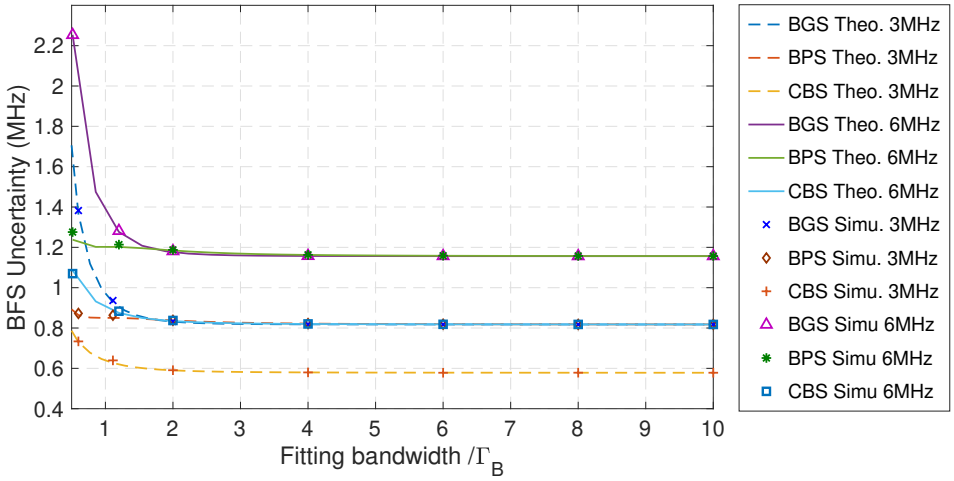

Figure 6.3: Simulated and theoretical standard deviation of BFS with different scanned bandwidth and frequency interval. Simu.: simulated results; Theo.: theoretical results. The bandwidth has been normalised to the Brillouin linewidth. SNR is set to 20 dB. Simulated points are from the statistics of 10^4 Monte-Carlo simulations.

bandwidth and frequency steps. The scanned bandwidth is normalised to the Brillouin linewidth. We find that when the normalised bandwidth is very narrow, such as from 0.5 to 1, BFS uncertainty by the BGS is much larger than that by the BPS, which is consistent with [144]. When the normalised bandwidth is larger than 2, the BFS estimated by BGS and BPS has the similar performance (BGS is slightly better than BPS), both of which are approximately $\sqrt{2}$ times of the result with CBS. With a larger frequency step (6 MHz), BFS uncertainty is almost $\sqrt{2}$ times of the result with the original case (3 MHz), which is consistent with our theory. From the practical point of view, a successful BOTDA system should be able to detect the potential temperature or strain in the FUT, so the normalised scanned bandwidth range is usually larger than $\sqrt{2}$. Therefore, the results indicate that the $\sqrt{2}$ improvement of our complex method is valid when a practical scanned bandwidth is considered, and the simulated results match very well with our theoretical predictions. Even at the special condition that the scanned bandwidth is less than 1, our complex method still has improvement comparing with the BGS or BPS methods. Another interesting result is that the BFS uncertainty with normalised bandwidth larger than 4 converges to a constant value,indicating that fitting with $4\Gamma_B$ is sufficient for a stable sensing accuracy.

6.5 Sys tem layout

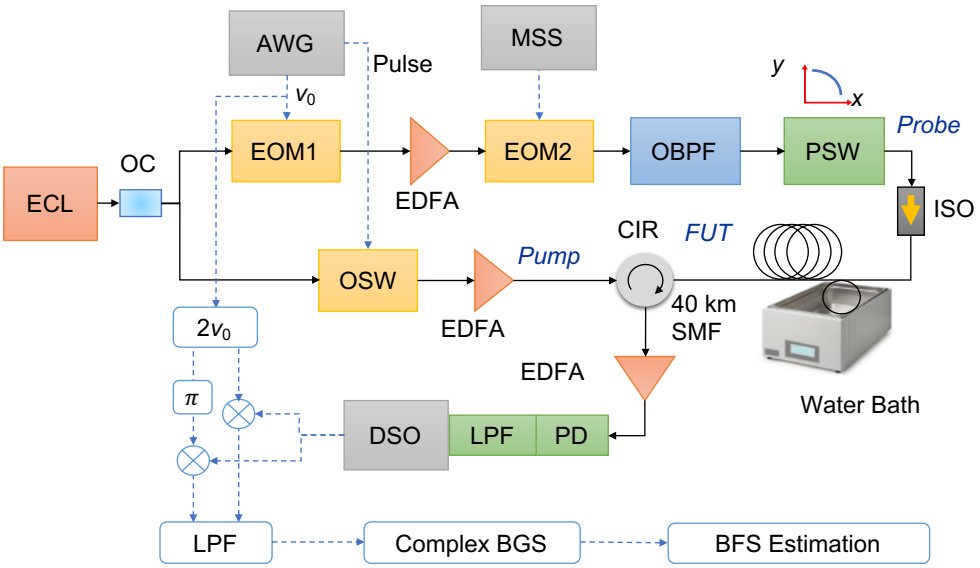

Figure 6.4: Experimental setup of the complex-domain BOTDA.

To validate this significant improvement, we conduct a distributed temperature sensing experiment with 40-km standard single-mode fibre (SSMF). Fig. 6.4 is the experimental setup of our complex BOTDA scheme. An external cavity laser (ECL) centred at 1545 nm with a 100 kHz linewidth is divided into two parts as the probe and pump by a 3-dB optical coupler (OC). The probe wave is firstly double-sideband modulated by a 200 MHz sine wave with a 20 dB suppressed carrier. Then it is up-shifted by a microwave synthesizer (MSS) sweeping from 10924 MHz to 11044 MHz with a 3 MHz interval. A commercial dense wavelength division multiplexer (DWDM) with a sharp falling slope (30 dB over 10 GHz) is used as the optical bandpass filter (OBPF) to eliminate undesired light waves. The probe light is then sent into the fibre through an optical isolator (ISO).

The pump pulse is modulated by an optical switch (OSW) with a 4.2 kHz repetition rate. The pulse width is 100 ns, corresponding to a spatial resolution of 10 meters. To mitigate the polarisation fading along the fibre, a polarisation scrambler (PS) is used to randomly scramble the state of polarisation (SOP) of the pump. A 40-km SSMF spool is used as the fibre under test (FUT) with the last 20 m of placed in a temperature controlled water bath. To avoid pump depletion and the non-local effect, the average power of

probe and pump is set to -8 dBm and -6 dBm, respectively. The received signal is amplified by a Erbium-doped fibre amplifier (EDFA), then converted into electrical signal by a photo-detector (PD), and finally collected by a digital storage oscilloscope (DSO) sampling at 1.25 GSa/s. Since the bandwidth of PD is much greater than the sampling rate of DSO, an 575MHz analogue low-pass filter (LPF) is applied as an anti-aliasing filter before analogue-to-digital conversion. The received data is first mixed with the double frequency of a 200 MHz sine wave and then filtered out by a 125 MHz bandwidth digital LPF, leading to an M factor for the IQ demodulation procedure equals to 10. The filtered data is finally for CBS extraction, as well as the BFS estimation.

6.6 Experimental results

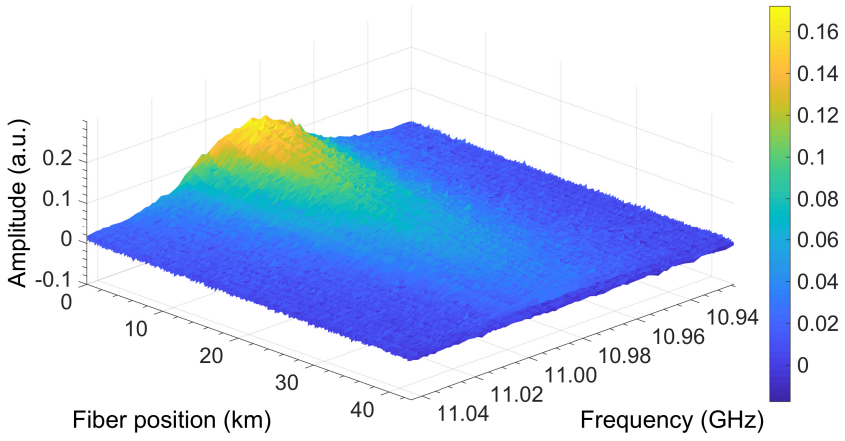

Figure 6.5: The three-dimensional views of the real part of the distributed complex Brillouin spectrum, i.e. the distributed Brillouin gain spectrum.

Figs. 6.5 and 6.6 show the three-dimensional views of the distributed Brillouin gain and phase in a 40-km FUT obtained from 50-time averaging. The spectrograms may look noisy because we intentionally acquire them through limited times averaging per scanned each frequency, in order to provide an obvious demonstration of our improvement. It is well-known that the noise variance is inversely proportional to N_{av}, where N_{av} is the number of traces taken into the averaging process[102, 164]. So the SNR will be improved if more averaging times are used. The maximal local gain factor is approximately

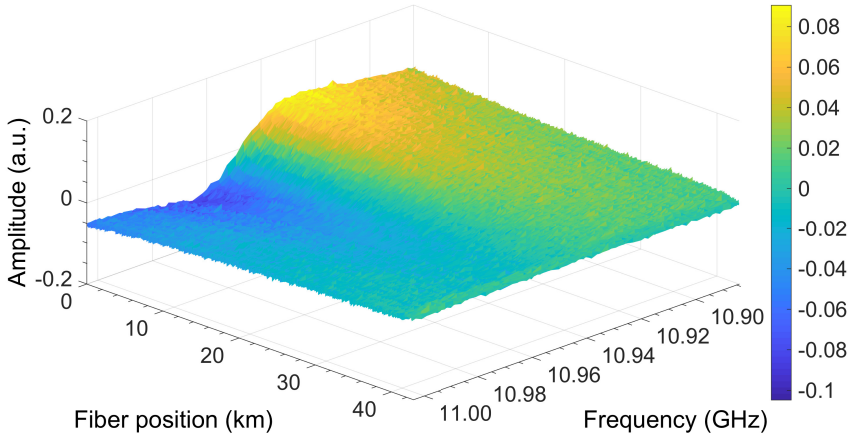

Figure 6.6: The three-dimensional views of the imaginary part of the distributed complex Brillouin spectrum, i.e. the distributed Brillouin phase spectrum.

0.1557, while the minimal local gain factor is about 0.0257%. The standard deviation of noise is 0.0056, indicating that the SNR decreases from 28.88 dB to 13.22 dB along the fibre.

We then characterise the statistics of the complex noise added on the CBS. Fig. 6.7(a) is the scatter diagram of the noise with 10^5 samples. The mean value of the noise equals to zero and the samples scatter as a thermal state. Fig. 6.7(b) shows the probability density distribution of the real and imaginary parts of the noise. Both of them have almost identical distribution, which fits well with the ideal Gaussian distribution (green line) in Fig. 6.7(b). The correlation coefficient between the real and imaginary parts is 0.003, confirming our assumption that they are independently and identically distributed. The variance of the real/imaginary component is 0.0056. According to the measured distributed spectrum, the maximal local gain factor is 0.1557, while the minimal local gain factor is 0.0257. Thus, the SNR decreases from 28.88 dB to 13.22 dB along the fibre.

We compare the estimates of the distributed BFS based on the nonlinear least squares fitting methods of the BGS, the BPS and the CBS. Fig. 6.8 depicts the BFS results obtained by these three approaches. The BFS values estimated by BGS and BPS have a similar amplitude fluctuation, while the BFS fluctuation by CBS in the complex-domain is noticeably smaller. Fig. 6.9 represents the standard deviation of BFS (i.e. σ_{v_B}) by calculating

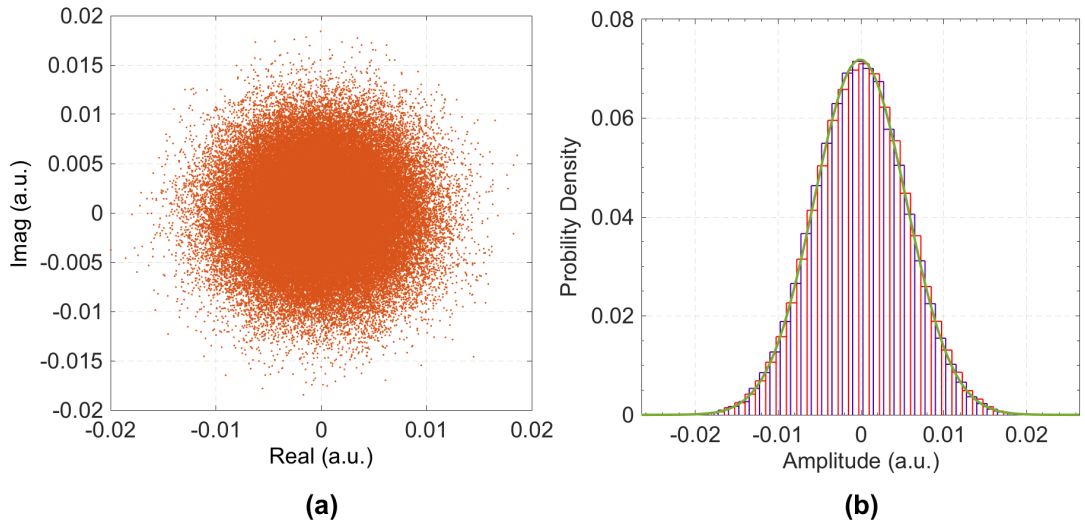

Figure 6.7: Statistical characterisation of the complex noise added on the CBS. (a) The scatter diagram of the real and imaginary components of the complex noise. (b) The probability density distribution of the real (red bars) and imaginary (blue bars) components, respectively. The thick green curve is the theoretical Gaussian distribution

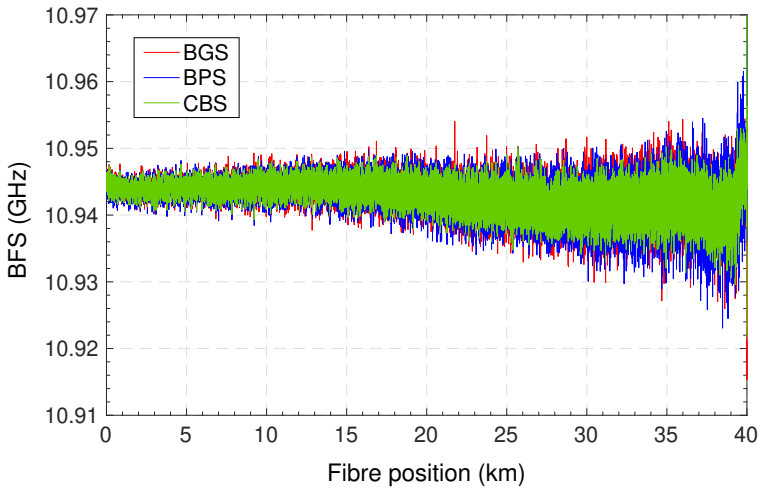

Figure 6.8: The estimated BFS by separately using the BGS, the BPS and the CBS.

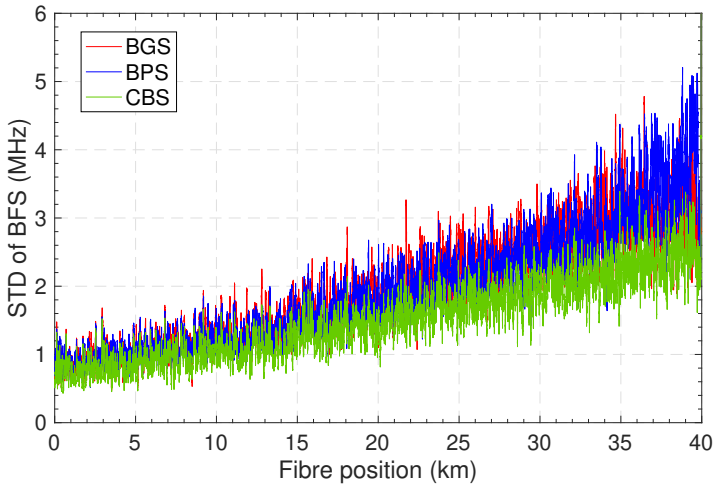

Figure 6.9: The standard deviation of 50 consecutive BFS by using the BGS, the BPS and the CBS, separately.

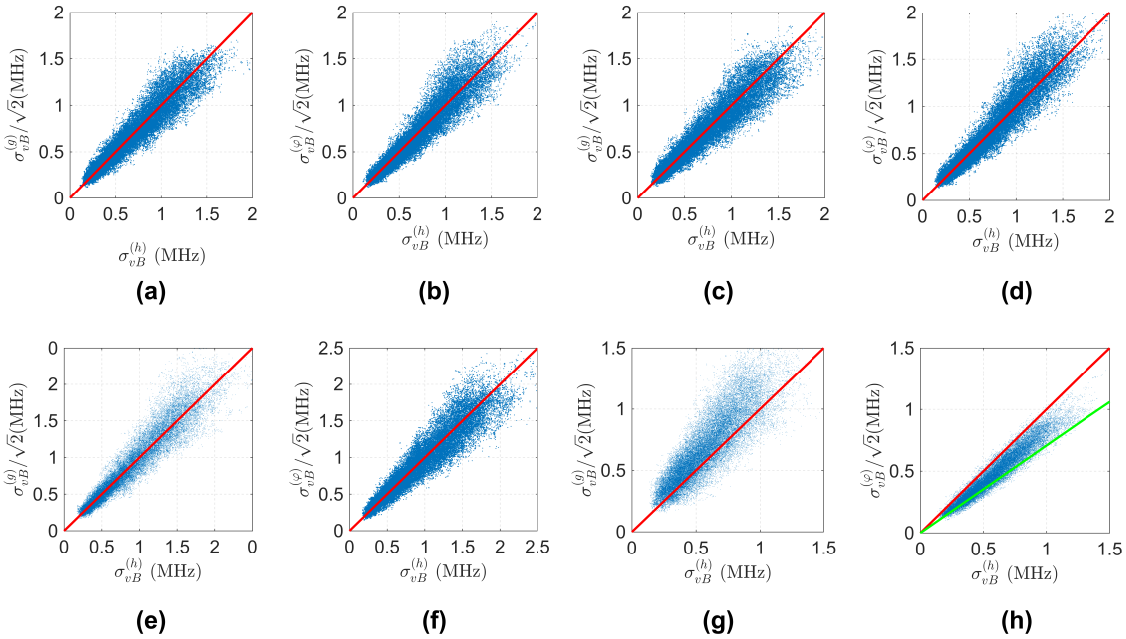

Figure 6.10: The relationship between CBS-based BFS uncertainty and BGS/BPS-based BFS uncertainty with different scanned bandwidth and frequency step.

a set of 50 consecutive BFSs. The standard deviation of these BFSs estimated by the BGS and BPS have similar performance, while the standard deviation of BFS from the CBS is considerably reduced.

To quantify the improvement, the relationships between the CBS-based BFS uncertainty $\sigma_{v_B}^{(h)}$ and the BGS/BPS-based BFS uncertainty ($\sigma_{v_B}^{(g)}$ or $\sigma_{v_B}^{(\varphi)}$) divided by $\sqrt{2}$ are depicted in Fig. 6.10(a) and (b), respectively. The BFS uncertainty points are scattered near the expected unity slopes (red solid lines), verifying the agreement between our theoretical prediction and the experimental results. Fig. 6.10(c) and (d) are the cases where the BFS is fit with half of the scanned bandwidth.Fig. 6.10(e) and (f) are the cases where the BFS is fit with double of the frequency step. We can see that the $\sqrt{2}$ improvement is still valid in these scenarios, as we predicted in the theory and simulation. Fig. 6.10(g) and (h) are the special condition under which a very narrow bandwidth (i.e., 21 MHz or 0.6 normalised bandwidth) is scanned. As we predicted, $\sigma_{v_B}^{(g)}$ rises above the $\sqrt{2}$ times of $\sigma_{v_B}^{(h)}$ while $\sigma_{v_B}^{(\varphi)}$ falls below the $\sqrt{2}$ times of $\sigma_{v_B}^{(h)}$, which is consistent with the results in [144]. In Fig 6.10(h), the solid green line indicates that the $\sigma_{v_B}^{(h)}$ equals to $\sigma_{v_B}^{(\varphi)}$. We can find that most of the data points are distributed between the red and the green lines, which means when the fitting bandwidth is narrow, the improvement of our approach will be smaller than $\sqrt{2}$. Meanwhile, most of the data points are still above the green solid line, indicating that our complex method still has improvement even with such narrow bandwidth.

To evaluate the practical sensing performance of our proposed technique, the temperature of water bath containing a 20 m fibre segment at the far end of the 40 km length is increased from 25 °C to 65 °C with 10 °C steps. The probe frequency is scanned from 10890 MHz to 11040 MHz with an interval of 3 MHz. To get more accurate results, the data traces are averaged by 100 times per scanned frequency. Since the spatial resolution is 10 meters and there is no applied strain at the far-end of FUT, it is reasonable to assume that the BFS within this heated 20 m segment fibre is uniform. We then estimate the BFS of this segment by repeating measurement with BGS, BPS and CBS, respectively. Fig. 6.11 shows the mean BFS values in the 20-m segment at different temperatures. It can be found that the BFS data obtained from BGS, BPS and CBS are well superposed . Lin-

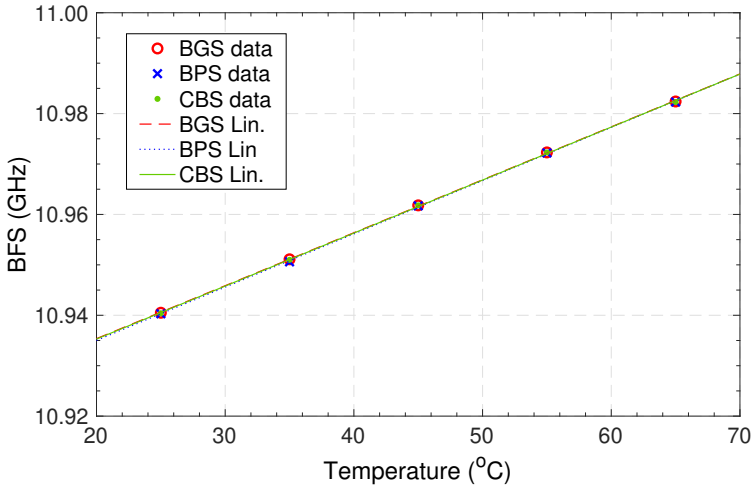

Figure 6.11: Mean estimated BFS v_B of different temperature by BGS, BPS and CBS at the far-end of 40km. Linear regression (Lin.) is performed on these BFS data.

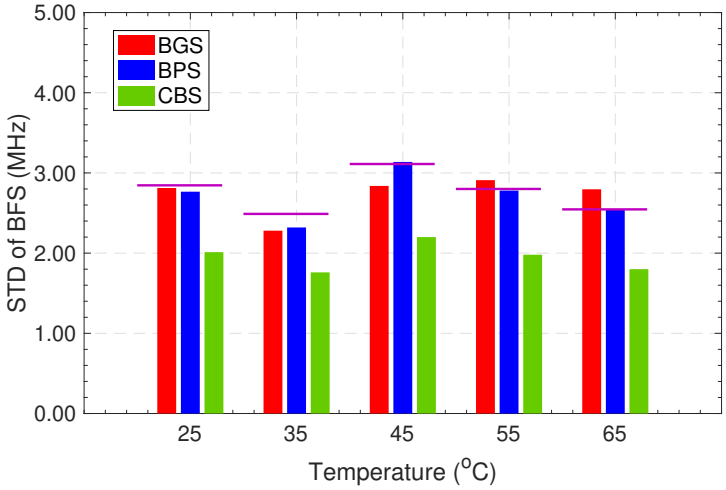

Figure 6.12: Standard deviation σ_{v_B} of the BFS at various temperature, from both experimental results and theoretical predictions. Exp.: experimental, Theo.: theoretical.

ear regression is then conducted on these BFS data points. The temperature coefficients calculated by BGS, BPS and CBS are 1.050 MHz/°C, 1.056 MHz/°C and 1.051 MHz/°C, respectively. The coefficients of determination (R^2) of these three methods are all above 99.8%, indicating that a promising linear relationship is achieved for distributed temperature sensing. This result confirm the fact that the measured BFS can really retrieve the real temperature change amount. We also compute the standard deviation of the BFS at various temperatures, as shown in Fig. 6.12. Comparing with the estimates from the BGS and BPS, the results from the CBS have a obviously lower BFS uncertainty, meaning that our complex BOTDA is more accurate and reliable. The $\sqrt{2}$ times of the BFS uncertainty by CBS versus temperature are plotted in Fig. 6.12 as the horizontal purple lines. The accordance between the purple lines and the BFS uncertainty by both BGS and BPS confirms the expected improvement predicted by our theory and simulations.

6.7 Discussiosn

It is worth noting that this technique can be applied to other existing phase-based BOTDA [113, 139, 151–154] with few modifications. Since the Brillouin gain information can be obtained when extracting the Brillouin phase, the sensing accuracy of all phase-based BOTDA systems can be enhanced by constructing the CBS and applying the CNLS regression. Therefore, this feature reveals a new advantage of the phase-based BOTDA configurations over conventional ones. Meanwhile, benefiting from the mitigation of BFS uncertainty, our complex BOTDA needs fewer measurements than a conventional system under the same SNR requirement. This indicates that the complex BOTDA approach can also reduce the measurement time as well as improve the sensing efficiency.

6.8 Chapter conclusion

In this chapter, we have proposed and demonstrated a novel complex BOTDA approach, which can not only detect the complex Brillouin spectrum, but also use it directly for BFS estimation in the complex domain. We have derived the theoretical equations and

asymptotic closed-form expressions for the BFS uncertainty estimated from CBS, BGS and BPS by nonlinear least squares regression. Both theoretical equations and Monte-Carlo simulation indicate that our complex BOTDA approach can reduce the sensing uncertainty by a factor of $\sqrt{2}$ or the required SNR by 3 dB. We have conducted a distributed temperature sensing experiment in a 40-km SSMF. Experimental results validate the considerable improvement of the sensing accuracy for a long fibre range, comparing with either the gain-based or the phase-based BOTDA approaches. Results in this chapter have been published in [137, 165].

.

Chapter 7
Conclusions

7.1 The summary of this work

7.1.1 Low-DMD few-mode fibre for optical transmission

On the topic of reducing DMD for high-performance optical transmission, we have proposed a distributed grating-assisted few-mode fibre (DG-FMF) to reduce the mean DMD. By introducing asymmetric long-period fibre gratings with random exposure directions in a step-index few-mode fibre during fibre manufacture process, the strong random mode coupling is generated along the entire length of the fibre. Simulation results show that mean DMD in the DG-FMF can be reduced to less than 12 ns at a distance of 100 km with a period of 514 μm and grating strength of 1×10^{-6}. The DMD reduction in our DG-FMF is guaranteed within the entire C-band, and in a wide temperature range from -20°C to $+60^{\circ}$C.

7.1.2 Multi-parameter sensing with few-mode fibres

On the topic of enabling the multi-parameter sensing with few-mode fibres, we have proposed a novel multi-parameter sensing technique based on a Brillouin optical time domain reflectometry in the elliptical-core few-mode fibre, using both the higher order optical and the higher-order acoustic modes. Multiple Brillouin peaks have been observed for the backscattering of both LP_{01} mode and LP_{11} mode. We characterise the temperature and strain coefficients for various optical-acoustic mode pairs. By selecting the proper combination of modes pairs, the performance of multi-parameter sensing can

be optimised. Distributed sensing of temperature and strain is demonstrated, with the error amplification factors of 3.66 °C and 76.6 $\mu\varepsilon$ for temperature and strain, respectively.

7.1.3 Ultra-fast Brillouin fibre sensing technology

On the topic of boosting the measurement time in Brillouin fibre sensors, we have demonstrated a novel single-shot distributed Brillouin optical time domain analyser. In our method, dual-polarisation probe with orthogonal frequency-division multiplexing modulation is used to acquire the distributed Brillouin gain spectra, and coherent detection is used to enhance the signal-to-noise ratio (SNR) drastically. Distributed temperature sensing is demonstrated over a 1.08 km standard single-mode fibre with 20.48 m spatial resolution and 0.59 °C temperature accuracy. Neither frequency scanning, nor polarisation scrambling, nor averaging is required in our scheme. All the data are obtained through only one-shot measurement, indicating that the sensing speed is only limited by the length of fibre.

7.1.4 Complex domain Brillouin Fibre sensors

On the topic of improving the sensing accuracy, we have demonstrated a novel complex Brillouin optical time-domain analysis (BOTDA) approach for distributed fibre sensing that detects the complex Brillouin spectrum. Unlike other approaches, we utilise the complex nonlinear least-square regression technique to determine the Brillouin frequency shift (BFS) directly in the complex domain. The reduction of BFS uncertainty with our approach is shown through theoretical analysis and is validated by both simulations and experiments. Compared with either the gain-based or the phase-based BOTDA approaches, our complex BOTDA can improve the sensing accuracy by a factor of $\sqrt{2}$, which is equivalent to a 3 dB improvement in the power signal-to-noise ratio. Distributed temperature sensing is demonstrated over 40 km standard single-mode fibre. The experimental results agree well with the theoretical predictions of BFS uncertainty that confirms this considerable improvement.

7.2 Future work and perspectives

Spatial-division multiplexing could potentially bring about a bright future for both optical transmission and optical sensing. For the high-performance optical transmission with few-mode fibres, controlling the modal dispersion is still a challenging topic. Though we have proposed a method to reduce the DMD with distributed gratings, the fibre profile and transmission loss can be further optimised. While our improvement has been confirmed by the simulation, the fabrication is still waiting to be finalised in the future. In addition, the perspective of SDM will also depend on the high-performance and cost-effective components, such as low-loss low-DMD low-crosstalk few-mode fibres, high extinction ratio mode multiplexers, equalised high-gain few-mode amplifiers, fast few-mode optical switch and reconfigurable optical add-drop multiplexers (ROADMs). With the development of these key components, SDM technology could be more mature, and the overall system cost could be significantly reduced. Therefore the SDM-based systems could be deployed in the future.

For the optical fibre sensing area, few-mode fibres have shown much improvement, including higher power threshold, better sensing accuracy and more measurable parameters. Even so, the few-mode fibre-based DOFS is still in its early stage. A lot of phenomena and applications are to be further explored. Meanwhile, the influence of other parameters, such as the modal crosstalk, the modal dependent loss and mode control needs to be thoroughly investigated. So the few-mode fibre is a fertile ground for many interest research topics.

For the distributed fibre sensing in single-mode fibre, boosting the sensing time, extending the sensing distance and improving the sensing accuracy are always the main challenges. In this thesis we have proposed the ultra-fast and complex-domain techniques for BOTDA. Nevertheless, these techniques can be further optimised and developed, by reducing the complexity and improving the performance. Though these methods are developed for single-mode fibre sensors, they can be applied in the few-mode fibre sensors as well. With the recent research fever on artificial intelligence, the interdisciplinary of the machine learning and optical fibre sensing could be the next hot topic, which will make the optical fibre sensors more intelligent and autonomous in the future.

Appendix A
Acronyms

AOM	Acoustic-optical modulator
ASE	Amplified spontaneous emission
ASIC	Application-specific integrated circuit
AWG	Arbitrary waveform generator
BFS	Brillouin frequency shift
BOTDA	Brillouin optical time-domain analysis
BOTDR	Brillouin optical time-domain reflectometry
BS	Beam splitter
CW	Continuous wave
DMD	Differential mode delay
DG-FMF	Distributed-grating few-mode fibre
DSB	Double sideband
DSO	Digital storage oscilloscope
DSP	Digital signal processing
DRS	Distributed Raman amplifier
ECL	External cavity laser
EC-FMF	Elliptical-core few-mode fibre
EOM	Electro-optic modulator
FM	Few-mode
FMF	Few-mode fibre
FS	Free-space
FSML	Free-space mode launcher

LO	Local oscillator
LOC	Lobe orientation controller
LP	Linearly polarised
LPF	Low-pass filter
LPG	Long period grating
MIMO	Multiple-input multiple-output
MDMUX	Mode demultiplexer
MMF	Multimode fibre
MMUX	Mode multiplexer
OBPF	Optical bandpass filter
OC	Optical coupler
OFDM	Orthogonal frequency division multiplexing
OOK	On-off keying
PAPR	Peak-to-average power ratio
PC	Polarisation controller
PD	Photodetector
PM	Polarisation-maintaining
QAM	Quadrature amplitude modulation
QPSK	Quadrature phase shift keying
RF	Radio frequency
RI	Refractive index
SBS	Stimulated Brillouin scattering
SDM	Spatial division multiplexing
SMF	Single-mode fibre
SpBS	Spontaneous Brillouin scattering
SpRS	Spontaneous Raman scattering
SSB	Single sideband
SRS	Spontaneous Raman scattering
TMF	Two-mode fibre

Bibliography

[1] Y. Tamura, H. Sakuma, K. Morita, M. Suzuki, Y. Yamamoto, K. Shimada, Y. Honma, K. Sohma, T. Fujii, and T. Hasegawa, "Lowest-ever 0.1419-dB/km loss optical fiber," in *Optical Fiber Communication Conference*, pp. Th5D–1 (Optical Society of America, 2017).

[2] K. Kikuchi, "Fundamentals of coherent optical fiber communications," Journal of Lightwave Technology **34**(1), 157–179 (2016).

[3] J. Cho, X. Chen, S. Chandrasekhar, G. Raybon, R. Dar, L. Schmalen, E. Burrows, A. Adamiecki, S. Corteselli, Y. Pan, D. Correa, B. McKay, S. Zsigmond, P. J. Winzer, and S. Grubb, "Trans-Atlantic Field Trial Using High Spectral Efficiency Probabilistically Shaped 64-QAM and Single-Carrier Real-Time 250-Gb/s 16-QAM," Journal of Lightwave Technology **36**(1), 103–113 (2018).

[4] R. W. Tkach, "Scaling optical communications for the next decade and beyond," Bell Labs Technical Journal **14**(4), 3–10 (2010).

[5] Cisco, "Cisco Visual Networking Index: Forecast and Trends, 2017-2022," Tech. Rep. ID 1543280537836565 (2018).

[6] D. J. Richardson, "Filling the light pipe," Science **330**(6002), 327–328 (2010).

[7] K. Okamoto, "Chapter 7 - Beam propagation method," in *Fundamentals of Optical Waveguides (Second Edition)*, K. Okamoto, ed., pp. 329–397 (Academic Press, Burlington, 2006).

[8] J. ichi Sakai and T. Kimura, "Large-core, broadband optical fiber," Optics Letters **1**(5), 169–171 (1977).

[9] J. Sakai, K. Kitayama, M. Ikeda, Y. Kato, and K. Tatsuya, "Design Considerations of Broadband Dual-Mode Optical Fibers," IEEE Transactions on Microwave Theory and Techniques **26**(9), 658–665 (1978).

[10] H. R. Stuart, "Dispersive multiplexing in multimode optical fiber," Science **289**(5477), 281–283 (2000).

[11] D. Soma, Y. Wakayama, S. Beppu, S. Sumita, T. Tsuritani, T. Hayashi, T. Nagashima, M. Suzuki, M. Yoshida, K. Kasai, M. Nakazawa, H. Takahashi, K. Igarashi, I. Morita, and M. Suzuki, "10.16-Peta-B/s Dense SDM/WDM Transmission Over 6-Mode 19-Core Fiber Across the C+L Band," Journal of Lightwave Technology **36**(6), 1362–1368 (2018).

[12] B. Culshaw and A. Kersey, "Fiber-Optic Sensing : A Historical Perspective," Journal of Lightwave Technology **26**(9), 1064–1078 (2008).

[13] P. Xu, Y. Dong, D. Zhou, C. Fu, J. Zhang, H. Zhang, Z. Lu, L. Chen, and X. Bao, "1200°C high-temperature distributed optical fiber sensing using Brillouin optical time domain analysis," Applied Optics **55**(21), 5471–5478 (2016).

[14] S. Berdagué and P. Facq, "Mode division multiplexing in optical fibers," Applied Optics **21**(11), 1950–1955 (1982).

[15] A. Li, A. Al Amin, X. Chen, and W. Shieh, "Transmission of 107-Gb/s mode and polarization multiplexed CO-OFDM signal over a two-mode fiber." Optics Express **19**, 8808–8814 (2011).

[16] R. Ryf, S. Randel, A. H. Gnauck, C. Bolle, R.-J. Essiambre, P. Winzer, D. W. Peckham, A. McCurdy, and R. Lingle, "Space-division multiplexing over 10 km of three-mode fiber using coherent 6×6 MIMO processing," in *Optical Fiber Communication Conference/National Fiber Optic Engineers Conference 2011*, p. PDPB10 (Optical Society of America, 2011).

[17] E. Ip, N. Bai, Y. K. Huang, E. Mateo, F. Yaman, M. J. Li, S. Bickham, S. Ten, J. L. nares, C. Montero, V. Moreno, X. Prieto, V. Tse, K. M. Chung, A. Lau, H. Y. Tam, C. Lu, Y. Luo, G. D. Peng, and G. Li, "88×3×112-Gb/s WDM Transmission over 50 km of Three-Mode Fiber with Inline Few Mode Fiber Amplifier," in *37th European Conference and Exposition on Optical Communications*, p. Th.13.C.2 (Optical Society of America, 2011).

[18] A. Tarighat, R. C. J. Hsu, A. Shah, A. H. Sayed, and B. Jalali, "Fundamentals and challenges of optical multiple-input multiple-output multimode fiber links," IEEE Communications Magazine **45**(5), 57–63 (2007).

[19] T. Mori, T. Sakamoto, T. Yamamoto, and S. Tomita, "Coherent optical MIMO transmission over 20 km GI multi-mode fiber by using digital coherent receiver with mode convergence unit," Optics Express **19**(17), 16,252 (2011).

[20] A. W. Snyder and J. Love, *Optical waveguide theory* (Springer Science & Business Media, 2012).

[21] K. Okamoto, "Chapter 3 - Optical fibers," in *Fundamentals of Optical Waveguides (Second Edition)*, K. Okamoto, ed., pp. 57–158 (Academic Press, Burlington, 2006).

[22] S. Randel, R. Ryf, A. Sierra, P. J. Winzer, A. H. Gnauck, C. A. Bolle, R.-J. Essiambre, D. W. Peckham, A. McCurdy, and R. Lingle, "6×56-Gb/s mode-division multiplexed transmission over 33-km few-mode fiber enabled by 6×6 MIMO equalization," Optics Express **19**(17), 16,697–16,707 (2011).

[23] A. Li, A. A. Amin, X. Chen, and W. Shieh, "Transmission of 107-Gb/s mode and polarization multiplexed CO-OFDM signal over a two-mode fiber," Optics Express **19**(9), 8808–8814 (2011).

[24] S. Randel, R. Ryf, A. Gnauck, M. A. Mestre, C. Schmidt, R. Essiambre, P. Winzer, R. Delbue, P. Pupalaikis, A. Sureka, Y. Sun, X. Jiang, and R. Lingle, "Mode-Multiplexed 6×20-GBd QPSK Transmission over 1200-km DGD-Compensated Few-Mode Fiber," in *Optical Fiber Communication Conference*, p. PDP5C.5 (Optical Society of America, 2012).

[25] R. Ryf, N. K. Fontaine, M. A. Mestre, S. Randel, X. Palou, C. Bolle, A. H. Gnauck, S. Chandrasekhar, X. Liu, B. Guan, R.-J. Essiambre, P. J. Winzer, S. Leon-Saval, J. Bland-Hawthorn, R. Delbue, P. Pupalaikis, A. Sureka, Y. Sun, L. Grüner-Nielsen, R. V. Jensen, and R. Lingle, "12×12 MIMO Transmission over 130-km Few-Mode Fiber," in *Frontiers in Optics 2012/Laser Science XXVIII*, p. FW6C.4 (Optical Society of America, Rochester, New York, 2012).

[26] A. Al Amin, A. Li, S. Chen, X. Chen, G. Gao, and W. Shieh, "Dual-LP_{11} mode 4×4 MIMO-OFDM transmission over a two-mode fiber," Optics Express **19**(17), 16,672–16,679 (2011).

[27] M. Salsi, C. Koebele, D. Sperti, P. Tran, P. Brindel, H. Mardoyan, S. Bigo, A. Boutin, F. Verluise, P. Sillard, M. Astruc, L. Provost, F. Cerou, and G. Charlet, "Transmission at 2×100Gb/s, over Two Modes of 40km-long Prototype Few-Mode Fiber, using LCOS-based Mode Multiplexer and Demultiplexer," in *Optical Fiber Communication Conference/National Fiber Optic Engineers Conference 2011*, p. PDPB9 (Optical Society of America, 2011).

[28] T. A. Birks, I. Gris-Sánchez, S. Yerolatsitis, S. G. Leon-Saval, and R. R. Thomson, "The photonic lantern," Advances in Optics and Photonics **7**(2), 107–167 (2015).

[29] S. G. Leon-Saval, N. K. Fontaine, J. R. Salazar-Gil, B. Ercan, R. Ryf, and J. Bland-Hawthorn, "Mode-selective photonic lanterns for space-division multiplexing," Optics Express **22**(1), 1036–1044 (2014).

[30] B. Huang, N. K. Fontaine, R. Ryf, B. Guan, S. G. Leon-Saval, R. Shubochkin, Y. Sun, R. Lingle, and G. Li, "All-fiber mode-group-selective photonic lantern using graded-index multimode fibers," Optics Express **23**(1), 224–234 (2015).

[31] S. H. Chang, H. S. Chung, N. K. Fontaine, R. Ryf, K. J. Park, K. Kim, J. C. Lee, J. H. Lee, B. Y. Kim, and Y. K. Kim, "Mode division multiplexed optical transmission enabled by all–fiber mode multiplexer," Optics Express **22**(12), 14,229–14,236 (2014).

[32] S. H. Chang, H. S. Chung, R. Ryf, N. K. Fontaine, C. Han, K. J. Park, K. Kim, J. C. Lee, J. H. Lee, B. Y. Kim, and Y. K. Kim, "Mode- and wavelength-division multiplexed transmission using all-fiber mode multiplexer based on mode selective couplers," Optics Express **23**(6), 7164–7172 (2015).

[33] M. J. Li, B. Hoover, S. Li, S. Bickham, S. Ten, E. Ip, Y. K. Huang, E. Mateo, Y. Shao, and T. Wang, "Low delay and large effective area few-mode fibers for mode-division multiplexing," in *Technical Digest - 2012 17th Opto-Electronics and Communications Conference, OECC 2012*, pp. 495–496 (2012).

[34] A. Li, X. Chen, and W. Shieh, "Nonlinear tolerance of few-mode fiber based transmission systems with random mode coupling," in *2013 Optical Fiber Communication Conference and Exposition and the National Fiber Optic Engineers Conference (OFC/NFOEC)*, pp. 1–3 (2013).

[35] K. J. Park, K. Y. Song, Y. K. Kim, and B. Y. Kim, "All-Fiber Mode Division Multiplexer optimized for C-band," in *Optical Fiber Communication Conference*, p. M3K.2 (Optical Society of America, 2014).

[36] L. Bigot, G. Le Cocq, and Y. Quiquempois, "Few-mode erbium-doped fiber amplifiers: A review," Journal of Lightwave Technology **33**(3), 588–596 (2015).

[37] G. L. Cocq, L. Bigot, A. L. Rouge, M. Bigot-Astruc, P. Sillard, C. Koebele, M. Salsi, and Y. Quiquempois, "Modeling and characterization of a few-mode EDFA supporting four mode groups for mode division multiplexing," Optics Express **20**(24), 27,051–27,061 (2012).

[38] Y. Jung, Q. Kang, V. A. J. M. Sleiffer, B. Inan, M. Kuschnerov, V. Veljanovski, B. Corbett, R. Winfield, Z. Li, P. S. Teh, A. Dhar, J. Sahu, F. Poletti, S. U. Alam, and D. J. Richardson, "Three mode Er^{3+} ring-doped fiber amplifier for mode-division multiplexed transmission," Optics Express **21**(8), 10,383–10,392 (2013).

[39] E. Ip, M. J. Li, K. Bennett, Y. K. Huang, A. Tanaka, A. Korolev, K. Koreshkov, W. Wood, E. Mateo, J. Hu, and Y. Yano, "146$\lambda\times$6$\times$19-Gbaud wavelength-and

mode-division multiplexed transmission over 10×50-km spans of few-mode fiber with a gain-equalized few-mode EDFA," Journal of Lightwave Technology **32**(4), 790–797 (2014).

[40] P. Genevaux, C. Simonneau, G. L. Cocq, Y. Quiquempois, L. Bigot, J.-F. Morizur, and G. Charlet, "Amplification of 5 modes carrying each 100Gb/s with a few mode EDFA," in *Optical Fiber Communication Conference*, p. Tu3C.5 (Optical Society of America, 2015).

[41] R. Ryf, A. Sierra, R.-J. Essiambre, S. Randel, A. H. Gnauck, C. Bolle, M. Esmaeelpour, P. J. Winzer, R. Delbue, P. Pupalaikise, A. Sureka, D. W. Peckham, A. McCurdy, and R. Lingle, "Mode-Equalized Distributed Raman Amplification in 137-km Few-Mode Fiber," in *37th European Conference and Exposition on Optical Communications*, p. Th.13.K.5 (Optical Society of America, 2011).

[42] J. Zhou, "An analytical approach for gain optimization in multimode fiber Raman amplifiers," Optics Express **22**(18), 21,393–21,402 (2014).

[43] G. Rademacher, R. Ryf, N. K. Fontaine, H. Chen, R. J. Essiambre, B. J. Puttnam, R. S. Luís, Y. Awaji, N. Wada, S. Gross, N. Riesen, M. Withford, Y. Sun, and R. Lingle, "Long-Haul Transmission over Few-Mode Fibers with Space-Division Multiplexing," Journal of Lightwave Technology **36**(6), 1382–1388 (2018).

[44] Y. Wakayama, D. Soma, S. Beppu, S. Sumita, K. Igarashi, and T. Tsuritani, "266.1-Tbit/s Repeatered Transmission over 90.4-km 6-Mode Fiber Using Dual C+L-Band 6-Mode EDFA," in *Optical Fiber Communication Conference*, p. W4C.1 (Optical Society of America, 2018).

[45] R. Ryf, S. Randel, A. H. Gnauck, C. Bolle, A. Sierra, S. Mumtaz, M. Esmaeelpour, E. C. Burrows, R. J. Essiambre, P. J. Winzer, D. W. Peckham, A. H. McCurdy, and R. Lingle, "Mode-division multiplexing over 96 km of few-mode fiber using coherent 6×6 MIMO processing," Journal of Lightwave Technology **30**(4), 521–531 (2012).

[46] E. Ip, N. Bai, Y.-K. Huang, E. Mateo, F. Yaman, M.-J. Li, S. Bickham, S. Ten, Y. Luo, G.-D. Peng, G. Li, T. Wang, J. Linares, C. Montero, and V. Moreno, "6×6 MIMO Transmission over 50+25+10 km Heterogeneous Spans of Few-Mode Fiber with Inline Erbium-Doped Fiber Amplifier," in *Optical Fiber Communication Conference*, p. OTu2C.4 (Optical Society of America, Los Angeles, California, 2012).

[47] R. Ryf, M. A. Mestre, S. Randel, C. Schmidt, A. H. Gnauck, R. J. Essiambre, P. J. Winzer, R. Delbue, P. Pupalaikis, A. Sureka, Y. Sun, X. Jiang, D. W. Peckham, A. McCurdy, and R. Lingle, "Mode-multiplexed transmission over a 209-km DGD-compensated hybrid few-mode fiber span," IEEE Photonics Technology Letters **24**(21), 1965–1968 (2012).

[48] V. Sleiffer, Y. Jung, V. Veljanovski, R. van Uden, M. Kuschnerov, H. Chen, B. Inan, L. G. Nielsen, Y. Sun, D. Richardson, S. Alam, F. Poletti, J. Sahu, A. Dhar, A. Koonen, B. Corbett, R. Winfield, A. Ellis, and H. de Waardt, "737 Tb/s (96×3×256-Gb/s) mode-division-multiplexed DP-16QAM transmission with inline MM-EDFA," Optics Express **20**(26), B428–B438 (2012).

[49] R. Ryf, S. Randel, N. K. Fontaine, M. Montoliu, E. Burrows, S. Chandrasekhar, A. H. Gnauck, C. Xie, R.-J. Essiambre, P. Winzer, R. Delbue, P. Pupalaikis, A. Sureka, Y. Sun, L. Gruner-Nielsen, R. V. Jensen, and R. Lingle, "32-bit/s/Hz Spectral Efficiency WDM Transmission over 177-km Few-Mode Fiber," in *Optical Fiber Communication Conference/National Fiber Optic Engineers Conference 2013*, p. PDP5A.1 (Optical Society of America, Anaheim, California, 2013).

[50] R. Ryf, N. K. Fontaine, H. Chen, B. Guan, S. Randel, N. Sauer, S. Yoo, A. Koonen, R. Delbue, P. Pupalaikis, A. Sureka, R. Shubochkin, Y. Sun, and R. Lingle, "23 Tbit/s Transmission over 17-km Conventional 50 μm Graded-Index Multimode Fiber," in *Optical Fiber Communication Conference: Postdeadline Papers*, p. Th5B.1 (Optical Society of America, 2014).

[51] N. Cvijetic, E. Ip, N. Prasad, M.-J. Li, and T. Wang, "Experimental Time and Frequency Domain MIMO Channel Matrix Characterization versus Distance for

6×28Gbaud QPSK Transmission over 40×25km Few Mode Fiber," in *Optical Fiber Communication Conference*, p. Th1J.3 (Optical Society of America, 2014).

[52] N. K. Fontaine, R. Ryf, H. Chen, A. V. Benitez, J. E. A. Lopez, R. A. Correa, B. Guan, B. Ercan, R. P. Scott, S. J. B. Yoo, L. Grüner-Nielsen, Y. Sun, and R. J. Lingle, "30×30 MIMO Transmission over 15 Spatial Modes," in *Optical Fiber Communication Conference Post Deadline Papers*, p. Th5C.1 (Optical Society of America, 2015).

[53] Y. Chen, A. Lobato, Y. Jung, H. Chen, V. A. Sleiffer, M. Kuschnerov, N. K. Fontaine, R. Ryf, D. J. Richardson, B. Lankl, and N. Hanik, "41.6 Tbit/s C-band SDM OFDM transmission through 12 spatial and polarization modes over 74.17 km few mode fiber," Journal of Lightwave Technology **33**(7), 1440–1444 (2015).

[54] E. Ip, G. Milione, M.-J. Li, N. Cvijetic, K. Kanonakis, J. Stone, G. Peng, X. Prieto, C. Montero, V. Moreno, and J. Liñares, "SDM transmission of real-time 10GbE traffic using commercial SFP + transceivers over 0.5km elliptical-core few-mode fiber," Optics Express **23**(13), 17,120 (2015).

[55] M. Esmaeelpour, R. Ryf, N. K. Fontaine, H. Chen, A. H. Gnauck, R. J. Essiambre, J. Toulouse, Y. Sun, and R. Lingle, "Transmission over 1050-km few-mode fiber based on bidirectional distributed raman amplification," Journal of Lightwave Technology **34**(8), 1864–1871 (2016).

[56] H. Liu, H. Wen, J. C. A. Zacarias, J. E. Antonio-Lopez, N. Wang, P. Sillard, A. A. Correa, R. Amezcua-Correa, and G. Li, "3×10 Gb/s mode group-multiplexed transmission over a 20 km few-mode fiber using photonic lanterns," in *Optical Fiber Communication Conference*, p. M2D.5 (Optical Society of America, 2017).

[57] F. Parmigiani, Y. Jung, L. Gruner-Nielsen, T. Geisler, P. Petropoulos, and D. J. Richardson, "Elliptical Core Few Mode Fibers for Multiple-Input Multiple Output-Free Space Division Multiplexing Transmission," IEEE Photonics Technology Letters **29**(21), 1764–1767 (2017).

[58] J. Li, L. Wang, J. Du, Z. He, C. Cai, L. Zhu, A. Wang, and J. Wang, "C + L band distributed few-mode Raman amplification with flattened gain for mode-division-

multiplexed optical transmission over 75-km Few-mode fiber," in *Optical Fiber Communication Conference*, p. W3D.2 (Optical Society of America, 2018).

[59] G. Rademacher, R. S. Luís, B. J. Puttnam, R. Ryf, H. Furukawa, R. Maruyama, K. Aikawa, A. Maruta, Y. Awaji, and N. Wada, "93.34 Tbit/s/mode (280 Tbit/s) Transmission in a 3-Mode Graded-Index Few-Mode Fiber," in *Optical Fiber Communication Conference*, p. W4C.3 (Optical Society of America, 2018).

[60] G. Rademacher, R. S. Luís, B. J. Puttnam, T. A. Eriksson, E. Agrell, R. Maruyama, K. Aikawa, H. Furukawa, Y. Awaji, and N. Wada, "159 Tbit/s C+L Band Transmission over 1045 km 3-Mode Graded-Index Few-Mode Fiber," in *Optical Fiber Communication Conference Postdeadline Papers*, p. Th4C.4 (Optical Society of America, 2018).

[61] G. Agrawa, *Nonlinear Fiber Optics* (Academic press, 2006).

[62] K.-P. Ho and J. M. Kahn, "Statistics of Group Delays in Multimode Fiber With Strong Mode Coupling," Journal of Lightwave Technology **29**(21), 3119–3128 (2011).

[63] S. O. Arik, D. Askarov, and J. M. Kahn, "Effect of mode coupling on signal processing complexity in mode-division multiplexing," Journal of Lightwave Technology **31**(3), 423–431 (2013).

[64] S. J. Savory, "Digital filters for coherent optical receivers," Optics Express **16**(2), 804–817 (2008).

[65] S. O. Arik, D. Askarov, and J. M. Kahn, "Adaptive frequency-domain equalization in mode-division multiplexing systems," Journal of Lightwave Technology **32**(10), 1841–1852 (2014).

[66] T. Sakamoto, T. Mori, T. Yamamoto, and S. Tomita, "Differential Mode Delay Managed Transmission Line for WDM-MIMO System Using Multi-Step Index Fiber," Journal of Lightwave Technology **30**(17), 2783–2787 (2012).

[67] P. Sillard, D. Molin, M. Bigot-Astruc, K. De Jongh, F. Achten, A. M. Velazquez-Benitez, R. Amezcua-Correa, and C. M. Okonkwo, "Low-Differential-Mode-Group-Delay 9-LP-Mode Fiber," Journal of Lightwave Technology **34**(2), 425–430 (2016).

[68] L. Grüner-Nielsen, Y. Sun, J. W. Nicholson, D. Jakobsen, K. G. Jespersen, R. Lingle, and B. Pálsdóttir, "Few mode transmission fiber with low DGD, low mode coupling, and low loss," Journal of Lightwave Technology **30**(23), 3693–3698 (2012).

[69] P. Sillard, "Scalability of few-mode fibers for mode-division-multiplexed systems," in *2014 IEEE Photonics Conference*, pp. 520–521 (2014).

[70] G. Rademacher, S. Warm, and K. Petermann, "Nonlinear interaction in differential mode delay managed mode-division multiplexed transmission systems," Optics Express **23**(1), 55–60 (2015).

[71] S. O. Arik, D. Askarov, and J. M. Kahn, "MIMO DSP Complexity in Mode-Division Multiplexing," in *Optical Fiber Communication Conference*, p. Th1D.1 (Optical Society of America, 2015).

[72] G. Li, N. Bai, N. Zhao, and C. Xia, "Space-division multiplexing: the next frontier in optical communication," Advances in Optics and Photonics **6**(4), 413–487 (2014).

[73] D. A. Nolan, X. Chen, and M. J. Li, "Fibers with low polarization-mode dispersion," Journal of Lightwave Technology **22**(4), 1066–1077 (2004).

[74] L. Palmieri, "Modal Dispersion Properties of Few-Mode Spun Fibers," in *Optical Fiber Communication Conference*, p. Tu2D.4 (Optical Society of America, 2015).

[75] K. P. Ho and W. Shieh, "Equalization-enhanced phase noise in mode-division multiplexed systems," Journal of Lightwave Technology **31**(13), 2237–2243 (2013).

[76] G. Bolognini and A. Hartog, "Raman-based fibre sensors: Trends and applications," Optical Fiber Technology **19**(6 Part B), 678–688 (2013).

[77] P. Rajeev, J. Kodikara, W. K. Chiu, and T. Kuen, "Distributed Optical Fibre Sensors and their Applications in Pipeline Monitoring," in *Structural Health Monitoring: Research and Applications*, vol. 558 of *Key Engineering Materials*, pp. 424–434 (Trans Tech Publications, 2013).

[78] M. A. Soto, T. Nannipieri, A. Signorini, A. Lazzeri, F. Baronti, R. Roncella, G. Bolognini, and F. Di Pasquale, "Raman-based distributed temperature sensor with 1m spatial resolution over 26km SMF using low-repetition-rate cyclic pulse coding," Optics Letters **36**(13), 2557–2559 (2011).

[79] M. A. Soto, T. Nannipieri, A. Signorini, G. Bolognini, F. D. Pasquale, A. Lazzeri, F. Baronti, and R. Roncella, "Advanced cyclic coding technique for long-range Raman DTS systems with meter-scale spatial resolution over standard SMF," in *SENSORS, 2011 IEEE*, pp. 878–881 (2011).

[80] M. Wang, H. Wu, M. Tang, Z. Zhao, Y. Dang, C. Zhao, R. Liao, W. Chen, S. Fu, C. Yang, W. Tong, P. P. Shum, and D. Liu, "Few-mode fiber based Raman distributed temperature sensing," Optics Express **25**(5), 4907–4916 (2017).

[81] Y. Liu, L. Ma, C. Yang, W. Tong, and Z. He, "Long-range Raman distributed temperature sensor with high spatial and temperature resolution using graded-index few-mode fiber," Optics Express **26**(16), 20,562–20,571 (2018).

[82] F. Chen, G. M. Brown, and N. Song, "Overview of 3-D shape measurement using optical methods," Optical Engineering **39**(1), 10–22 (2000).

[83] O. Frazão, R. Falate, J. L. Fabris, J. L. Santos, L. a. Ferreira, and F. M. Araújo, "Optical inclinometer based on a single long-period fiber grating combined with a fused taper," Optics Letters **31**(20), 2960–2962 (2006).

[84] X. Chen, C. Zhang, D. J. Webb, K. Kalli, and G. D. Peng, "Highly sensitive bend sensor based on bragg grating in eccentric core polymer fiber," IEEE Photonics Technology Letters **22**(11), 850–852 (2010).

[85] P. Li, Z. Yan, K. Zhou, L. Zhang, and J. Leng, "Monitoring static shape memory polymers using a fiber Bragg grating as a vector-bending sensor," Optical Engineering **52**(1), 014,401 (2013).

[86] Z. Ou, Y. Yu, P. Yan, J. Wang, Q. Huang, X. Chen, C. Du, and H. Wei, "Ambient refractive index-independent bending vector sensor based on seven-core photonic crystal fiber using lateral offset splicing," Optics Express **21**(20), 23,812–23,821 (2013).

[87] H. Wu, R. Wang, D. Liu, S. Fu, C. Zhao, H. Wei, W. Tong, P. P. Shum, and M. Tang, "Few-mode fiber based distributed curvature sensor through quasi-single-mode Brillouin frequency shift," Optics Letters **41**(7), 1514–1517 (2016).

[88] H. Wu, M. Tang, M. Wang, C. Zhao, Z. Zhao, R. Wang, R. Liao, S. Fu, C. Yang, W. Tong, P. P. Shum, and D. Liu, "Few-mode optical fiber based simultaneously distributed curvature and temperature sensing," Optics Express **25**(11), 12,722–12,732 (2017).

[89] M. N. Alahbabi, Y. T. Cho, and T. P. Newson, "Simultaneous temperature and strain measurement with combined spontaneous Raman and Brillouin scattering," Optics Letters **30**(11), 1276–1278 (2005).

[90] T. R. Parker, M. Farhadiroushan, V. A. Handerek, and A. J. Rogers, "A fully distributed simultaneous strain and temperature sensor using spontaneous Brillouin backscatter," IEEE Photonics Technology Letters **9**(7), 979–981 (1997).

[91] S. M. Maughan, H. H. Kee, and T. P. Newson, "Simultaneous distributed fibre temperature and strain sensor using microwave coherent detection of spontaneous Brillouin backscatter," Measurement Science and Technology **12**(7), 834–842 (2001).

[92] Q. Yu, X. Bao, and L. Chen, "Strain dependence of Brillouin frequency, intensity, and bandwidth in polarization-maintaining fibers," Optics Letters **29**(14), 1605–1607 (2004).

[93] W. Zou, Z. He, and K. Hotate, "Complete discrimination of strain and temperature using Brillouin frequency shift and birefringence in a polarization-maintaining fiber," Optics Express **17**(3), 1248–1255 (2009).

[94] L. Zou, X. Bao, S. Afshar V., and L. Chen, "Dependence of the Brillouin frequency shift on strain and temperature in a photonic crystal fiber," Optics Letters **29**(13), 1485–1487 (2004).

[95] X. Liu and X. Bao, "Brillouin spectrum in LEAF and simultaneous temperature and strain measurement," Journal of Lightwave Technology **30**(8), 1053–1059 (2012).

[96] Y. Xu, M. Ren, Y. Lu, P. Lu, P. Lu, X. Bao, L. Wang, Y. Messaddeq, and S. LaRochelle, "Multi-parameter sensor based on stimulated Brillouin scattering in inverse-parabolic graded-index fiber," Optics Letters **41**(6), 1138–1141 (2016).

[97] Y. Dong, G. Ren, H. Xiao, Y. Gao, H. Li, S. Xiao, and S. Jian, "Simultaneous Temperature and Strain Sensing Based on M-Shaped Single Mode Fiber," IEEE Photonics Technology Letters **29**(22), 1955–1958 (2017).

[98] A. Li, Y. Wang, J. Fang, M.-J. Li, B. Y. Kim, and W. Shieh, "Few-mode fiber multi-parameter sensor with distributed temperature and strain discrimination," Optics Letters **40**(7), 1488–1491 (2015).

[99] Y. Weng, E. Ip, Z. Pan, and T. Wang, "Distributed Temperature and Strain Sensing using Spontaneous Brillouin Scattering in Optical Few-Mode Fibers," in *CLEO: 2015*, p. SM2O.5 (Optical Society of America, 2015).

[100] Y. Weng, E. Ip, Z. Pan, and T. Wang, "Single-end simultaneous temperature and strain sensing techniques based on Brillouin optical time domain reflectometry in few-mode fibers," Optics Express **23**(7), 9024–9039 (2015).

[101] Y. H. Kim and K. Y. Song, "Optical time-domain reflectometry based on a Brillouin dynamic grating in an elliptical-core two-mode fiber," Optics Letters **42**(15), 3036–3039 (2017).

[102] M. A. Soto and L. Thévenaz, "Advanced Pulse Coding Techniques for Distributed Optical Fiber Sensors," in *Frontiers in Optics 2013*, p. FW4I.3 (Optical Society of America, 2013).

[103] J. Park, G. Bolognini, D. Lee, P. Kim, P. Cho, F. Di Pasquale, and N. Park, "Raman-based distributed temperature sensor with simplex coding and link optimization," IEEE Photonics Technology Letters **18**(17), 1879–1881 (2006).

[104] M. A. Soto, G. Bolognini, and F. Di Pasquale, "Analysis of optical pulse coding in spontaneous Brillouin-based distributed temperature sensors," Optics Express **16**(23), 19,097–19,111 (2008).

[105] M. A. Soto, G. Bolognini, F. Di Pasquale, and L. Thévenaz, "Simplex-coded BOTDA fiber sensor with 1 m spatial resolution over a 50 km range," Optics Letters **35**(2), 259–261 (2010).

[106] Y. Muanenda, M. Taki, and F. D. Pasquale, "Long-range accelerated BOTDA sensor using adaptive linear prediction and cyclic coding," Optics Letters **39**(18), 5411–5414 (2014).

[107] H. Iribas, A. Loayssa, F. Sauser, M. Llera, and S. L. Floch, "Brillouin optical time-domain analyzer for extended sensing range using probe dithering and cyclic coding," in *2017 25th Optical Fiber Sensors Conference (OFS)*, pp. 1–4 (2017).

[108] Y. Muanenda, C. J. Oton, S. Faralli, and F. D. Pasquale, "A Cost-Effective Distributed Acoustic Sensor Using a Commercial Off-the-Shelf DFB Laser and Direct Detection Phase-OTDR," IEEE Photonics Journal **8**(1), 1–10 (2016).

[109] Y. Muanenda, M. Taki, T. Nannipieri, A. Signorini, C. J. Oton, F. Zaidi, I. Toccafondo, and F. D. Pasquale, "Advanced Coding Techniques for Long-Range Raman / BOTDA Distributed Strain and Temperature Measurements," Journal of Lightwave Technology **34**(2), 342–350 (2016).

[110] G. Daniel, B. Vazquez, O. E. Martínez, and D. Kunik, "Distributed Temperature Sensing Using Cyclic Pseudorandom Sequences," IEEE Sensors Journal **17**(6), 1686–1691 (2017).

[111] A. Masoudi and T. P. Newson, "Contributed Review: Distributed optical fibre dynamic strain sensing," Review of Scientific Instruments **87**(1), 11,501 (2016).

[112] Y. Peled, A. Motil, L. Yaron, and M. Tur, "Slope-assisted fast distributed sensing in optical fibers with arbitrary Brillouin profile," Optics Express **19**(21), 19,845–19,854 (2011).

[113] D. Zhou, Y. Dong, B. Wang, T. Jiang, D. Ba, P. Xu, H. Zhang, Z. Lu, and H. Li, "Slope-assisted BOTDA based on vector SBS and frequency-agile technique for wide-strain-range dynamic measurements," Optics Express **25**(3), 1889–1902 (2017).

[114] Y. Peled, A. Motil, and M. Tur, "Fast Brillouin optical time domain analysis for dynamic sensing," Optics Express **20**(8), 8584–8591 (2012).

[115] A. Voskoboinik, O. F. Yilmaz, A. W. Willner, and M. Tur, "Sweep-free distributed Brillouin time-domain analyzer (SF-BOTDA)," Optics Express **19**(26), B842–B847 (2011).

[116] C. Jin, N. Guo, Y. Feng, L. Wang, H. Liang, J. Li, Z. Li, C. Yu, and C. Lu, "Scanning-free BOTDA based on ultra-fine digital optical frequency comb," Optics Express **23**(4), 5277–5287 (2015).

[117] A. K. Azad, L. Wang, N. Guo, H.-Y. Tam, and C. Lu, "Signal processing using artificial neural network for BOTDA sensor system," Optics Express **24**(6), 6769–6782 (2016).

[118] H. Wu, L. Wang, N. Guo, C. Shu, and C. Lu, "Brillouin Optical Time-Domain Analyzer Assisted by Support Vector Machine for Ultrafast Temperature Extraction," Journal of Lightwave Technology **35**(19), 4159–4167 (2017).

[119] B. Wang, L. Wang, C. Yu, and C. Lu, "Simultaneous Temperature and Strain Measurement Using Deep Neural Networks for BOTDA Sensing System," in *Optical Fiber Communication Conference*, p. Th2A.66 (Optical Society of America, 2018).

[120] R. Ruiz-Lombera, A. Fuentes, L. Rodriguez-Cobo, J. M. Lopez-Higuera, and J. Mirapeix, "Simultaneous Temperature and Strain Discrimination in a Conventional BOTDA via Artificial Neural Networks," Journal of Lightwave Technology **36**(11), 2114–2121 (2018).

[121] W.-P. Huang, "Coupled-mode theory for optical waveguides: an overview," Journal of the Optical Society of America A **11**(3), 963–983 (1994).

[122] J. F. Brennan III and D. L. LaBrake, "Long-length continuous phase Bragg reflectors in optical media," (2002). US Patent 6,404,956.

[123] A. M. Vengsarkar, P. J. Lemaire, J. B. Judkins, V. Bhatia, T. Erdogan, and J. E. Sipe, "Long-period fiber gratings as band-rejection filters," Journal of Lightwave Technology **14**(1), 58–64 (1996).

[124] M. B. Shemirani, W. Mao, R. A. Panicker, and J. Kahn, "Principal Modes in Graded-Index Multimode Fiber in Presence of Spatial- and Polarization-Mode Coupling," Journal of Lightwave Technology **27**(10), 1248–1261 (2009).

[125] N. H. Ky, H. G. Limberger, R. P. Salathé, and F. Cochet, "Efficient broadband intracore grating LP01–LP02 mode converters for chromatic-dispersion compensation," Optics Letters **23**(6), 445–447 (1998).

[126] T. Erdogan, "Fiber grating spectra," Journal of Lightwave Technology **15**(8), 1277–1294 (1997).

[127] G. Ghosh, M. Endo, and T. Iwasaki, "Temperature-Dependent sellmeier Coefficients and Chromatic Dispersions for Some Optical fiber glasses," Journal of Lightwave Technology **12**(8), 1338–1342 (1994).

[128] Y.-J. Kim, U.-C. Paek, and B. H. Lee, "Measurement of refractive-index variation with temperature by use of long-period fiber gratings," Optics Letters **27**(15), 1297–1299 (2002).

[129] C. C. Ye, S. W. James, and R. P. Tatam, "Simultaneous temperature and bend sensing with long-period fiber gratings." Optics Letters **25**(14), 1007–1009 (2000).

[130] J. Fang, A. Li, and W. Shieh, "Low-DMD few-mode fiber with distributed long-period grating," Optics Letters **40**(17), 3937–3940 (2015).

[131] K. Y. Song, Y. H. Kim, and B. Y. Kim, "Intermodal stimulated Brillouin scattering in two-mode fibers," Optics Letters **38**(11), 1805–1807 (2013).

[132] A. Motil, A. Bergman, and M. Tur, "[INVITED] State of the art of Brillouin fiber-optic distributed sensing," Optics and Laser Technology **78**, 81–103 (2016).

[133] A. Li, Y. Wang, Q. Hu, and W. Shieh, "Few-mode fiber based optical sensors," Optics Express **23**(2), 1139–1150 (2015).

[134] W. Jin, "Simultaneous measurement of strain and temperature: error analysis," Optical Engineering **36**(2), 598–610 (1997).

[135] H. H. Kee, G. P. Lees, and T. P. Newson, "All-fiber system for simultaneous interrogation of distributed strain and temperature sensing by spontaneous Brillouin scattering," Optics Letters **25**(10), 695–697 (2000).

[136] M. A. Soto and L. Thévenaz, "Modeling and evaluating the performance of Brillouin distributed optical fiber sensors," Optics Express **21**(25), 31,347–31,366 (2013).

[137] J. Fang, M. Sun, D. Che, M. Myers, H. Bao, C. Prohasky, and W. Shieh, "Complex Brillouin Optical Time-Domain Analysis," Journal of Lightwave Technology **36**(10), 1840–1850 (2018).

[138] J. Fang, G. Milione, J. Stone, G. Peng, M.-J. Li, E. Ip, Y. Li, Y.-K. Huang, P. N. Ji, M.-F. Huang, S. Murakami, W. Shieh, and T. Wang, "Distributed Temperature and

Strain Sensing Using Brillouin Optical Time-Domain Reflectometry Over a Few-Mode Elliptical-Core Optical Fiber," in *26th International Conference on Optical Fiber Sensors*, p. TuD1 (Optical Society of America, 2018).

[139] J. Urricelqui, M. Sagues, and A. Loayssa, "BOTDA measurements tolerant to non-local effects by using a phase-modulated probe wave and RF demodulation," Optics Express **21**(14), 17,186–17,194 (2013).

[140] W. Shieh, H. Bao, and Y. Tang, "Coherent optical OFDM: theory and design," Optics Express **16**(2), 841–859 (2008).

[141] W. Shieh and I. Djordjevic, *OFDM for optical communications* (Academic Press, 2009).

[142] J. Urricelqui, M. A. Soto, and L. Thévenaz, "Sources of noise in Brillouin optical time-domain analyzers," in *24th International Conference on Optical Fibre Sensors (OFS)*, vol. 9634, p. 963434 (2015).

[143] M. van Deventer and A. Boot, "Polarization properties of stimulated Brillouin scattering in single-mode fibers," Journal of Lightwave Technology **12**(4), 585–590 (1994).

[144] A. Lopez-Gil, M. A. Soto, X. Angulo-Vinuesa, A. Dominguez-Lopez, S. Martin-Lopez, L. Thévenaz, and M. Gonzalez-Herraez, "Evaluation of the accuracy of BOTDA systems based on the phase spectral response," Optics Express **24**(15), 17,200–17,214 (2016).

[145] M. G. Herráez, K. Y. Song, and L. Thévenaz, "Arbitrary-bandwidth Brillouin slow light in optical fibers," Optics Express **14**(4), 1395–1400 (2006).

[146] J. Fang, P. Xu, and W. Shieh, "Single-shot measurement of stimulated Brillouin spectrum by using OFDM probe and coherent detection," in *Australian Conference on Optical Fibre Technology*, pp. AT5C–3 (Optical Society of America, 2016).

[147] J. Fang, W. Shieh, and P. Xu, "Single-shot Brillouin optical time domain analysis for distributed fiber sensing," in *2016 IEEE SENSORS*, pp. 1–3 (2016).

[148] J. Fang, P. Xu, Y. Dong, and W. Shieh, "Single-shot distributed Brillouin optical time domain analyzer," Optics Express **25**(13), 15,188–15,198 (2017).

[149] X. Bao and L. Chen, "Recent progress in Brillouin scattering based fiber sensors," Sensors **11**(4), 4152–4187 (2011).

[150] M. Alem, M. A. Soto, and L. Thévenaz, "Modelling the depletion length induced by modulation instability in distributed optical fibre sensors," in *23rd International Conference on Optical Fibre Sensors (OFS)*, vol. 9157, p. 91575S (2014).

[151] J. Urricelqui, A. Zornoza, M. Sagues, and A. Loayssa, "Dynamic BOTDA measurements based on Brillouin phase-shift and RF demodulation," Optics Express **20**(24), 26,942–26,949 (2012).

[152] X. Angulo-Vinuesa, A. Lopez-Gil, A. Dominguez-López, J. L. Cruz, M. V. Andres, S. Martin-Lopez, and M. Gonzalez-Herraez, "Simultaneous gain and phase profile determination on an interferometric BOTDA," in *24th International Conference on Optical Fibre Sensors (OFS)*, vol. 9634, p. 963419 (2015).

[153] Y. Zhang, Z. Ying, G. Tu, X. Zhang, and L. Lv, "Strain variation measurement with short-time Fourier transform-based Brillouin optical time-domain reflectometry sensing system," Electronics Letters **50**(22), 1624–1626 (2014).

[154] A. Zornoza, M. Sagues, and A. Loayssa, "Self-heterodyne detection for SNR improvement and distributed phase-shift measurements in BOTDA," Journal of Lightwave Technology **30**(8), 1066–1072 (2012).

[155] R. W. Boyd, *Nonlinear Optics* (Academic press, 2008).

[156] P. C. Hansen, V. Pereyra, and G. Scherer, *Least Squares Data Fitting with Applications* (JHU Press, 2012).

[157] P. H. Richter, "Estimating Errors in Least-Squares Fitting," TDA Progress Report pp. 42–122 (1995).

[158] R. J. Sheppard, "The least-squares analysis of complex weighted data with dielectric applications," Journal of Physics D: Applied Physics **6**(6), 790–794 (1973).

[159] J. R. Macdonald, J. Schoonman, and A. P. Lehnen, "Applicability and power of complex nonlinear least squares for the analysis of impedance and admittance data," Journal of Electroanalytical Chemistry **131**(C), 77–95 (1982).

[160] M. E. Orazem and B. Tribollet, "Complex Nonlinear Regression," in *Electrochemical Impedance Spectroscopy*, pp. 527–544 (John Wiley & Sons, Inc., 2017).

[161] M. E. Orazem, "A systematic approach toward error structure identification for impedance spectroscopy," Journal of Electroanalytical Chemistry **572**(2), 317–327 (2004).

[162] T. Horiguchi, K. Shimizu, T. Kurashima, M. Tateda, and Y. Koyamada, "Development of a Distributed Sensing Technique Using Brillouin Scattering," Journal of Lightwave Technology **13**(7), 1296–1302 (1995).

[163] A. W. Brown, M. D. DeMerchant, X. Bao, and T. W. Bremner, "Precision of a Brillouin-scattering-based distributed strain sensor," in *Smart Structures and Materials 1999: Sensory Phenomena and Measurement Instrumentation for Smart Structures and Materials*, vol. 3670, pp. 359–366 (International Society for Optics and Photonics, 1999).

[164] H. W. Ott and H. W. Ott, *Noise reduction techniques in electronic systems*, vol. 442 (Wiley New York, 1988).

[165] J. Fang, M. Sun, D. Che, M. Myers, and W. Shieh, "Complex domain Brillouin frequency estimation for distributed fiber sensing," in *Photonics Conference (IPC), 2017 IEEE*, pp. 695–696 (IEEE, 2017).

University Library

A gateway to Melbourne's research publications

Minerva Access is the Institutional Repository of The University of Melbourne

Author/s:
Fang, Jian

Title:
Advanced techniques for high-performance optical transmission and sensing

Date:
2018

Persistent Link:
http://hdl.handle.net/11343/220313

Terms and Conditions:
Terms and Conditions: Copyright in works deposited in Minerva Access is retained by the copyright owner. The work may not be altered without permission from the copyright owner. Readers may only download, print and save electronic copies of whole works for their own personal non-commercial use. Any use that exceeds these limits requires permission from the copyright owner. Attribution is essential when quoting or paraphrasing from these works.